

3-1-2003

REU 2002 Program Report

Clay Naito

Fyiad Constantine

Justin McCarthy

Michael Minicozzi

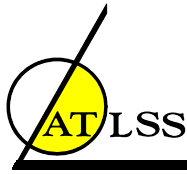
Follow this and additional works at: <http://preserve.lehigh.edu/engr-civil-environmental-atlss-reports>

Recommended Citation

Naito, Clay; Constantine, Fyiad; McCarthy, Justin; and Minicozzi, Michael, "REU 2002 Program Report" (2003). ATLSS Reports. ATLSS report number 03-03.

<http://preserve.lehigh.edu/engr-civil-environmental-atlss-reports/25>

This Technical Report is brought to you for free and open access by the Civil and Environmental Engineering at Lehigh Preserve. It has been accepted for inclusion in ATLSS Reports by an authorized administrator of Lehigh Preserve. For more information, please contact preserve@lehigh.edu.



LEHIGH
University

**FINAL REPORT
2002 REU PROGRAM**

by

Clay Naito, Ph.D.

Fyiad Constantine

Justin McCarthy

Michael Minicozzi

Greg Parent

Edward Regnier

ATLSS Report No. 03-03

March 2003

**ATLSS is a National Center for Engineering Research
on Advanced Technology for Large Structural Systems**

117 ATLSS Drive
Bethlehem, PA 18015-4729

Phone: (610)758-3525

Fax: (610)758-5902

www.atlss.lehigh.edu

Email: inatl@lehigh.edu

Table of Contents

Table of Contents.....	1
Section 1: Program Summary.....	3
Section 2: Summer Program Activities	4
2.1. Research Techniques	4
2.2. Engineering Field Trips	4
2.3. Social Activities.....	5
Section 3: 2002 REU Students, Projects, and Administrators	6
Section 4: Laboratory Testing Of FRP Bridge Deck-Reinforced Concrete Parapet Connection Details By Fyiad Constantine.....	7
4.1. Summary.....	7
4.2. Background.....	7
4.3. Overview	8
4.4. Planning And Design.....	9
4.5. Investigation	18
4.6. Instrumentation	27
4.7. Construction Of Set-Up	33
4.8. Conclusion	35
4.9. Acknowledgements	36
4.10. References	36
Section 5: Blast Testing, State of the Practice by Justin McCarthy.....	37
5.1. Project Summary	37
5.2. Background.....	37
5.3. Summary of Blast Wave Characteristics	37
5.4. Summary of Blast Components	39
5.5. Dangers From Blast.....	41
5.6. Current Test Facilities.....	43
5.7. Current Blast Experts.....	47
5.8. Current Testing Technologies.....	48
5.9. Concerns	50
5.10. Discussion.....	50
5.11. Acknowledgments	51
5.12. References	51
5.13. Appendix A: Column Calculations.....	53
Section 6: Mortar Reinforced With Superelastic Nickel-Titanium Fibers By Michael J. Minicozzi	55
6.1. PROJECT SUMMARY	55
6.2. BACKGROUND	55
6.3. PROJECT OVERVIEW	59
6.4. CONCLUSION	61
6.5. ACKNOWLEDGEMENTS.....	61
6.6. APPENDIX A.....	62
6.7. References	66
Section 7: Lateral Load Behavior of Unbonded Post-Tensioned Precast Concrete Walls with Horizontal Joints By Ed Regnier	68

7.1. Summary.....	68
7.2. Background.....	68
7.3. Wall System.....	69
7.4. Lateral Load Behavior	71
7.5. Stub-Panel Comparison	78
7.6. Conclusion	80
7.7. Acknowledgments	80
Section 8: Field Instrumentation, Testing and Analysis of the Dubois Creek Fiber Reinforced Polymer (FRP) Bridge By Greg Parent	81
8.1. Project Scope	81
8.2. Overview of the ATLSS Scope of work	82
8.3. Description of FRP Material.....	82
8.4. Field Equipment Used	83
8.5. Controlled Load Test.....	84
8.6. Test Results.....	85
8.7. Conclusions	90
8.8. Acknowledgements	90
8.9. References	90
Section 9: Acknowledgements	91

Section 1: Program Summary

In coordination with the Pennsylvania Infrastructure Technology Alliance (PITA) and the Center for Advanced Technology for Large Structural Systems (ATLSS) a Research Experience for Undergraduate (REU) program in Structural Engineering at Lehigh University was conducted. The program exposed five students to applied research. Students were given the opportunity to work in one of eight different thrust areas: earthquake hazard mitigation, explosive effects on structures, bridge field monitoring, fatigue and fracture, bridge systems, building systems, advanced materials, and advanced sensors. Practical research experiences were conducted with faculty advisors and graduate student mentorship. In addition to the focused research experience, the program incorporated student development workshops and field trips. Workshops focused on developing research abilities of the students. Site visits to various fabricators, construction projects, and engineering offices were used to illustrate application of research topics and career opportunities in structural engineering. The goal of the program was to expose students to the field of Civil Engineering and the pursuit of advanced degrees and careers in Structural Engineering.

Special attention was made to recruiting students from Universities that do not have significant research capabilities. In addition women and minorities were sought with the assistance of Henry Odi director of Lehigh University Academic Outreach Office. The program was coordinated by the principal investigator (PI) Assistant Professor Clay Naito, and Mr. Robert Alpago, associate director and industry relations for the ATLSS Center. Research supervisors included Associate Professor Steven Pessiki, Professor James Ricles, Professor Richard Sause, Assistant Professor Yunfeng Zhang, Dr. Robert Connor, as well as the PI. Financial support from the ATLSS center and the Pennsylvania Infrastructure and Technology Alliance (PITA) was provided to assist with successful operation of the program.

The program was conducted over a 10-week period from June 3 to August 9. Recruitment began early in the second half of the academic year. The program schedule is shown in Table 1. Descriptions of the scheduled activities are provided in section 2.

Table 1: Tentative Summer Program Schedule	
Week	Scheduled Activities
1	<ul style="list-style-type: none"> • Orientation meeting and advisor introductions • Applied research project initiation • Lab tour and program wide lunch meeting
2	<ul style="list-style-type: none"> • Library workshop • REU lunch meeting
3	<ul style="list-style-type: none"> • Program wide lunch meeting
4	<ul style="list-style-type: none"> • Schuylkill Precast Concrete Production Plant Tour
5	<ul style="list-style-type: none"> • Technical writing workshop • Presentation organization and delivery workshop
6	<ul style="list-style-type: none"> • Introduction to Microsoft PowerPoint • Program wide lunch meeting • Preliminary presentations conducted
7	<ul style="list-style-type: none"> • New York Brooklyn Bridge tour
8	<ul style="list-style-type: none"> • REU lunch meeting
9	<ul style="list-style-type: none"> • Program wide lunch meeting • High Steel Structures production facility tour
10	<ul style="list-style-type: none"> • Final student presentations • Final student papers submitted

Section 2: Summer Program Activities

The summer REU program incorporated applied research, research techniques, engineering tours, and social activities (Table 1).

2.1. Research Techniques

The program provided education in the basic skills needed for research in structural engineering. Workshops focused on both research methods and presentation techniques. The following workshops were conducted over the 10-week program:

- Library Search Techniques
- Presentation Organization and Delivery
- Introduction to Microsoft PowerPoint
- Preliminary Presentations

Library search techniques were taught early in the program to provide basic tools for use by the REU students in their research projects. The Lehigh University Engineering Library services department conducted this workshop. The workshop focused on methods for using library search systems to find information on various research topics. In addition, the students were familiarized with standard research sources such as engineering journal publications and conference proceedings.

Presentations make up an important part of an engineers career. Unfortunately, this topic is often overlooked in the undergraduate engineering education or at the best limited to the speech courses offered through humanities departments. The REU program provided workshops on presentation organization, delivery, and mechanics tailored for engineers. In addition, the students were given the opportunity to present their research to an engineering audience. Preliminary presentations were conducted midway through the program to assess and provide feedback to the students on their presentation techniques. This culminated in a series of final presentation seminars to the Civil Engineering Department.

2.2. Engineering Field Trips

To provide a balance with the research focus of the REU program a number of application oriented engineering field trips were conducted. The trips included visits to fabricators, construction sites, and engineering offices.



Figure 1: PITA REU students visit High Steel fabrication plant



Figure 2: PITA REU students visit Manhattan Bridge renovation project

In the 2002 PITA REU Program a number of exciting field trips were conducted. A visit to High Steel Structures Inc. Bridge Fabrication Plant, the largest steel bridge fabricator in the nation, was conducted (Figure 1). Students learned first hand how large structural bridge systems are produced from raw plate material to fully built bridges. A tour of the Schuylkill Products Inc. Precast Concrete Plant exposed students to the precast method of building and bridge construction and fabrication. A visit to Weidlinger and Associates field office and tour of the rehabilitation of the Manhattan Bridge was organized (Figure 2). Students were given the opportunity to talk to the site engineer and experience first-hand the design and repair issues associated with the aging infrastructure.








2.3. Social Activities

To help the students become acclimated to Lehigh University a number of social activities were undertaken. This included student luncheons, dinner outings, and social field trips. Wednesday luncheons were held throughout the duration of the program to assess and assist the progress of the students. Luncheons alternated between group luncheons (including all project participants) and student luncheons (including REU students and principal investigators). The group luncheons provided a casual forum to share research experiences and discuss social activities. The student luncheons provided an opportunity for the REU students to share any concerns or questions that came up with regards to the research advisors, mentors, and the profession of engineering.

Section 3: 2002 REU Students, Projects, and Administrators

The REU was organized and operated by Assistant Professor Clay Naito and ATLSS Associate Director and industrial relations Robert Alpage. Ms. Phyllis Pagel was the Accounts Manager for the project and for all ATLSS Center projects. Advertisements were distributed in May of 2002. Seven students applied to the program. This included six Lehigh University students and one student from Morgan State University. Five students were admitted to the program. They include Justin McCarthy, Fyiad Constantine, Edward Regnier, Michael Minicozzi, and Greg Parent. The program organization is summarized in Figure 3.

Figure 3: Program Organization

 Principal Investigator Clay Naito Assistant Professor		 Robert Alpage ATLSS Associate Director and Industrial Relations		
 Fyiad Constantine Morgan State University	 Justin McCarthy Lehigh University	 Michael Minicozzi Lehigh University	 Greg Parent Lehigh University	 Edward Regnier Lehigh University
Research Advisor: Clay Naito	Research Advisor: Clay Naito	Research Advisor: Yunfeng Zhang	Research Advisor: Robert Connor and Ian Hodgson	Research Advisors: Richard Sause and Stephen Pessiki
Student Advisor: Seoksoon Lee	-	Student Advisor: David Browne	Field Advisor: Carl Bowman	Student Advisor: Felipe Perez
Project: Laboratory Testing Of FRP Bridge Deck-Reinforced Concrete Parapet Connection Details	Project: Blast Testing, State of the Practice	Project: Mortar Reinforced With Superelastic Nickel-Titanium Fibers	Project: Field Instrumentation, Testing and Analysis of the Dubois Creek Fiber Reinforced Polymer (FRP) Bridge	Project: Lateral Load Behavior of Unbonded Post- Tensioned Precast Concrete Walls with Horizontal Joints

The students worked on a number of interesting projects including the development of innovative concrete mixtures, laboratory testing, field bridge evaluation and analytical research. The student final reports are included in the following sections 4 through 8.

Section 4: Laboratory Testing Of FRP Bridge Deck-Reinforced Concrete Parapet Connection Details By Fyiad Constantine

Advisors: Clay J. Naito, Ph.D., P.E. & Seoksoon Lee, MSCE

4.1. Summary

The search for new materials for more reliable, long lasting, safer construction of highways and bridges has led to the use of Fiber Reinforced Polymers (FRP). Though these are fairly new uses for the material it has proven itself a valuable substitute for traditional reinforced concrete decks. The material has performed well under typical loading conditions over relatively short spans.

The objective of this report is to look at the connection details at the glass-fiber reinforced bridge deck-reinforced concrete connection for a top-surface mounted concrete parapet. Based on the AASHTO design level, a transverse load will be applied to the parapet to induce connection failure so as to simulate possible failure due to a vehicle impact. The testing will check for failure types due in part, or whole, to the application of a load on the parapet resulting in a transfer of high stresses to the connections. This failure could come from the connections themselves, the parapet, or deck material.

At the time of writing this report the project went through three phases:

- 1) Planning and test set-up design
- 2) Instrumentation design
- 3) Construction of test set-up

In phase 1, the theoretical capacity of the structure was determined, and the boundary condition modeling was considered for set-up design. MathCAD was used in calculating the forces that would be transferred to the specimen, supports, and bracings.

For phase 2, the predominant possible modes of failure were itemized and as such the instrumentation plan was created. Instruments were placed at various positions to check the behavior of each component of the deck and parapet system.

Phase 3 was the culmination of all the pre-planning and planning stages where the assembly was actually undertaken for use in determining the objective of the research.

4.2. Background

Traditionally, bridge parapet to deck connections is made between concrete and steel, where both the deck and parapet are steel reinforced concrete structures. With the standard behaviors of each of the components, as far as their load capacities go, these systems could be designed where the yield load is known and the intended behavior is predictable. In the case of the parapet to deck system, connections are made such that the safety provided by the parapet is directly related to the level-of-service of the structure. Thus a bridge with a high speed limit would need a parapet that could withstand a high velocity impact. The optimal case for the system being one where on collision the deck system is undamaged and the parapet absorbs the energy of the impact and yields without failing. It should not stay too rigid either, as that would transfer most of the crash energy to the car and worse, the driver. For bridges, the typical parapet is a reinforced concrete fixture usually mounted to the top of the deck provided that the edge thickness of the deck is at least 8.0in.

These new FRP decks systems are usually composed of sheets of glass reinforcing fibers infused and set in a polyester or vinyl ester resin matrix. The other types of reinforcing fibers used are carbon and aramid (usually called Kevlar), fused with epoxy resins. Carbon and aramid fibers set in epoxy resins are the more expensive and as such not used in the experimental bridge building (Adapted from *Fiber-Reinforced Bridge Decks* Patrick Cassidy 2000).

The benefits of FRP decks is that it is:

- Light weight, thus reducing the dead load, and increasing the live load capacity
- Corrosion resistant, so a long service life expected
- High strength

- Fabricated in a controlled environment, thus ensuring high quality level
- Environmentally friendly
- Easily installed

The drawbacks of FRP decks is:

- More expensive than typical reinforced concrete deck
- Material is brittle, so limited yielding capacity
- Characteristics and performance relatively unknown in the bridge building field

FRP decks are generally made in two ways:

1. Sandwich or honeycomb method using vacuum assisted resin transfer molding (VARTM) techniques.
2. Pultruded tubes bonded together with adhesives.

The new FRP materials have been use on relatively short-span bridges (20-60ft.), where data regarding the performance of the out in the field can be accurately gathered. It is only after gaining a full understanding of the composite material, that it can be tested and later utilized on longer span bridges, and one day replace concrete decks altogether. Other Universities have been performing tests on the physical capacities of FRP composites, and have initiated the deck replacement using the composites. Along with the Transportation Research Board (TRB) and the Federal Highway Administration (FHWA), extensive testing has been going on regarding the suitability of using FRP.

Lehigh University and the ATLSS Center, is undertaking the project of looking at the connection details and analyzing this mechanism for the Pennsylvania Department of Transportation (Penn DOT). It is hoped that by understanding the way in which the reinforced concrete parapet and the FRP deck handle impact loads, that safer, more ideal deck systems may be build to handle the eventualities of everyday vehicular use without causing damage to the system. The research also serves to broaden the knowledge base of FRP materials in bridge building, and to bring into being a standard by which FRP structures may be designed.

4.3. Overview

The project undertaken by ATLSS Center, Lehigh University, is to test the limit of loading on a reinforced concrete parapet to FRP deck connection, within AASHTO standards for a test bridge, the Dubois Creek Bridge. Tests have been performed on decks but not too much emphasis has been placed on the interaction between parapet and deck, as a means of determining modes of failure due to vehicular impact loading.

The major concerns for the system is:

- What is the load capacity for the system until failure?
- Which component(s) of the system will succumb first under loading?
- How can the data gather be correlated over a wider scope?

The first step was to identify possible mechanisms of failure, or precursors that initiate failure in other components for the existing structure, and they were identified as:

- Crushing of the concrete parapet
- Yield and fracture of the reinforcement between the parapet and deck
- Yield and fracture of the steel reinforcement within the deck
- Tension or flexure failure of the top flange of the of the deck
- Buckling of the bottom flange of the deck
- Buckling of the deck web due to overturning of the parapet
- Pullout of the reinforcement from the deck

Using an appropriate model of the actual system for testing, the possible modes of failure will actually be evaluated. Thus the boundary conditions surrounding the actual deck had to be simulated under lab conditions, but also exaggerated somewhat to cause the components to undergo a worst-case scenario for interpolative reasons. Using the set-up model, calculations to determine the extent of deflections had to be done so that the appropriate instrumentation could be placed at the designated areas (as determined by considering mechanisms) of possible failure, to ascertain the type of failure and where.

This particular bridge was designed on a TL-2 level by AASHTO standards, and a load well exceeding the design capacity was used to bring about a worst-case situation. The test set-up was chosen as a 10ft. by 4ft. deck section fixed at one end and cantilevered out at the parapet end. The test load was set at a maximum of 200 kips (200,000lbs) to pull on the parapet with a controlled rate of displacement until failure was achieved.

From the results gathered by the instruments, it will be possible to quantitatively assess which mode of failure occurred, at what load value, and the levels of stresses that were carried by each component. The loading would have a lesser impact upon some parts of the specimen, whereas others may be in a near state of failure when the entire configuration fails. It is hoped that the testing and gauging would help to ascertain all of this information.

The theoretical mode of failure calculated using the Ultimate Moment Capacities of each of the critical components could give some prediction of the expected behavior; this may be proven or discredited after the actual test is performed. However, from these simplified analyses a better understanding of the practical mechanism at work could be accomplished. This would ultimately lead to work that improves on the design and efficiency of the connections, and/or material, as causes of failure would be identified.

4.4. Planning And Design

The intent of the research project was to provide information regarding the behavior of the connection detail between the FRP deck and the reinforced concrete parapet. To initialize the testing of the system and collection of data, an extensive amount of planning and design work had to be done. Knowledge of the actual bridge and the level of service that was intended for the structure was critical. The Pennsylvania Department of Transportation had design specifications for the actual bridge regarding impact standards for safety rails and parapets, and it was important to capture that in the test specimens, for consistency in comparing experimental with real world data/performance. By modeling the full-sized system to the component section chosen for testing, a configuration of how the test set-up should look was proposed and then designed for strength and more importantly with specificity toward the test objective, i.e. test of the connections under loading to failure. The bridge tested was the Dubois Creek Bridge; this actual bridge was instrumented to gather field data on the performance of FRP decks due to traffic loads and insitu conditions.

4.4.1. Existing Bridge Design

The actual Dubois Creek Bridge is located in the Great Bend region in northern Pennsylvania. The bridge consists of two (2) 20'x15' FRP deck panels supplied by Hardcore Composites Inc., Delaware, placed side by side on the abutments of the bridge without any other structural bracing (Fig. 1.1-1).

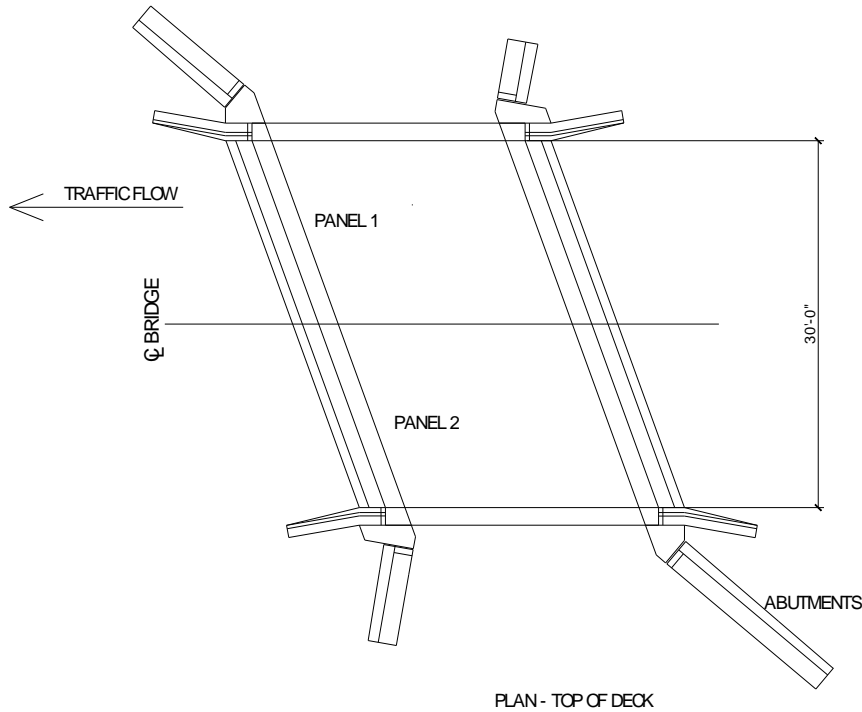
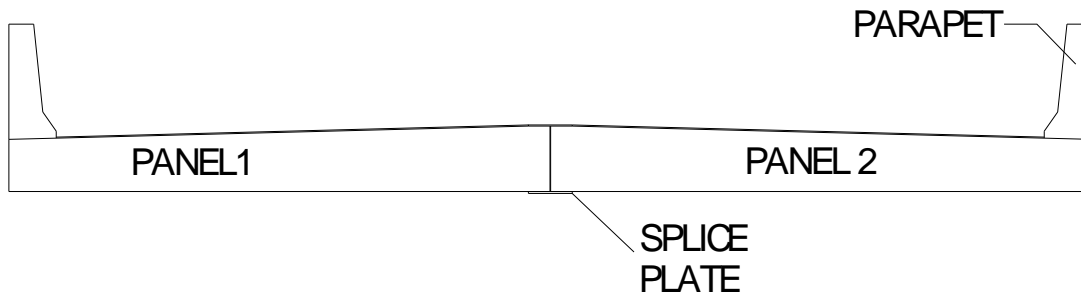


Fig. 1.1-1

Each panel covers the full span of the bridge (20') and half the total width of 30'. Steel reinforced concrete parapets 42" high are surface mounted to the bridge deck and connected by a pair of reinforcement bars connected to the deck by means of threads. Each pair of bars are spaced at 8" within the parapet and deck, and where the bars in the deck are placed at the seam of the composite material where it is totally encased in the resin-polymer matrix. At the center of the bridge, where both panels butt up against each other, there is a composite lap-splice plate that is grouted with epoxy to each panel to provide a connection between them (Fig. 1.1-2).



ELEVATION OF DECK

Fig. 1.1-2

The bridge has been designed such that the parapet wall has been assigned a TL-2 level of design, which quantifies the design forces and designations for it.

4.4.2. AASHTO Design For Parapet

The parapet was designed according to the American Association of State Highway and Transportation Officials (AASHTO) design specifications. The design forces for the railing system was based upon the traffic volume crossing the bridge, it's level-of-service, the speed limit and design vehicle used in testing (usually a truck). The design force, as defined by AASHTO, is the equivalent static force that represents the dynamic force imparted to a railing system by a specified vehicle impacting a railing at a designated speed and angle. From this definition,

reference may be made to TABLE A 13.2-1 Design Forces for Traffic Railings, to quantitatively assess the design performance of the railing.

Table A13.2-1 - Design Forces for Traffic Railings

Design Forces and Designations	Railing Test Levels						
	TL-1	TL-2	TL-3	TL-4	TL-5A	TL-5	TL-6
F_t Transverse (KIP)	13.5	27	54	54	116	124	175
F_L Longitudinal (KIP)	4.5	9.0	18.0	18	39	41	58
F_v Vertical (KIP) Down	4.5	4.5	4.5	18	50	80	80
L_t and L_L (FT)	4.0	4.0	4.0	3.5	8.0	8.0	8.0
L_v (FT)	18.0	18.0	18.0	18.0	40.0	40.0	40.0
H_e (min) (IN)	18	20	24	32	40	42	56
Minimum H Height of Rail (IN)	27	27	27	32	40	54	90

(From AASHTO 2000)

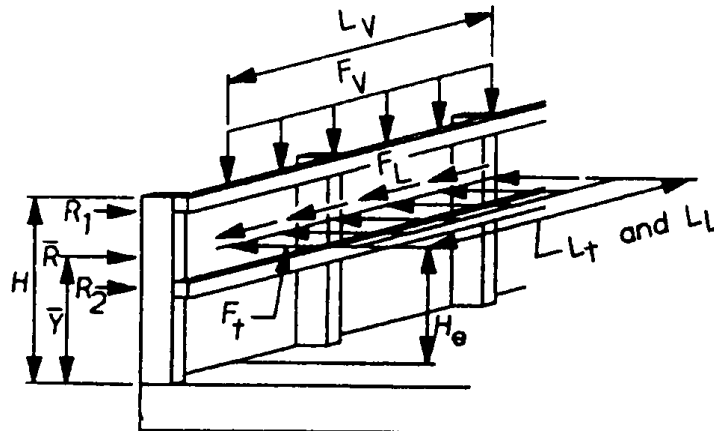


Figure A13.2-1 - Metal Bridge Railing Design Forces, Vertical Location, and Horizontal Distribution Length

(From AASHTO 2000)

The Dubois Creek Bridge was built with a surface mounted concrete parapet, which required that the deck be at least 8.0" and at a TL-2 level for a transverse force and longitudinal force acting at 20" from the deck surface.

AASHTO definitions of some terms stated in the table:

- Transverse loads are any horizontal design forces that are applied perpendicular to a railing or barrier system.
- Longitudinal loads are any horizontal design forces that are applied parallel to the railing or barrier system and that result from friction on the transverse loads.

The basis for these load combinations was derived from tests performed and also extensive monitoring of performance in the field. AASHTO specifications state that for concrete railings at the TL-4 level a required rail height of 34" is required. Note that a height of 32" is shown in the table for a TL-4 level because this height was

considered to be acceptable as many railings of this height were built and appear to be performing acceptably. At a TL-5 and TL-6 level, the height shown in Table 1 is the height required to engage the bed of the truck and the side of the tank, respectively.

The analysis performed for the design of the parapet was yield-line analysis; AASHTO design used this method to determine the failure within the parapet. This design covered only the flexural capacity of the concrete component, thus stirrups or ties would need to be present to resist the shear and/or diagonal tension forces. AASHTO design CA13.3.1 states that the ultimate flexural resistance of the bridge deck or slab should be determined in recognition that the deck is also resisting a tensile force, caused by the transverse component of the impact force. The analysis assumes that the yield-line failure pattern occurs within the parapet only and does not extend into the deck. Thus it is assumed that the deck is sufficiently strong enough to force the yield line failure to remain in the parapet. Another concern is that A13.1.2 states that reinforcing steel for concrete barriers shall have embedded length sufficient to develop yield in the bars. These latter points bring into question the flexural rigidity of the brittle FRP deck material and also the bond strength developed between the reinforcement and the composite material.

4.4.3. Modeling

The other important phase was the selection of a specimen model to accurately represent the full-sized bridge was a task in itself. The material properties of the FRP composite, and its structural behavior were not readily known for the bridge. An analysis of the full-scale bridge response was undertaken using Finite Element Modeling (FEM) to determine the stress distributions and critical regions under loading (Figs 1.3-1, 1.3-2, 1.3-3).

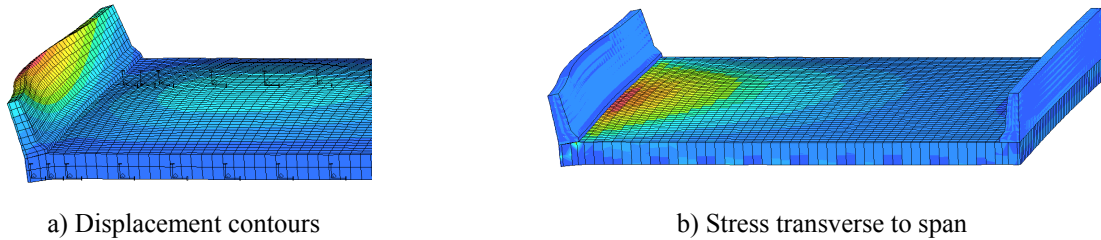


Figure 1.3-1: Finite element model of bridge with AASHTO transverse uniform load

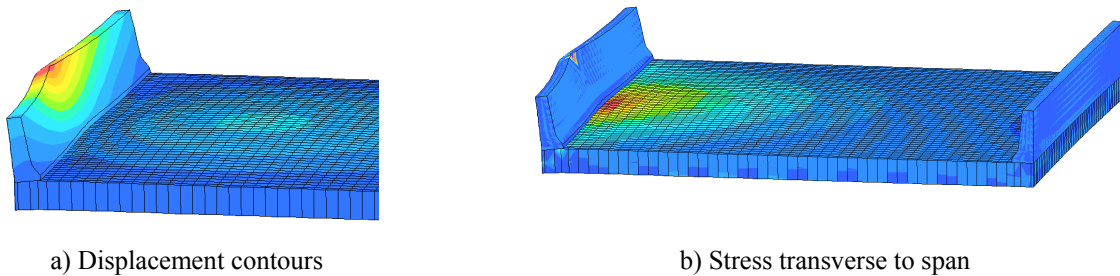


Figure 1.3-2: Finite element model of bridge with transverse point displacement

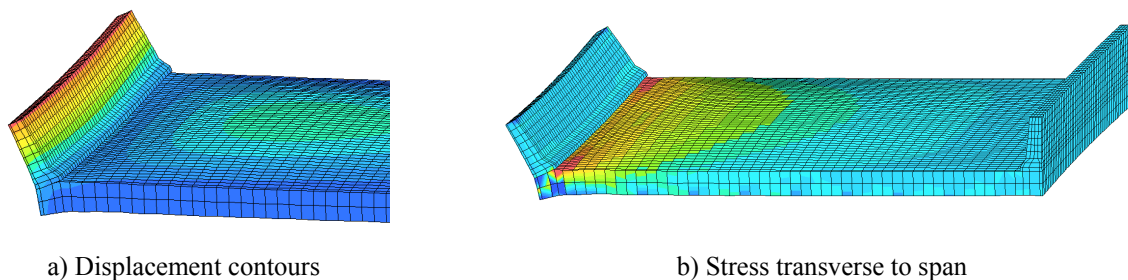


Figure 1.3-3: Finite element model of bridge with transverse uniform displacement

Using the FEM models, propositions for the specimen design were made so as to achieve similar stress distributions that also articulate the AASHTO design for the bridge. AASHTO's transverse uniform load compared well with a transverse point displacement. Experimentally it was not viable to perform a uniform loading test, as it would involve attaching a continuous line of actuators all applying the same force to the test piece to simulate a uniform load. Calculations were also done for a point displacement, and using yield line analysis the deck section would have to be close to 20' long, which even exceeded the actual deck width of 15'. A transverse uniform displacement was suggested to Penn DOT officials and it was decided that although this did not produce the actual profile they had suggested for the parapet, it was still a means obtaining a good load-displacement analysis of the section at the connections, or due to connection failure.

Since the bridge was designed at a TL-2 level, an effective length of 4' was set as the design span of the specimen, since this correlated with the length over which the uniform load was placed in TABLE A 13.2-1 Design Forces for Traffic Railings. An appropriate width was then to be selected for the deck panel. The worse case loading condition, and most probable impact load was assumed to be the transverse force perpendicular to the parapet; this was also incorporated into the modeling.

The first proposed design was a pinned-roller set-up, where the parapet end was cantilevered out 55.25". This design had the force at a height of 42", which was at a TL-5 level and not TL-2, and the stresses introduced into the deck by the roller support did not exist in the real bridge deck. The additional stress in the deck at the support would have placed the deck at a higher state of possible failure than the connections themselves (Fig 1.3-4).

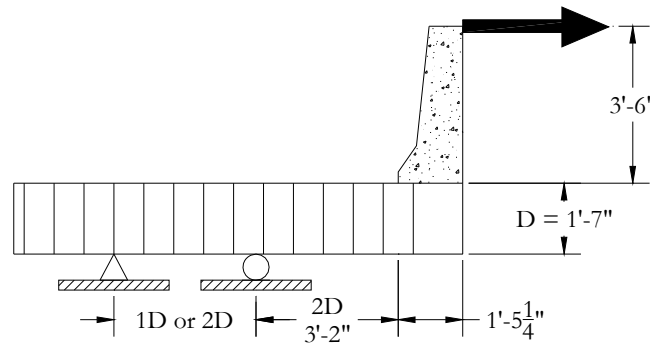


Fig. 1.3-4

The actual bridge was essentially fixed at the parapet wall and cantilevered out to the middle width of the bridge. Based on this, a new design for the model was chosen as a fixed end-cantilevered model. However, since the connections at the parapet end were under test the parapet end was cantilevered out instead. The other issue was choosing a deck length. Based on the moment profile of the free body diagram (FBD) for the configuration under transverse loading, a constant moment would be induced in the deck, so a reasonable length would suffice, and 10' was chosen for the specimen.

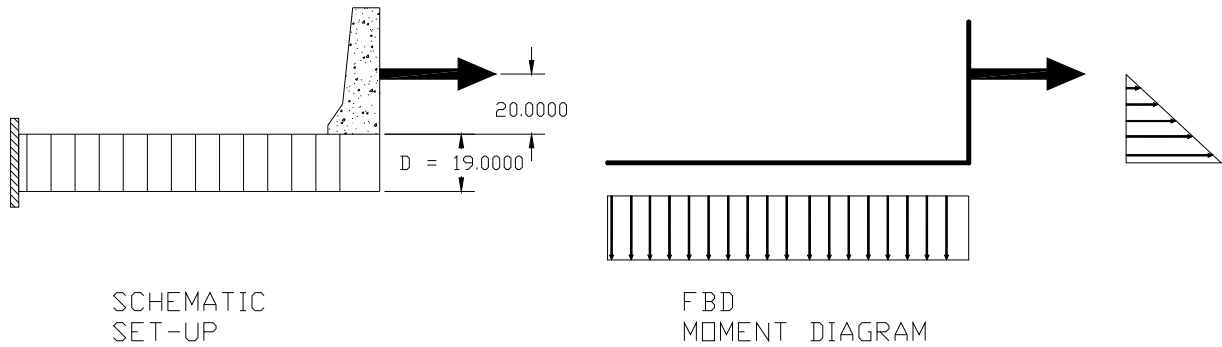


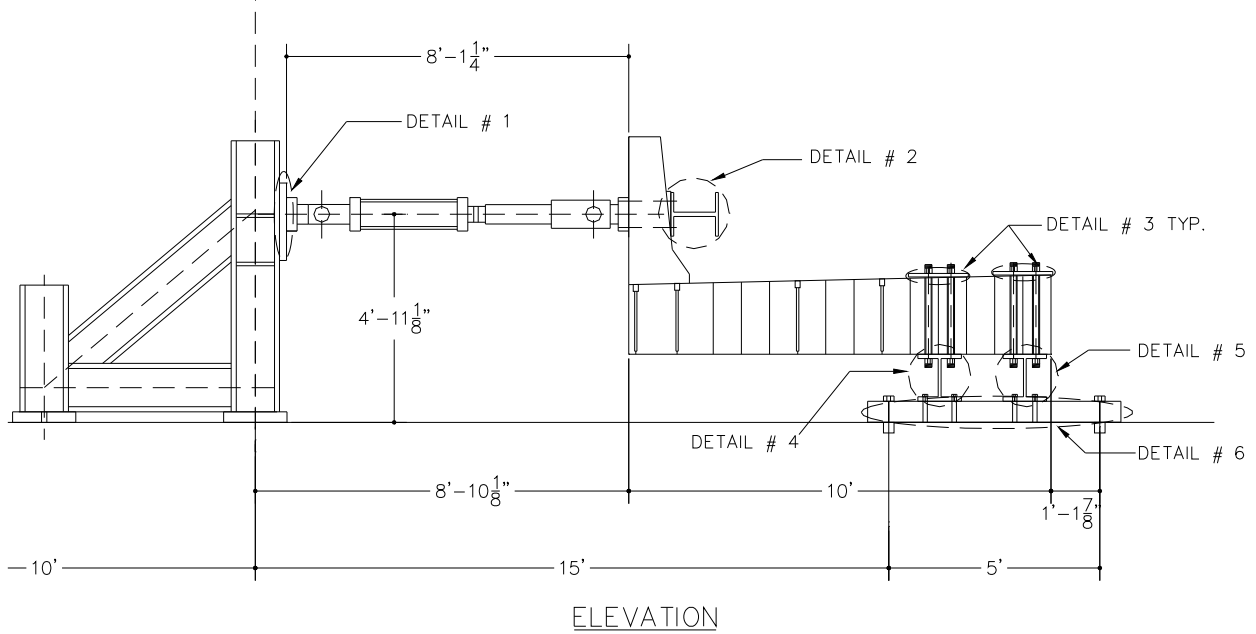
Fig 1.3-5

4.4.4. Set-Up Design And Configuration

Based on the proposed model an adequate, yet efficient set-up had to be created. The elementary configuration consisted of a 4'x10' FRP deck panel with a 42" surface mounted concrete parapet, cantilevered off of a fixed support on the opposite end. The initial thoughts were to use W-beams as the fixed-end support mounts and have a steel plate as the base plate and anchor plate for the system. The size and exact dimensions of these fixtures still had to be determined, and this was done according to their shear, axial force and moment capacities.

The main consideration in the design phase was the load being applied to the structure and the forces transferred to the other components of the specimen.

The loading would be accomplished by using a load actuator (which is essentially a hydraulic jack) capable of tensile or compressive loading, with a capacity of 200kips. The actuator would be in tensile loading affixed to the parapet wall at a height of 20" and anchored on the other end by use of a K-frame fixed to a strong-floor. The system would then be cantilevered out and fixed to the other end, to a pair of W-beams connected to the deck by use of threaded bolts going from the top flange of the deck to the top flange of the W-beams. The W-beams in turn would then be connected to an anchor plate attached to the strong-floor. The set-up configuration is shown in Fig 4.4-1.

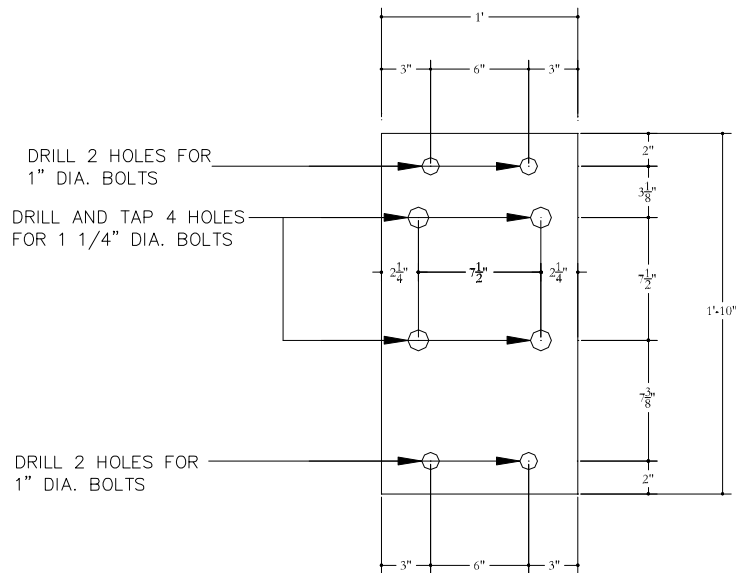


ELEVATION

Fig. 4.4-1

Each detail highlighted in the test set-up required special preparation in order to connect the parts and also bear the proposed loads.

Detail 1 Fig. 4.4-2 shows a connector plate used to connect the actuator plate to the K-frame. The main concern was the steel plate thickness and bolt length and size required such that the eccentric moment of the plate's off-centeredness would not cause bending of the plate or shear stripping of the bolts.



STEEL PLATE THICKNESS : 2.5 INCH

Fig. 4.4-2

Detail 2 Fig. 4.4-3 shows a W-beam (W12x136) affixed to the concrete parapet wall by threaded through bolts placed through the concrete parapet. This W-beam was used to get the even, uniform load distribution; because of

the sloping parapet wall, the flange of the beam was made vertical by grouting the gap between the wall and the beam. To eliminate excessive bending of the flanges, stiffeners were placed at the mid-span and near the ends of the beam. This measure was used to add rigidity to the beam and promote a more uniform load distribution.

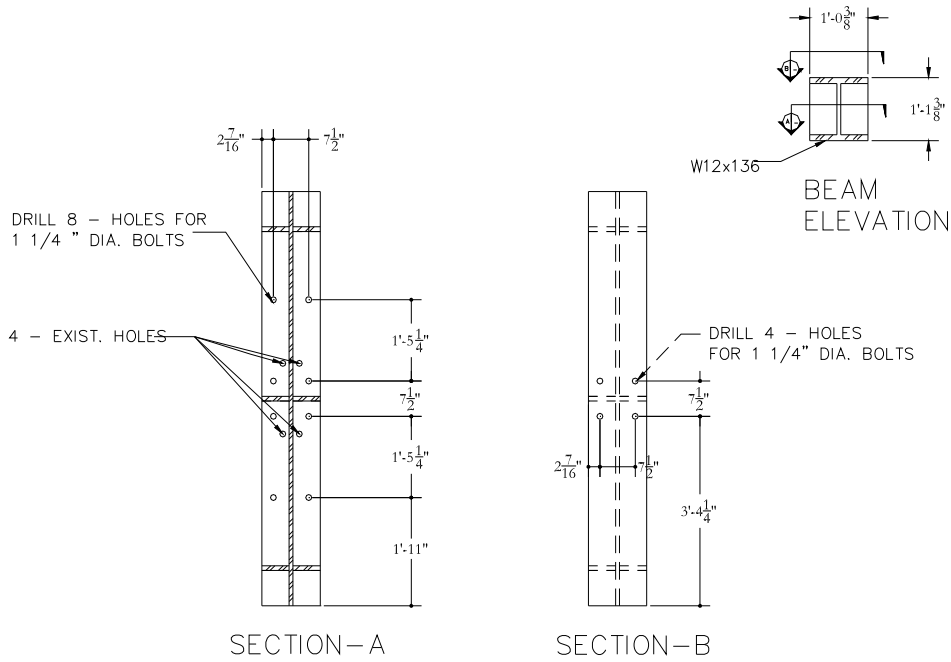
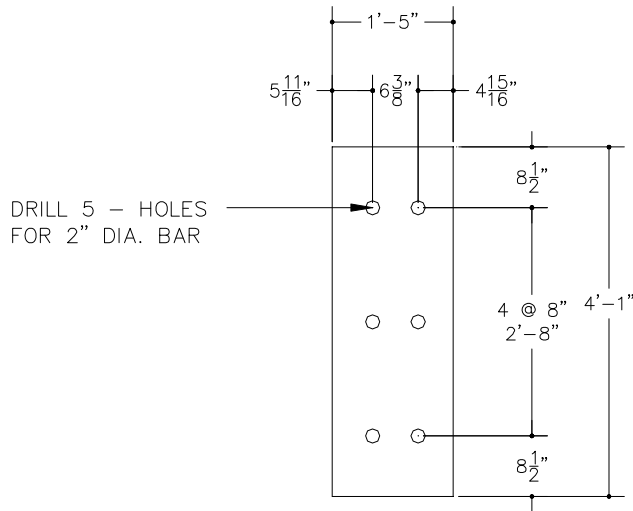


Fig. 4.4-3

Detail 3 Fig. 4.4-4 are a pair of bearing plates used to distribute the force caused by flexure of the deck at the bolt connections. The force present at each bolt on the top flange of the deck was calculated to be high enough to punch through the deck. The plate would create a bigger "footprint" or area over which the force could be distributed per bolt. Major considerations were plate thickness, and the length and breadth of the plate that would be conservative yet perform effectively, and not add stresses to the deck.



STEEL PLATE THICKNESS : 1 INCH

BASE PLATE (QUANTITY : 2)

Fig. 4.4-4

Detail 4 and 5 Fig. 4.4-5 created the fixed end supports and were a pair of stiffened W-beams (W12x136). They were designed such that they would provide the structural rigidity of the system in resisting shear and primarily moment forces that induced tensile forces in beam detail #5 and compressive forces in detail #4. An adequate bolt pattern and suitable number of bolts were required for the connections to hold rigid against the forces induced in each beam.

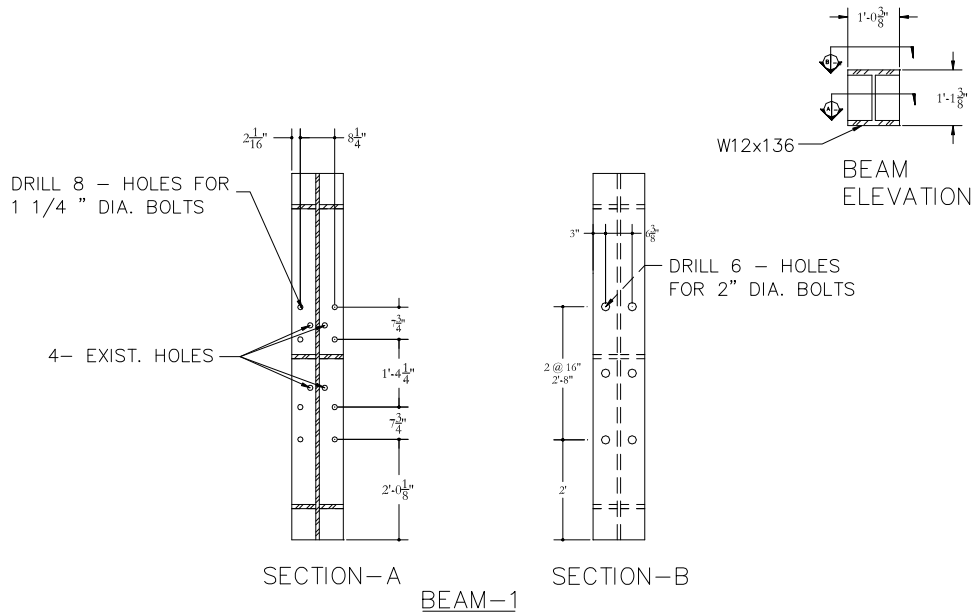


Fig. 4.4-5

Detail 6 Fig.4.4-6 shows the anchor plate, which was essentially a 6" thick steel plate, 2' wide and 6' long. This plate was fixed to the strong-floor and supported the entire structure above. The critical design of this plate was to resist flexure caused by the large moment-arm, and to bear the tensile force transferred by the beam above.

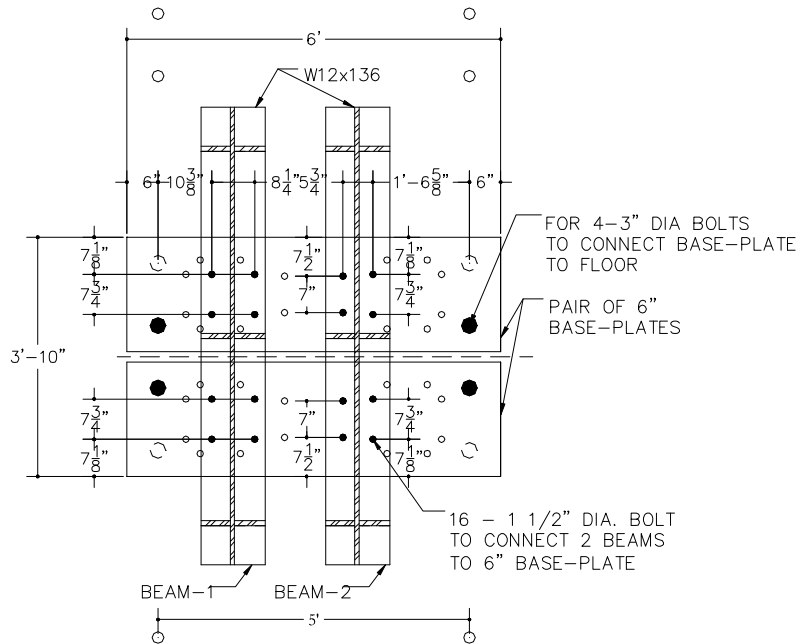


Fig.4.4-6

4.5. Investigation

The investigation looked at how the system would be analyzed in terms of displacements, as well as load capacities. The displacements were broken up into component and system displacements so that by getting loading data, load displacement correlations could be determined.

4.5.1. Actual Deformations Versus Theoretical Deformations

Actual displacements:

Assuming extension to be positive, the expression relating the sum of displacements can be written as:

$$\Delta_T = \Delta_1 + \Delta_2 - \Delta_3 \text{ (Fig. 5.1-1)}$$

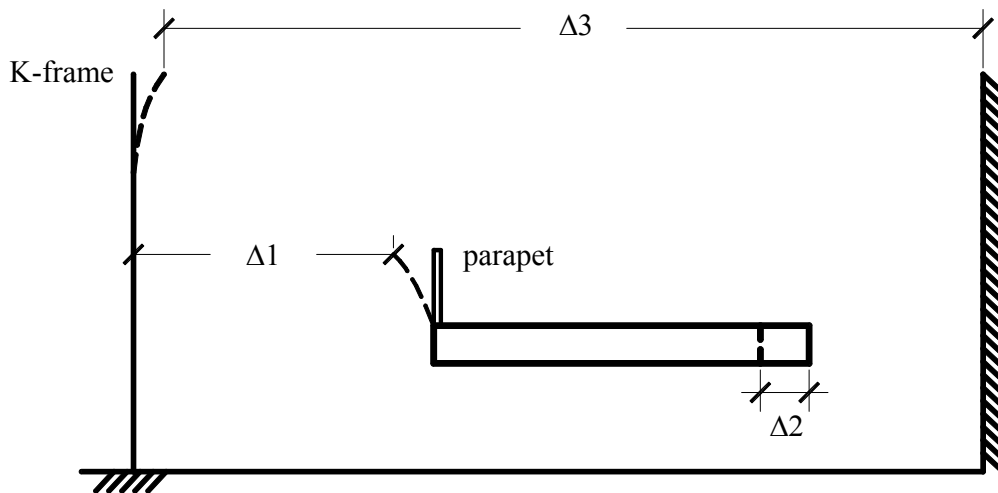


Fig. 5.1-1

Where Δ_T = Total deflection of the specimen

Δ_1 = Movement of the parapet

Δ_2 = Movement of specimen support

Δ_3 = Movement of K-frame

Theoretical displacements:

Theoretical displacements assume that the structure is acting under ideal conditions, and is perfectly fixed at one end, and cantilevered on the other. The sum of all ideal component displacements is equal to the sum of the actual displacements of the test setup components. In this model, Fig.5.1-2, the expression for the sum of all displacements is:

$$\Delta_T = \Delta_{A1} + \Delta_{A2} + \Delta_{A3} + \Delta_{A4} + \Delta_{A5}$$

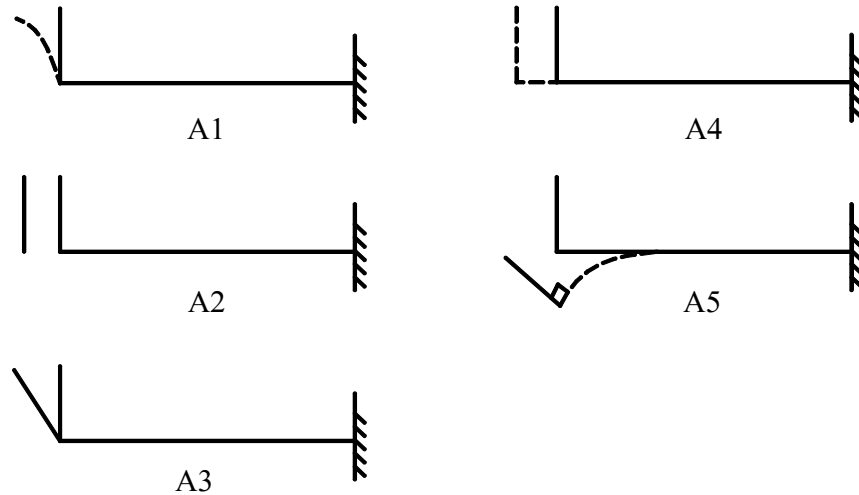


Fig. 5.1-2

Where Δ_T = sum of the component displacements $A_1 A_2 A_3 A_4 A_5$ (total displacement)

Δ_{A1} = displacement by flexure of the parapet

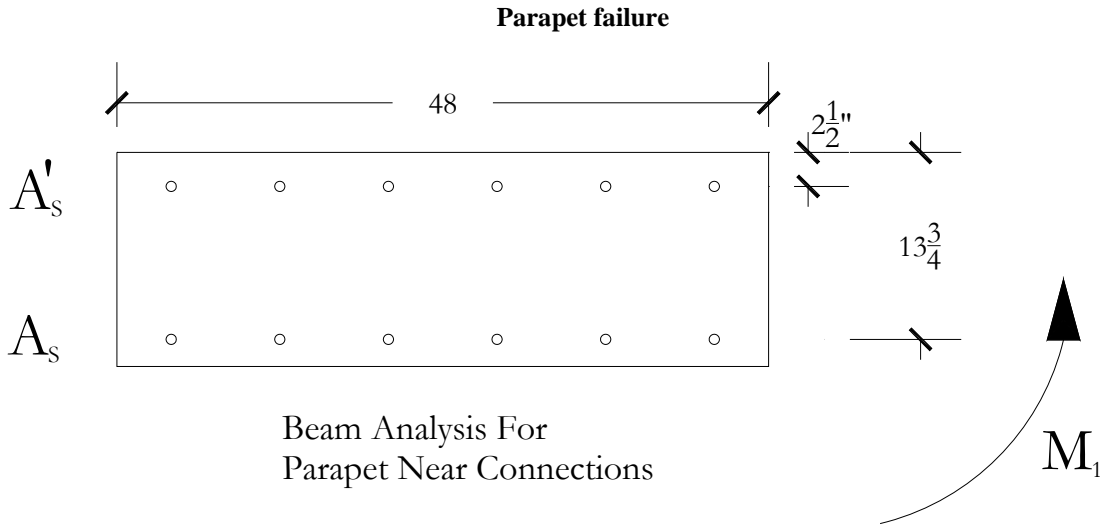
Δ_{A2} = displacement by shear of the connections

Δ_{A3} = displacement by rotation of the parapet about the connection

Δ_{A4} = displacement by axial deformation of the deck

Δ_{A5} = displacement by flexure of the deck

4.5.2. Simplified Calculations



$$6 \text{ #6 bars } A_s = 2.65 \text{ in}^2$$

$$6 \text{ #6 bars } A'_s = 2.65 \text{ in}^2$$

$$d = 13.75 \text{ in}$$

$$d' = 2.5 \text{ in} \quad f'_c = 4 \text{ ksi}$$

$$f_y = 60 \text{ ksi} \quad \beta_1 = 0.85 \quad E_s = 29000 \text{ ksi}$$

$$c_b = d \left(\frac{87}{87 + f_y} \right)$$

$$\epsilon_y = \left(\frac{f_y}{E_s} \right) = \left(\frac{60}{29000} \right) = 0.00207$$

$$= 13.75 \left(\frac{87}{87 + 60} \right) = 8.138 \text{ in}$$

$$a_b = \beta_1 \cdot c_b = 0.85(8.138) = 6.9173 \text{ in}$$

$$\epsilon'_s = 0.003 \left(\frac{c_b - d'}{c_b} \right) = 0.003 \left(\frac{8.138 - 2.5}{8.138} \right) = 0.00208$$

Since $\epsilon'_s > \epsilon_y$ **Compressive steel yielding**

$$A_s \text{ bal.} = \frac{[A'_s (f'_s - 0.85 f'_c) + 0.85 f'_c b a_b]}{f_y} = 21.31 \text{ in}^2$$

$$A_s < A_s \text{ bal} \quad \epsilon_s > \epsilon_y \quad f_s = f_y$$

$$A'_s (f'_s - 0.85 f'_c) + 0.85 f'_c b \beta_1 c = A_s f_y$$

$$c = 0.06495$$

$$\epsilon'_s > \epsilon_y$$

Iterative calculation

$$A'_s f_y + A_s f_y = 0.85 f'_c b \beta_1 c$$

$$c = 2.29 \text{ in}$$

So using

$$\frac{0.003}{c} = \frac{\varepsilon_s'}{d'-c}$$

$$\therefore \varepsilon_s' = 0.000275 \ll \varepsilon_y$$

From

$$\frac{0.003}{c} = \frac{\varepsilon_s'}{d'-c}$$

$$\Rightarrow f_s' = \varepsilon_s' \cdot E = \frac{0.003(d'-c)}{c} \cdot E$$

Then using

$$A_s' \left(\frac{0.003(d'-c)}{c} \cdot E \right) + A_s f_y = 0.85 f_c' b \beta_1 c$$

Solving for c

$$c = 1.80 \text{ in}$$

So now

$$\varepsilon_s' = \frac{0.003(2.5 - 1.8)}{1.8} = 0.00117 < \varepsilon_y$$

Check $\varepsilon_s > \varepsilon_y$

$$\varepsilon_s = \frac{0.003(13.75 - 1.8)}{1.8} = 0.0199 \gg \varepsilon_y$$

The Nominal Moment Capacity

$$M_n = \left[0.85 f_c' b \beta_1 c \cdot \left(d - \frac{a}{2} \right) \right] - [\varepsilon_s \cdot E \cdot (d - d')]$$

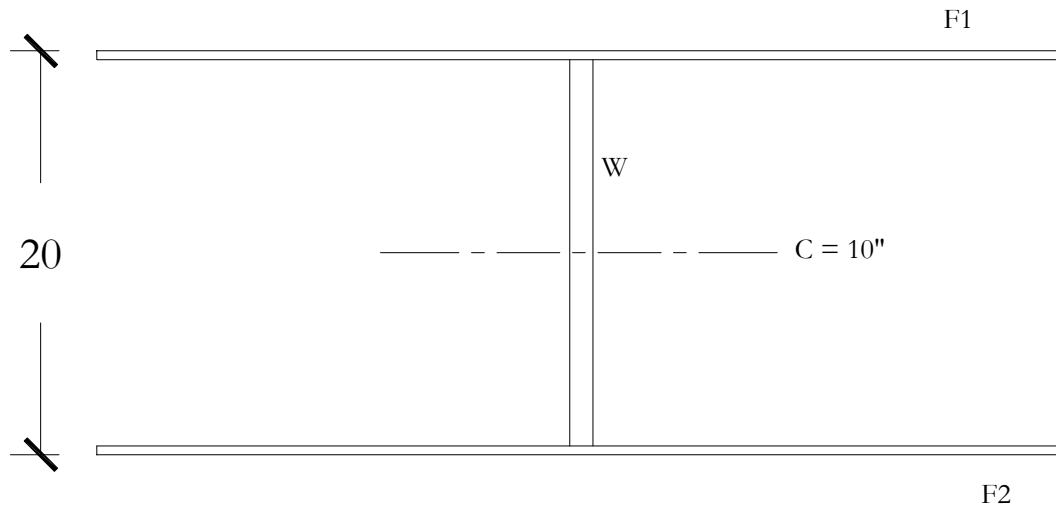
$$M_n = 2860 \text{ kip.in}$$

Since the moment arm between the connection and the load is 20" the force required by the actuator to cause failure within the concrete:

$$P_{act} = \frac{M_n}{20} = 143 \text{ kips}$$

Deck Failure

Simplified analysis modeled the deck as a simple I-beam



Simplified Deck Section

Due to symmetrical section assumption centroid (c) = 10" from base

Top Flange thickness (F1) = 0.432"

Breadth (b) = 48"

Height (h) = 0.432"

Distance from centroid of flange to (c) = 10-0.216 = 9.784

Bottom Flange thickness (F2) = 0.432"

Breadth (b) = 48"

Height (h) = 0.432"

Distance from centroid of flange to (c) = 10-0.216 = 9.784

Σ Web thickness (W) = 1.152"

Breadth (b) = 1.152"

Height (h) = 19.136"

Distance from centroid of flange to (c) = 10-10 = 0"

Moment of inertia

$$I_x = \frac{1}{12}bh^3 + Ad^2$$

$$I_x = 2 \left[\frac{1}{12} (48)(0.432)^3 + ((0.432 \times 48)(10 - 0.216)^2) \right] + \left[\frac{1}{12} (1.152)(19.136)^3 + 0 \right] = 4643.32in^4$$

Nominal Moment Capacity

$$M_n = F_y \frac{I_x}{c}$$

The lower force value for the FRP based on calculated results was $F_y = 62.13 \text{kips}$ for compression

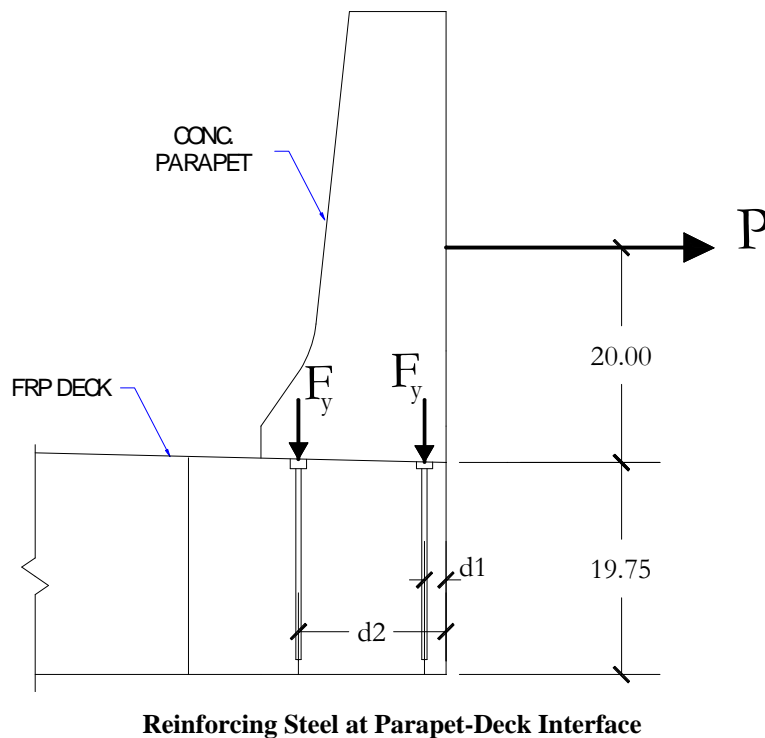
Hence the conservative Nominal Moment Capacity:

$$M_n = 62.13 \left(\frac{4643.32}{10} \right) = 28,848.9 \text{kip.in}$$

The force required by the actuator to cause failure within the deck:

$$P_{act} = \frac{M_n}{30} = 961.6 \text{kips}$$

Reinforcement steel failure



$$\sigma_y = 60 \text{ksi}$$

$$A_s = 2.65 \text{in}^2$$

$$F_y = \sigma_y A_s = 60 \cdot 2.65 = 159 \text{kips}$$

Assuming that parapet is overturning, and both rows of reinforcement in tension

Nominal Moment Capacity

$$M_n = F_y d_1 + F_y d_2$$

$$M_n = 159(13.75 + 2.5) = 2583.75 \text{kip.in}$$

The force required by the actuator to cause failure within the steel reinforcement at the parapet-deck interface

$$P_{act} = \frac{M_n}{20} = 129.2 \text{ kips}$$

4.5.3. Relevance Of Data And Evaluation

The data collected should correlate with the theoretical calculations to some extent, however the specific property behavior of FRP materials is unknown. The actual deforming ability of the material will be put to the test and the strength characteristic as applied to the construction of bridges will be answered. Impact tests and design loads for reinforced concrete parapets connected to reinforced concrete slabs are well known to engineers due to extensive tests performed. It is hoped that similar testing of FRP decks would give a better idea of its performance from a standardization point of view, where AASHTO would have designs to accommodate FRP decked bridges.

From the analysis that will be performed in this specific test, data such as the strains and displacements measured can be used to calculate stress levels in each material and at critical points. From the stress behavior better approximations can be arrived at with the use of FEM models, since empirical data can be used to develop standard relationships for similar FRP material, and input into the material properties for such models. Stresses can be related to strains for the FRP and will give it a section property (Elastic Modulus) for the configuration chosen for testing. Since the material is brittle it is necessary to know the failure point so that an appropriate factor can be incorporated for design purposes.

The expectation is, that the behavior of the specimen will be somewhat closely related to the theoretical model, and the mode of failure should come in the form of connection reinforcement yielding Fig. 5.3-1.

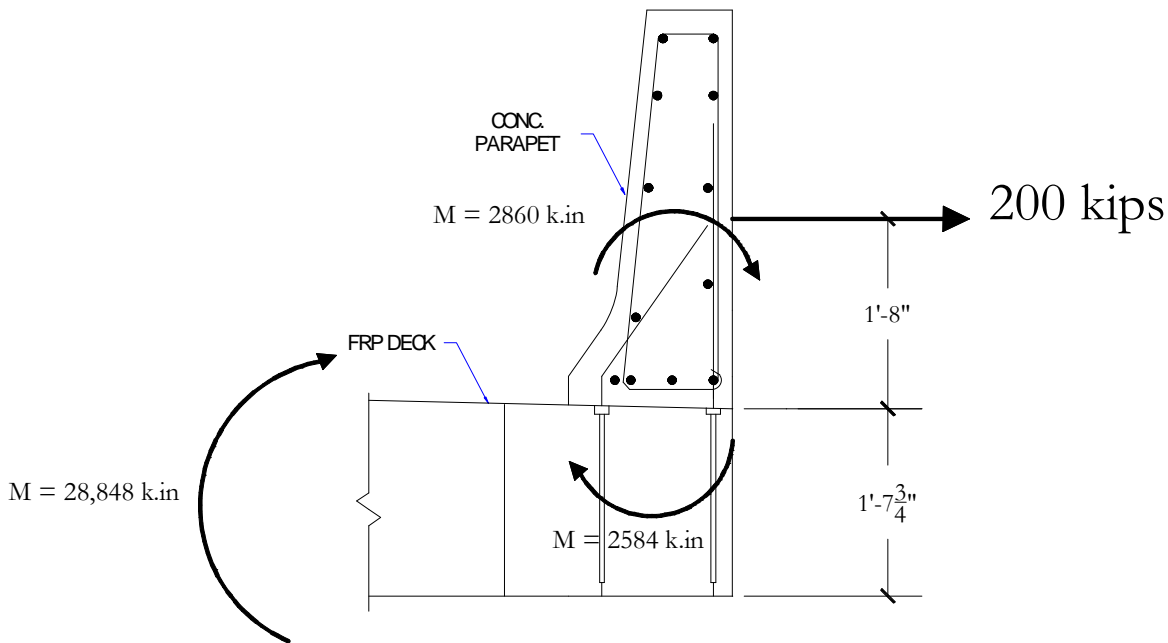


Fig. 5.3-1

Figure 5.3-1 shows that the theoretical calculated moment capacity for the system is the least for the reinforcement, so failure is expected at the connection and due to the steel reinforcement.

This assumption was the basis of the gauging locations, from which the concrete strain will be measured, the steel strain will be measured and the deck strain will be measured. Gages on the reinforcement bars at the concrete connection and the deck connection are critical points, so too is the concrete section just above the parapet deck interface, and the web and flanges of the deck. Using appropriate transformation equations the strains in each component will be found, and the actual progressive failure and more importantly the initiating mode of failure will be known.

By using a constant rate of displacement the load-displacement profile for the system could be calculated, as well as load-displacement for the component systems (deck, concrete, reinforcement in deck and concrete). It is important

that as many of the systemic displacements are recorded for a comprehensive understanding of how applied loads (impact loads) will be absorbed in such a way not to cause damage to the deck system, hence the reason for the instrumentation design chosen.

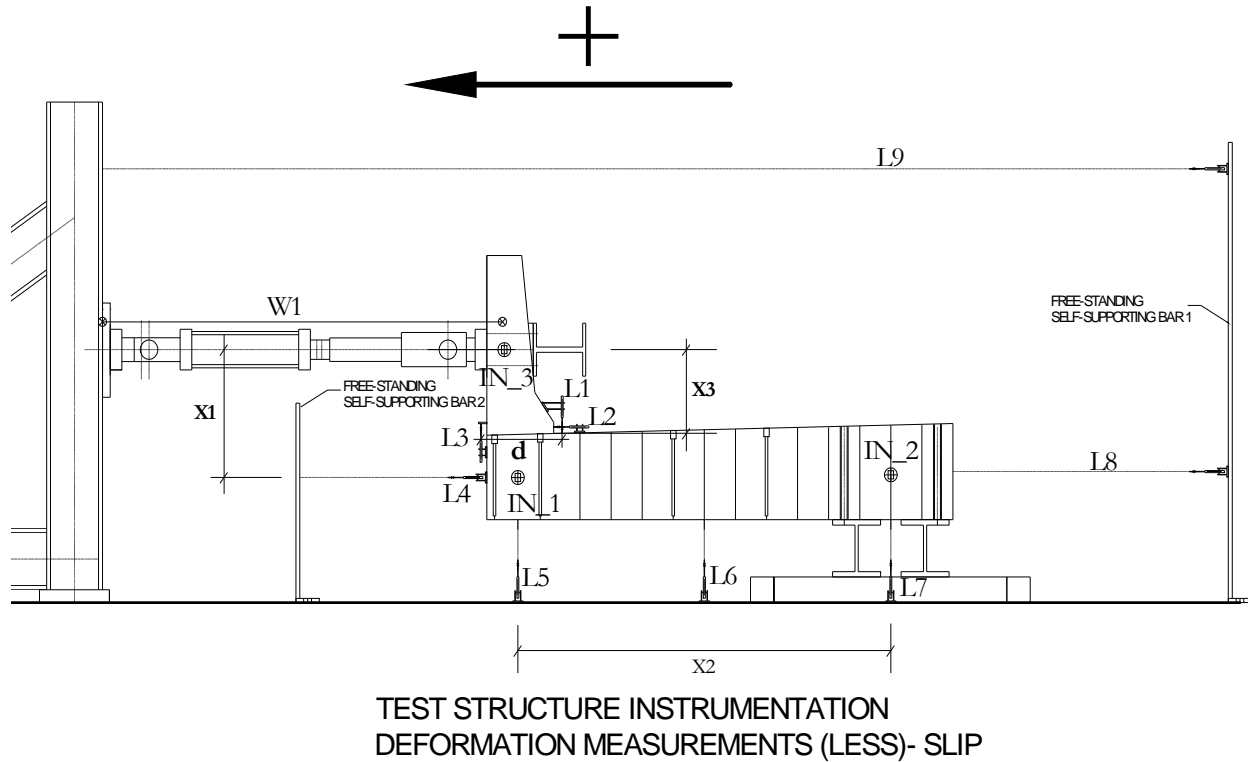


Fig. 5.3-1

Fig. 5.3-1 shows the displacement calculations for the system components in terms of the instrumentation used.

$$\text{Total Displacement of Specimen } \Delta_T = (-W1) + L9 - L8$$

Component displacements

$$\Delta_T = \Delta_{A1} + \Delta_{A2} + \Delta_{A3} + \Delta_{A4} + \Delta_{A5}$$

$$\Delta_{A1} = \frac{2}{3} X_3 \left(\text{IN}_3 - \text{IN}_1 - \left(\frac{L2 - L3}{d} \right) \right)$$

$$\Delta_{A2} = L2$$

$$\Delta_{A3} = X_3 \left(\frac{L2 - L3}{d} \right)$$

$$\Delta_{A4} = -L4 - L8$$

$$\Delta_{A5} = X_1 (\text{IN}_1 - \text{IN}_2) = X_1 \left(\frac{2}{X_2} (L5 - \text{IN}_2 \cdot X_2) \right)$$

The proposed instrumentation for the setup was based on the relationships formulated for the theoretical displacements.

Load-displacement results from the existing system can be used by engineers who plan to work on similar FRP-R.C. concrete type bridges when designing for impact levels as far as understanding which load is maximum load for the system, and maximum displacement. These are two important criteria used by engineers in the design of structures,

and having quantitative results will greatly enhance the understanding of how much load and displacement an actual parapet can withstand, while being part of an FRP system, before failure or within safety standards (e.g. AASHTO standard designs). Due to the relative innovation of FRP in bridge building and design, even AASTHO will gain from this research by having more information about such systems for the preparation of national FRP bridge design standards for the industry.

4.6. Instrumentation

The specimen set-up captured an acceptable approximation of the full-scale response of the actual bridge as far as connection detail was concerned as gathered from the FEM models. The means of verifying this information experimentally was by using instruments to capture possible points of failure, as well as significant areas of interest to determine their performance at failure for the system. Theoretical qualitative analysis of the specimen was done to assess the possible behavior of the overall system and component parts, to identify mechanisms of failure.

The modes of failure were identified primarily as

- Breaking of the concrete parapet
- Steel reinforcement within the parapet connecting to deck may yield
- Steel reinforcement within the deck connecting to parapet may yield
- The top flange of the of the deck may fail in tension or flexure
- The bottom flange of the deck may buckle
- The web of the deck may buckle as the deck is set in flexure
- The reinforcing bars in the deck may pullout

Based on simplified calculations, displacements and moment capacities gave some idea of what might be expected from the system and components within the system.

4.6.1. Selection

The mechanisms of failure and theoretical displacements that were identified, aided in the selection of gauging devices for the specimen. Based on the mechanisms of failure, the gages were selected as such:

1. Breaking of the parapet

For the measurement of this possible type of failure, concrete gages were attached to the external faces of the concrete parapet, front and back, to get a strain profile within the concrete. With the gage at the opening having zero (0) strain, and the gage on the compressive face having maximum strain Fig. 6.1-1a&b.

2. Steel reinforcement connecting parapet to deck

Unidirectional strain gages were attached to the reinforcing bars within the parapet to determine the strain on the bars themselves that were set in the concrete. They were placed at the section of least reinforcement, as close to the connections, where the propensity for failure was highest Fig. 6.1-1a&b.

3. Steel reinforcement connecting deck to parapet

Unidirectional strain gages were placed on the bars embedded within the deck. The bond strength between the composite and the rebar was unknown, so the strain on the gages would help determine whether these bars were being set into a condition of yield or pullout. Yielding would mean high strain measurement, whereas pullout would be marked by a low strain being recorded Fig. 6.1-1a&b.

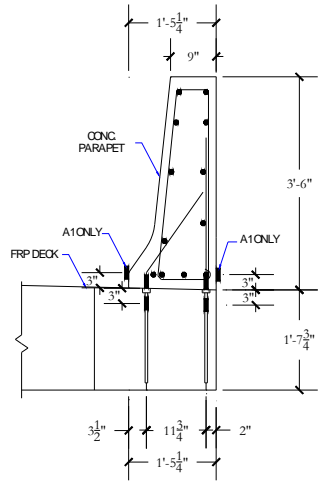
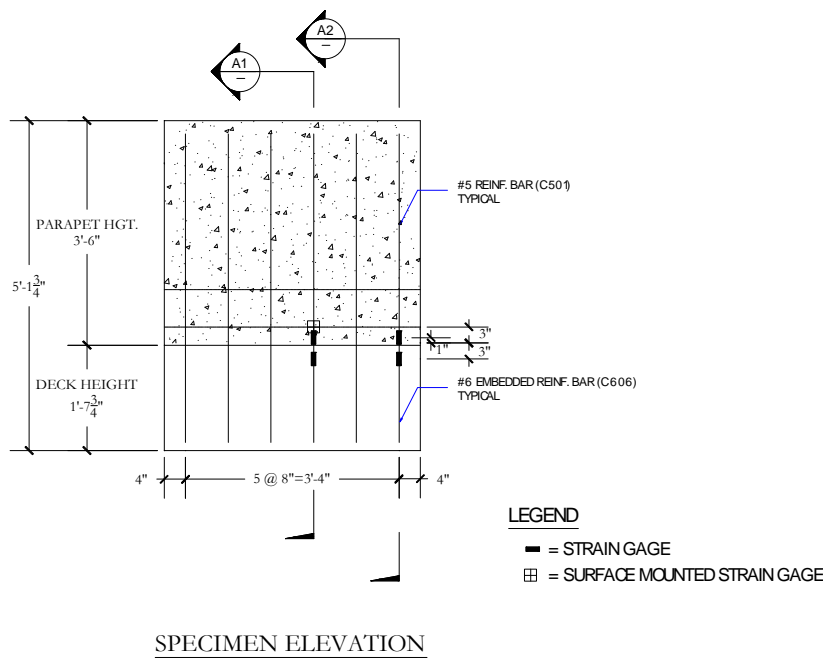


Fig. 6.1-1a. SECTION DRAWING OF PARAPET AND DECK GAGES



SPECIMEN ELEVATION

Fig. 6.1-1b

4. Top flange of the deck failing in tension

Tri-axial gages (rosettes) were placed in the top flange of the deck to record the various components of strain present in the orthotropic deck material. Rosettes are a configuration of 3 strain gages set in a 0,45,90 degree orientation capable of recording transverse, longitudinal and torsional strain Fig. 6.1-2.

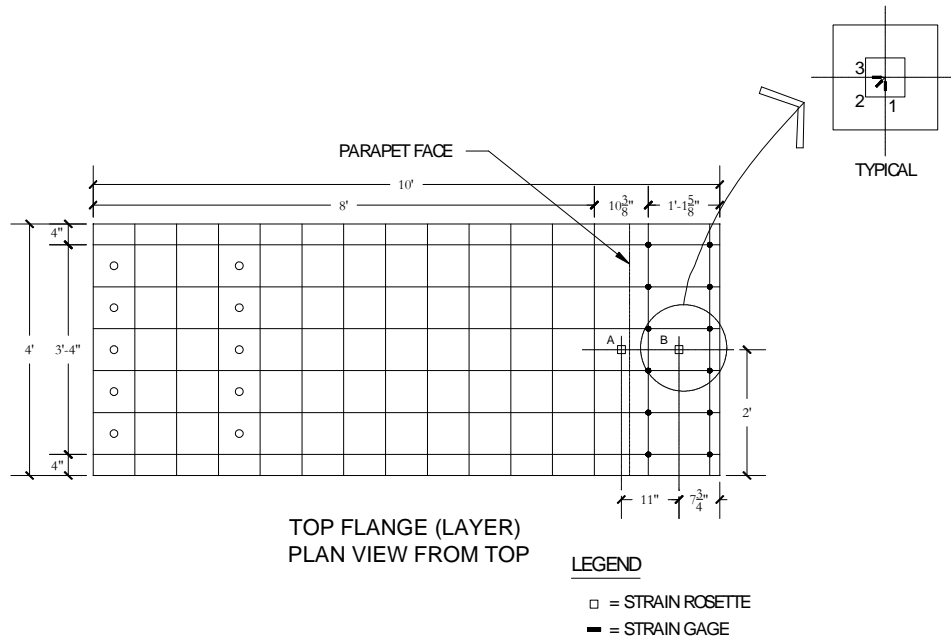


Fig. 6.1-2

5. Bottom flange of the deck buckling

Similar rosettes were placed in the bottom flange of the deck at corresponding locations to those in the top flange to check for buckling of the lower flange under compression.

6. Web buckling and possible shear

Rosettes were instrumented in the web of the deck to check primarily for buckling of the webs and for the secondary effects, if any, of shear strain Fig. 6.1-3.

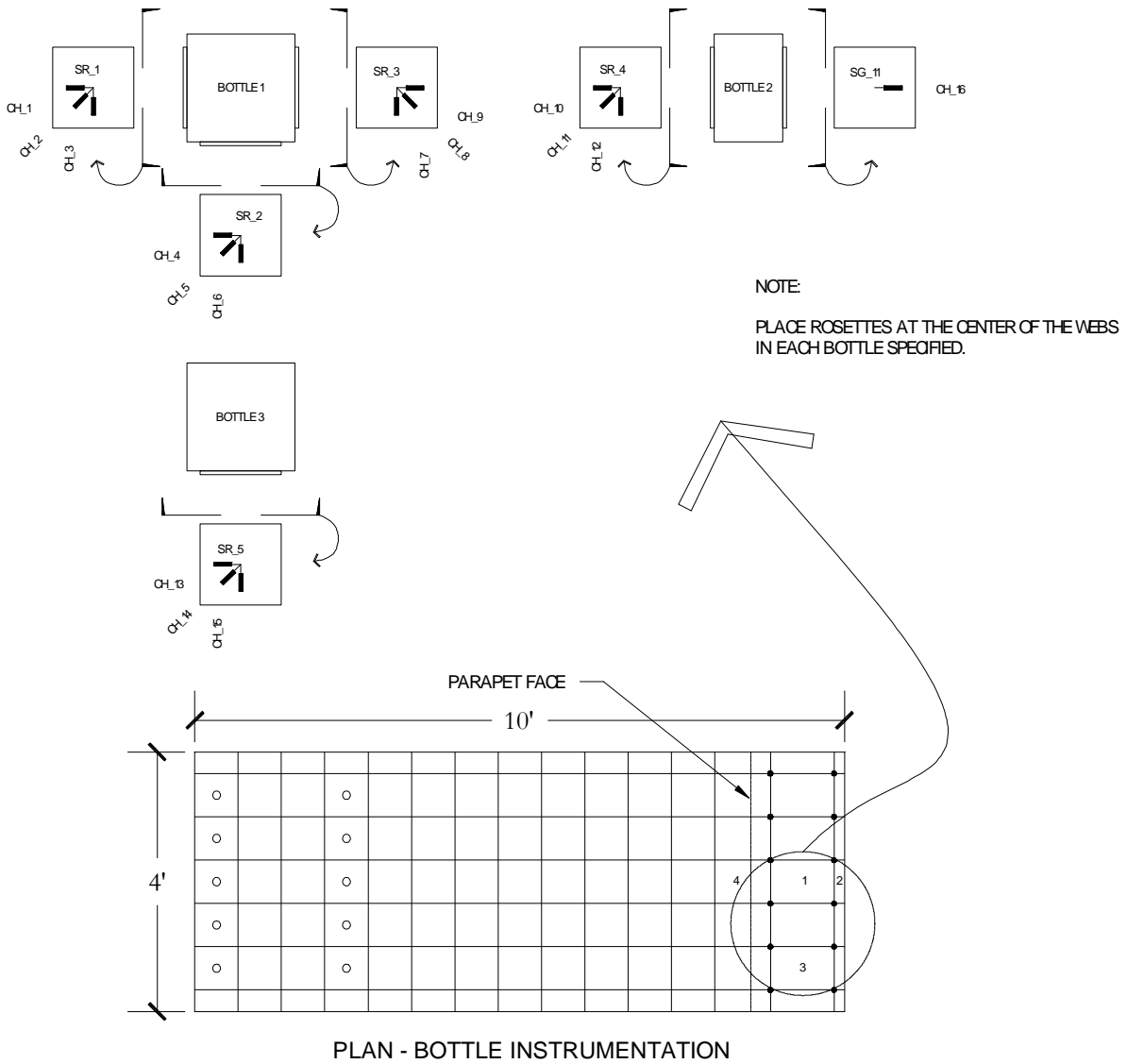
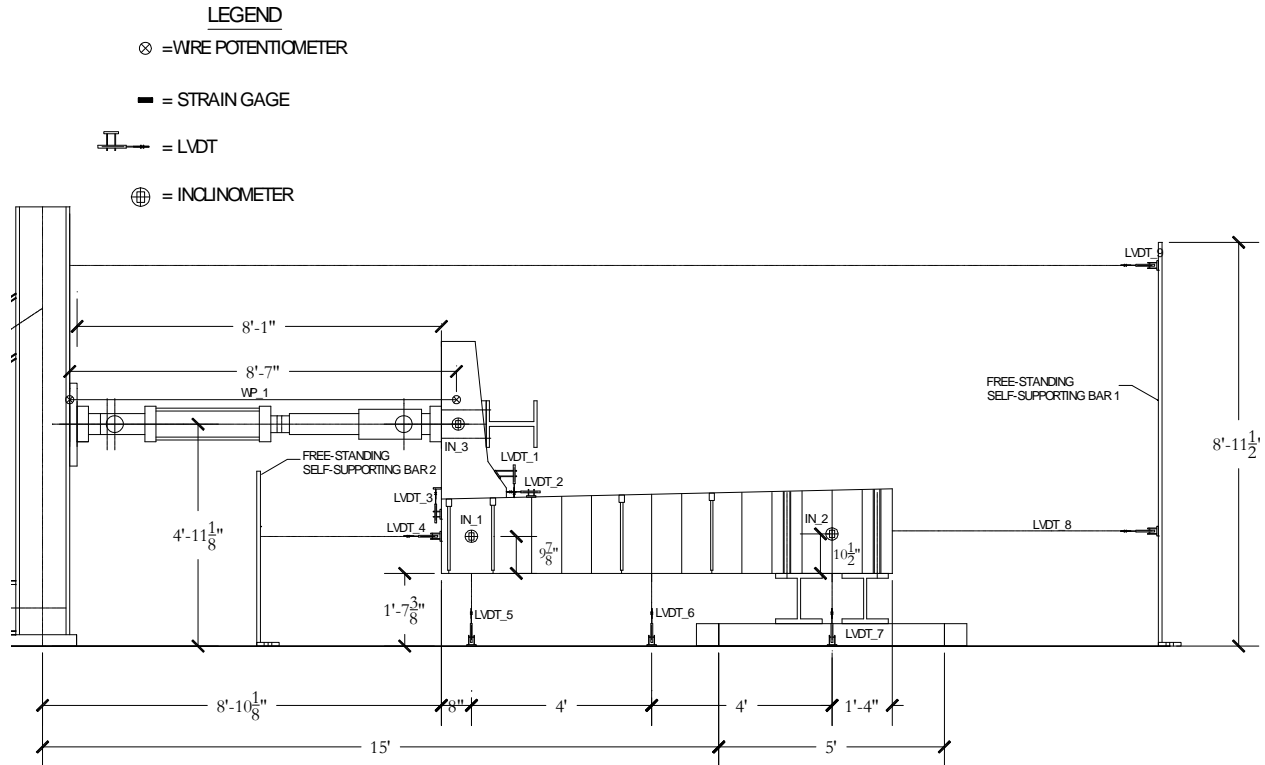


Fig. 6.1-3

These gages were set-up primarily to capture the micro-displacements within each component of the structure.

On a larger scale, the total structural displacements as well as entire component displacements were measured by using external gages mounted to the specimen. The *theoretical* overall specimen displacements were qualitatively considered, and checked by implementing gages to compare with *actual* overall specimen behavior Fig. 6.1-4.



TEST STRUCTURE INSTRUMENTATION

Fig. 6.1-4

The external specimen displacement were to be measured using devices capable of recording displacements in the order of 0.5"-12", and also inclinometers to capture the flexural rotation. For large-scale movement between the fixed end of the load actuator connected to the K-frame and the parapet under displacement, a wire potentiometer was instrumented between these two points; this was a good means of measuring large displacements. The inclinometers were to be fixed to the parapet to get its flexure, the free-rotating deck section directly under the parapet inclinometer, and at the fixed end of the deck as a check measure for possible uplift of the supports.

To detect slippage of the system, movement of the K-frame, elongation of the specimen, gap opening of the concrete and flexural displacement of the deck, Linear Voltage Displacement Transducers (LVDTs) were to be used. They were considered to be more adept at recording smaller displacements with higher levels of output resolution and accuracy than the wire potentiometers.

With the aid of all the gages the component displacements could be found and compared to the total displacement according to the theoretical relationships developed. The inclinometer rotation measurements were to be coordinated with the LVDT displacements, in order to determine the component of pure flexure of the parapet.

4.6.2. Preparation

The Instrumentation phase primarily dealt with the preparation of the rosettes and the rebar gages. The gages for the reinforcement bars were 120-ohm unidirectional glue-able gages, and the rosettes were 350-ohm gages.

The rosettes were specially prepared for implementation in the deck because of the high temperature issues associated with the fabrication, and the fact that the gages were to be place between the layers of fiberglass. In order to protect the gages from yielding due to strains present when the deck was fabricated special high temperature resistant composite 'wafers', 2"x2" were specially cut in order to mount the gages on them to protect them in the handling phase.

Each gage had to be bonded to the composite chip using specific gauging methods, and preparatory procedures as follows:

Step 1. The wafer surface had to first be prepared by applying a degreaser to remove impurities, and totally degrease the surface to promote good adhesion between the surface and the gage.

Step 2. The wafer surface was then dry abraded with 220- or 320-grit silicon-carbide paper to remove scale or oxides, then a surface conditioner was applied and wet abrading was carried out using 400-grit silicon-carbide paper. The residue was removed with gauze, by wiping in a single direction to prevent re-deposition of contaminants.

Step 3. Following the last stage, the gage area had to be prepared by applying a neutralizer and scrubbing with a cotton swab. The neutralizer was removed by wiping in a single direction with gauze.

Step 4. The gage was then removed from the package by using tweezers, and handled thereafter by covering with cellophane tape and positioned into place by setting down one edge of the tape on the wafer and pressing the gage unto the surface, in a smoothing out manner.

Step 5. The tape was then lifted using a shallow angle of lift, and the terminal, surface and back of gage was coated with the adhesive. Immediately following, the tape was smoothed back into place by using a gauze pad and wiping the gage back unto the surface.

Step 6. A silicone gum pad and aluminum backup plate was placed over the gage installation. The silicon pad was used to distribute the force of metal clamps used to set the bond between the wafer surface and gage. (The gages were placed in a furnace at expected temperatures of 250 degrees Fahrenheit for approx. 2.5 hours)

Step 7. After curing the pad and backup plate was removed and the tape was carefully peeled off the gage, and gauging was complete (Adapted from *Strain Gage Applications with M-Bond AE-10,AE-15, GA-2 Adhesive Systems* Measurements Group Inc).

These gages also required high temperature wire, which had to be soldered to the connection tabs of each gage. Soldering basically requires beads of rosin-core flux to be deposited on each tab that secures the wire leads to each gage. There would be 6 connections for each rosette comprising three (3) wires.

The rebar gages use a similar preparation phase before being glued on the rebar. First off the rebar needed to be ground to create a constant continuous surface free of ridges, and or bumps with as smooth a finish as possible without losing too much section of the steel.

4.6.3. Specimen Gaging

The deck was gauged on site at the Hardcore Composites Inc. production plant in Delaware. All the prepared gages were taken to the plant and calculations were done to assess the lengths of wire needed for the gauging process, such that there was sufficient excess for connecting to external data recording devices. The actual material was a woven fiberglass cloth, which had to be parted so that the gages could be placed at assigned locations within the deck. The flanges were 6 layers thick, and the webs 3 layers thick. Each gage was set in place and the high temperature wire was run along the seams and out to the corner of the deck. The high temperature wire was necessary since the temperature of the deck gets close to 300 degrees Fahrenheit when the fiberglass is infused with the resin.

For each deck there were:

- 2 rosettes in the top panel
- 2 rosettes externally mounted to the bottom flange
- 5 rosettes in specific webs of the deck
- 1 unidirectional gage mounted to the outer web of the deck on the parapet end
- 4 rebar gages inside the deck

For the parapet there were:

- 4 rebar gages placed on the vertical rebar that made the connection from parapet to deck
- 2 concrete gages on the external faces of the parapet
- The proposed setup will have:
- 1 wire potentiometer

- 9 linear voltage displacements transducers
- 3 inclinometers

Figure 6.3-1 shows all the gages used on a test piece, and the assigned channel numbers that each gage will have as they are connected to a data acquisition device for data processing.

INSTRUMENTATION DETAIL				
FRP Parapet to RC Deck Project				
Channel #	Gage ID	Location	Gage Type	Remarks
1	SR_1	Web of bottle 1 (vertical)	Strain Rosette	
2	SR_1	Web of bottle 1 (diagonal)	Strain Rosette	
3	SR_1	Web of bottle 1 (horizontal)	Strain Rosette	
4	SR_2	Web of bottle 1 (horizontal)	Strain Rosette	
5	SR_2	Web of bottle 1 (diagonal)	Strain Rosette	
6	SR_2	Web of bottle 1 (vertical)	Strain Rosette	
7	SR_3	Web of bottle 1 (horizontal)	Strain Rosette	
8	SR_3	Web of bottle 1 (diagonal)	Strain Rosette	
9	SR_3	Web of bottle 1 (vertical)	Strain Rosette	
10	SR_4	Web of bottle 2 (vertical)	Strain Rosette	
11	SR_4	Web of bottle 2 (diagonal)	Strain Rosette	
12	SR_4	Web of bottle 2 (horizontal)	Strain Rosette	
13	SR_5	Web of bottle 3 (horizontal)	Strain Rosette	
14	SR_5	Web of bottle 3 (diagonal)	Strain Rosette	
15	SR_5	Web of bottle 3 (vertical)	Strain Rosette	
16	SG_11	Web of bottle 2 (vertical)	Strain Gage	
17	A1	Top flange of bottle 4 (parallel to parapet)	Strain Rosette	
18	A2	Top flange of bottle 4 (diagonal to parapet)	Strain Rosette	
19	A3	Top flange of bottle 4 (perpendicular to parapet)	Strain Rosette	
20	B1	Top flange of bottle 1 (parallel to parapet)	Strain Rosette	
21	B2	Top flange of bottle 1 (diagonal to parapet)	Strain Rosette	
22	B3	Top flange of bottle 1 (perpendicular to parapet)	Strain Rosette	
23	C1	Bottom flange of bottle 4 (parallel to parapet)	Strain Rosette	
24	C2	Bottom flange of bottle 4 (diagonal to parapet)	Strain Rosette	
25	C3	Bottom flange of bottle 4 (perpendicular to parapet)	Strain Rosette	
26	D1	Bottom flange of bottle 1 (parallel to parapet)	Strain Rosette	
27	D2	Bottom flange of bottle 1 (diagonal to parapet)	Strain Rosette	
28	D3	Bottom flange of bottle 1 (perpendicular to parapet)	Strain Rosette	
29	SG_1	Interior face of concrete parapet (20" from side)	Strain Gage	
30	SG_2	Exterior face of concrete parapet (20" from side)	Strain Gage	
31	SG_3	1" up O.C. on re-bar 13.75" from back wall of parapet 20" O.C. in from side	Strain Gage	
32	SG_4	3" down O.C. on re-bar. 13.75" from back wall of parapet 20" O.C. in from side	Strain Gage	
33	SG_5	3" down O.C. on re-bar. 2" from back wall of parapet 20" O.C. in from side	Strain Gage	
34	SG_6	1" up O.C. on re-bar. 2" from back wall of parapet 20" O.C. in from side	Strain Gage	
35	SG_7	1" up O.C. on re-bar 13.75" from back wall of parapet 4" O.C. in from side	Strain Gage	
36	SG_8	3" down O.C. on re-bar. 13.75" from back wall of parapet 4" O.C. in from side	Strain Gage	
37	SG_9	3" down O.C. on re-bar. 2" from back wall of parapet 4" O.C. in from side	Strain Gage	
38	SG_10	1" up O.C. on re-bar. 2" from back wall of parapet 4" O.C. in from side	Strain Gage	
39	WP_1	Mounted on inner flange of K-frame to top of parapet	Wire Potentiometer	Range +/-12"
40	LVDT_1	Mounted on deck with displacement measure against parapet	Linear Voltage Displacement Transducer	Range +/-1"
41	LVDT_2	Mounted on parapet with displacement measure against deck	Linear Voltage Displacement Transducer	Range +/-0.5"
42	LVDT_3	Mounted on cantilevered end of deck at deck-parapet interface	Linear Voltage Displacement Transducer	Range +/-0.5"
43	LVDT_4	Mounted on cantilevered end of deck to inner flange of K-frame	Linear Voltage Displacement Transducer	Range +/-0.5"
44	LVDT_5	Mounted at 8" in from cantilevered end of deck to floor	Linear Voltage Displacement Transducer	Range +/-5"
45	LVDT_6	Mounted at 4'-8" in from cantilevered end of deck to floor	Linear Voltage Displacement Transducer	Range +/-3"
46	LVDT_7	Mounted between supports to floor	Linear Voltage Displacement Transducer	Range +/-0.5"
47	LVDT_8	Mounted to deck from fixed to self-supporting bar	Linear Voltage Displacement Transducer	Range +/-1"
48	LVDT_9	Mounted to self-supporting bar to inner flange of K-frame	Linear Voltage Displacement Transducer	Range +/-1"
49	IN_1	Mounted to cantilevered end of deck below parapet	Inclinometer	Uni-directional
50	IN_2	Mounted on deck at position between supports	Inclinometer	Uni-directional
51	IN_3	Mounted on parapet at approx. center-line of actuator	Inclinometer	Uni-directional

Fig. 6.3-1

4.7. Construction Of Set-Up

The construction involved in the preparation of the specimen took 3 main forms:

Strain Rosettes = 9
Concrete Strain Gages = 2
Reinf. Strain Gages = 9
Wire Potentiometers = 1
LVDTs = 9
Inclinometers = 3
Total # of Gages = 33

1. Construction of the deck
2. Construction of the parapet
3. Construction of the entire test configuration

The deck manufacturers, Hardcore Composites Inc. in Delaware, undertook deck construction and this was done at their plant. The parapet construction was in progress at the time of writing this paper, and assembly of the test specimen was yet to come.

4.7.1. Deck Construction

In the report on Salem Avenue Bridge Deck Investigation, by Mark Henderson, P.E., Hardcore's deck construction was described. The deck consisted of a foam-core "sandwich" panel manufactured with the (Seemann Composite Resin Infusion Molding Process) SCRIMP™ process. The sandwich core consists of foam blocks (8"x8"), wrapped with glass fiber cloth. The lattice of non-structural (does not add to strength of system) foam blocks are used to maintain the shape of the core section until the resin infiltrates all the layers of glass fiber. The lattice of fiber-reinforced webs consists of 3 sheets of glass fiber cloth, and the flanges are 6 layers of the glass fiber cloth, which all become consolidated upon infusion to produce a 0.144" web and flanges that are 0.432" thick. The panels made were usually 8' wide, but for testing purposes they were made 4'x10'. Connectors for the parapet are made by placing threaded reinforcement bars in the material before infusion on the edges of the panel where the parapet would be. The bars are set in the seams where four webs coincide, so that upon infusion the bar becomes locked into place, hence giving it, what is considered to be, adequate development length. A pair of bars at each reinforcement location is connected to the bars in the deck, as provided by Hardcore so that the parapet could be attached. Fig. 7.1-1 shows one of the decks used for testing, and the parapet reinforcement can be seen in the deck foreground.

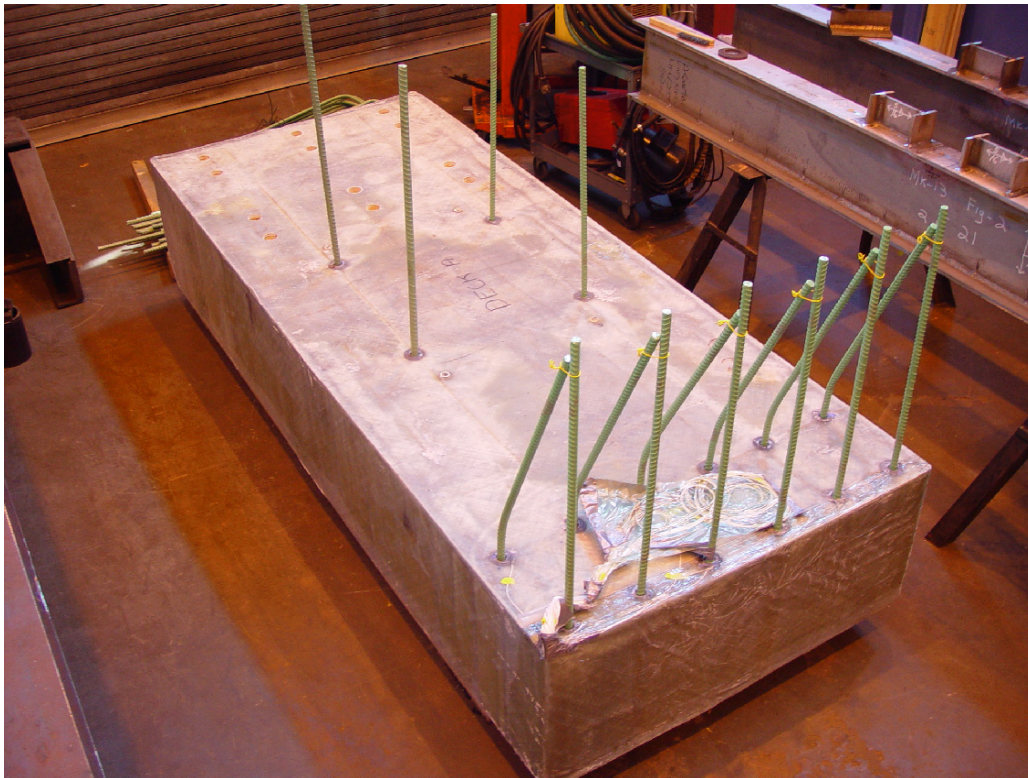


Fig. 7.1-1

4.7.2. Parapet Construction

The parapet construction was undertaken at the ATLSS center and various components had to be ordered and obtained from external sources for construction.

The first thing that was required was reinforcing steel bars, which were purchased from Re-Steel Co., Eddystone, PA. The reinforcing steel, Fig. 7.2-1, was needed to build the reinforcement cage to strengthen the parapet against shear and moment.



Fig. 7.2-1

After the construction of the reinforcement cage, the next thing was building of formwork to create the required parapet shape to form the concrete parapet. This took a lot of man power and labor, wood needed to be cut to size and measure against the specimen to ensure correct dimensioning. The forms were nailed together using 8d nails, and 3" masonry drywall screws, and the design was braced against forces exerted by the concrete mix so that there would not be any bowing of the form. In constructing the forms special consideration had to be made for the through bolts that were to be placed through the parapet for the connecting of the actuator plate. Forming reinforcement was not to coincide with the hole layout for the plate connection. The unevenness of the deck was also an issue, and gaps in the forms would cause the concrete to seep out, so a proposed solution was the use of caulking.

The final step was the concrete mix design. It was important to simulate the mix used on the actual bridge, and this phase was in progress at the time of writing. The mix design class was AASHTO design for Class "AA" Cement Concrete. The mix had an average 7-day compressive strength of 4457 psi and 28-day strength of 5627 psi. Local suppliers who had experience doing Penn DOT concrete work submitted mix designs approved for the same class, but there were differences, so a decision on which design to use was not arrived at yet. The proposed designs were forwarded to Penn DOT engineers for approval based on constituent properties (e.g. pozzolan selection, fly ash compare with blast furnace slag).

4.7.3. Test Set-Up Construction

This was the last phase in the construction process, and was assigned to the laboratory construction crew. This involves the preparation of the details designed in section 4 and the assembly of the entire test configuration. Work in this area had yet to be done.

4.8. Conclusion

The main objective of the research testing was to assess the reliability and behavior of the connections between a standard reinforced concrete parapet and a new bridge design using glass fiber reinforced composite material. Based on analysis the test design was chosen as a fixed end-cantilevered model to achieve practicality in testing. The test would apply a constant static rate of displacement on the parapet so as to induce failure in the mechanism,

preferably at the connections. The simulation was supposed to give information regarding the design capacity of this new type of bridge system in handling the load of a vehicular impact. From calculations done the mode of failure was predicted to come from the connections, such that the deck is undamaged and only the connections and the parapet is affected. The extent to which the connections fail should give an idea of whether or not new connection details should be designed for FRP decks.

The instrumentation chosen was configured to give an idea of the load displacement characteristics of the actual bridge system under impact. The information that is expected to come from the tests is expected to provide Penn DOT in particular with information regarding the maximum load capacity for the parapet and connections, and also the maximum displacement before failure ensues. From an engineering perspective this information is important for design work, however the implications of this test are more widespread. The data collected may be used in further empirical testing so that AASHTO may use the results to propose standardized designs when FRP material is used in bridge construction as it relates to railing designs. There is also a lot that is unknown about the material characteristics of FRP material in bearing typical loads associated with the concrete decks in bridges.

The scope of this research is expected to go into using the strains and displacements acquired to develop stress strain relationships for the deck material, and to verify for the most part **tensile** and **compressive** strengths by material testing. After the testing of the two panels according to Penn DOT's requirements further testing on two additional panels will be done to assess modified deck systems and connection types to improve on the existing design. As is, Hardcore's construction is quite elaborate and not easily reproducible, however information that could lead to a simple more efficient deck design capable of meeting existing standards assigned to the alternative bridge systems, would aid in the development of better FRP designs and standardization within the industry. It is hoped that if a bridge is made of FRP material then there would be a standard in AASHTO design for the bridge capacity, section properties, material properties and so on.

4.9. Acknowledgements

My thanks go out to everyone who had an input into the writing of this paper. In the compiling of data and calculations, assistance with construction and materials acquisition, advice on engineering practices and in general for support and encouragement. I must thank my fiancée and God for inspiring me to give the best of myself and without whose input this would not be possible.

I would like to specially acknowledge:

Clay J. Naito PhD, P.E. (Primary Advisor, P.I.)

Mr. Robert P. Alpago, P.E. (Secondary Advisor)

Mr. Seoksoon Lee (Graduate Student Advisor)

Mr. Carl Bowman (Instrumentation Technician)

Mr. John Hoffner (Laboratory Foreman)

4.10. References

AASHTO Standards 2000. Section 13-Railings

Cassidy, Patrick A. 2000. Fiber-Reinforced Polymer Bridge Decks. J. Muller International Chicago, IL.

Federal Highway Administration, U.S. Department of Transportation.

Henderson, Mark P. 2000 Salem Avenue Bridge Deck Investigation: Issues Regarding the Composite Material Deck Systems.

Pennsylvania Department of Transportation.

Measurements Group Inc. Strain Gage Applications with M-Bond AE-10, AE-15, GA-2 Adhesive Systems.

Section 5: Blast Testing, State of the Practice by Justin McCarthy

Advisor: Clay J. Naito, Ph.D., P.E.

5.1. Project Summary

This project focuses on the characteristics of explosive loading of structures and the work that has been accomplished in this field. A basic description of blast as it pertains to structures is given. The effects produced by blast i.e. blast overpressure, shock loads, and fragments are described. The details of associated dangers such as glass projectiles, brisance, progressive collapse, and smoke inhalation are discussed. The paper continues with an overview of current government and non-government test facilities and experts in the field of blast testing. There is a description of current testing technologies namely the shock tube and Split-Hopkinson Bar for material testing. Finally, the concerns with constructing university test facility are expressed.

5.2. Background

The need for a blast testing facility comes from the recent terrorist actions on U.S. soil and U.S. embassy buildings abroad. The World Trade Center bombing in 1993, the Oklahoma City bombing in 1995, the attacks on U.S. embassies in Kenya and Tanzania in 1998, and most recently the World Trade Center attack of 2001 have demonstrated the weakness in physical security of structures. Further studies on blast wave characteristics and their interactions with structures must be performed to improve the safety of individuals inside buildings and to preserve the integrity of the structure itself.

The majority of testing has been performed under the curtain of the Department of Defense. University blast testing facilities must be developed to provide more information on the behavior of blast loads on structures. Dangerous effects such as brisance, progressive collapse, and projectiles must be investigated further to enhance structural integrity of buildings and provide sufficient safety measures for the people inside of them.

5.3. Summary of Blast Wave Characteristics

A basic understanding of blast wave characteristics is necessary for testing the behavior of structures under explosive loadings. Army Technical Manual TM5-1300 “Structures to Resist the Effects of Accidental Explosions” [1] gives valuable information on blast wave characteristics. It describes the three parts involved in testing and types of protective structures. Scaling is an essential component in testing structures for blast. Scaled parameters are constantly used in the design of structures against blast loads. The different types of explosions must be understood to recognize the correct blast environment. Furthermore, pressure design ranges and the pressure vs. time relationship are important factors in blast design.

5.3.1. Systems and Protective Structures in Blast Testing

Army Technical Manual TM5-1300 “Structures to Resist the Effects of Accidental Explosions” defines three main systems in blast testing. These are the donor system, the acceptor system, and the protection system. The donor system is made up of the potentially detonating explosive. This depends on the amount, type, and location of the explosive. The acceptor system consists of personnel, equipment, and other explosives requiring protection from the dangers of an explosive donor system. Finally, the protection system is the protective structure designed to prevent or limit damage to the acceptor system. This includes shelters, barriers, containment structures, etc.

Impact loads are the primary cause of acceptor system explosion. From an economic viewpoint, protection can be afforded through the use of distance and/or protective structures. Equipment can usually withstand higher pressures (shock impact) and can be isolated or secured to the floor.

Protective structures consist of three types of structures. A shelter is designed to fully enclose the acceptor system. Another type of structure is a barrier. The barrier acts as a shield between the donor and acceptor systems. The most expensive protective structure is the containment structure. This fully or near fully encloses the donor system, limiting the spread of primary and secondary fragments into the acceptor system.

In general, human tolerance to blast pressure is relatively high. However, the orientation of the person to the blast wave influences the magnitude of injury. Standing, sitting, prone, face-on, and side-on to a blast wave all determine the amount of damage caused by an explosion. The critical targets in human beings are air-containing tissues of the lungs. A pressure blast of 100-120 psi can be fatal. Pressures are also amplified by a phenomenon

known as the “jetting effect.” Pressures passing through and opening may increase several times the magnitude of the average pressure [1].

5.3.2. Scaling Blast Tests

The main idea behind explosive scaling is that two different weight TNT explosives generate the same overpressure on an object but they do so at different standoff distances [2]. Essentially, a smaller bomb must be placed closer to a structure for it to experience the same effects as a larger bomb. Research conducted by Hopkinson in 1915 and by Cranz in 1926 revealed that a blast wave can be scaled based on the amount of explosive and distance from detonation [3]. This scaled distance parameter is created from the weight of the bomb and distance from the detonation. Equations and charts may be defined for the peak overpressure using this scaled distance parameter and applied using an explosive of any mass. The scaled distance parameter Z is defined as:

$$Z = R/W^{1/3}$$

Where R is the distance from the center of the explosion to the structure, and W is the weight of the explosive in pounds of TNT. Explosives other than TNT can be multiplied by TNT equivalency factors to determine their blast overpressures on structures [4].

5.3.3. Types of Explosions

The two types of blast loads encountered are unconfined and confined. Unconfined blasts are further broken down into free air blasts, air bursts, and surface bursts. Confined blasts may be fully vented, partially confined, and fully confined [1].

5.3.3.1. Unconfined:

- Free air blast – blast that occurs in the air and the shock wave is not reflected
- Air burst – shock wave is reflected prior to arrival at protective structure
- Surface burst – explosion is near or on the ground surface so that the initial shock wave is amplified at the point of detonation due to ground reflections

5.3.3.2. Confined:

- Fully vented – one or more surfaces of the protective structure is open to the atmosphere
- Partially confined – produced within a barrier structure with smaller sized openings and the initial shock wave is amplified by frangible and/or nonfrangible portions of the structure (frangible elements are ones that will yield due to blast overpressures)
- Fully confined – associated with total or near total confinement of the blast within a protective structure

For unconfined explosions, negative blast wave parameters need to be considered in the design of flexible protective structures. This includes steel-frame structures. On the other hand, these parameters need not be considered in more rigid structures such as reinforced concrete [1].

5.3.4. Pressure Design Ranges

There are three areas of concern when considering the dynamic response criteria used in design. The properties of the donor location, namely its type, weight, shape, and casing along with its location with respect to the acceptor system must be considered. Also, the sensitivity (tolerance, “fragility level”) of the donor system plays a role. The “fragility level” is defined as the magnitude of shock (acceleration) that equipment can sustain and remain operational. Finally, the physical properties and configuration of the protective structure should be taken into account [1].

There are two types of design ranges when designing for accidental explosions [1]. These types are high pressure and low-pressure design.

5.3.4.1. High Pressure Characteristics

- High initial pressure, amplified by reflections in structure
- Applied load durations are short

- Structures need to be designed for impulse (area under pressure vs. time curve) rather than maximum pressure associated with longer durations
- Fragments have high initial velocities
- “Spalling” of concrete may occur which is the disengagement of concrete cover over the reinforcement on the acceptor side resulting in danger to personnel and/or equipment

5.3.4.2. Low Pressure Characteristics

- Sustain peak pressures of smaller intensity
- Longer applied load duration which may exceed response time of structure, which is the amount of time it takes before the structure comes back to rest
- Depends on both the maximum pressure and the impulse

5.3.5. Typical Pressure vs. Time Curve

A typical pressure pulse profile is shown in Figure 1(a). It represents a jump discontinuity from the ambient pressure up to the peak static overpressure. The pressure decays exponentially with time below the ambient pressure due to the over expansion of gases. A change in momentum is known as impulse [5]. It is calculated as the product of force and time. The units for impulse of blast loading is typically psi-ms. The impulse of a blast pressure wave is calculated by integrating the area under the positive phase of the pressure-time curve.

The actual pressure-time curve for distributed pressure load acting on an element is highly irregular because of multiple reflections within the structure. Therefore, a fictitious peak triangular pulse may be used as an approximation for design purposes.

For design purposes, this pressure vs. time relationship is simplified into three linear segments shown in Figure 1(b). Figure 1(b) can be calculated for any detonation given the quantity of explosive, distance to the structure, and orientation of the structure relative to the blast [1].

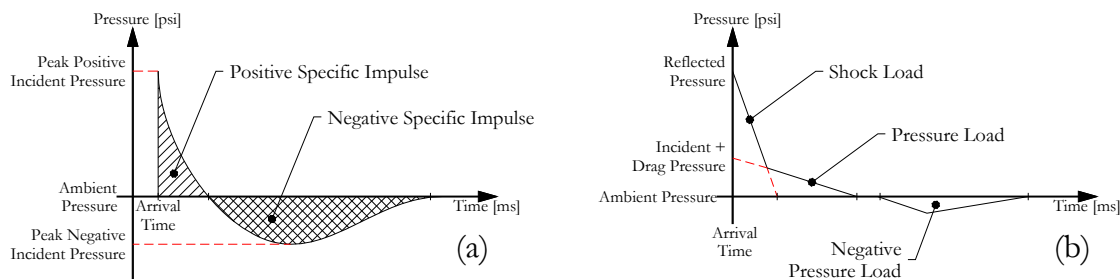


Figure 1: Actual and Ideal Pressure vs. Time Blast Curves

5.4. Summary of Blast Components

When an explosion occurs, it consists of different parts. These include the blast overpressure, shock loads, primary and secondary fragments, and a phenomenon known as the Mach front. All of these components affect the response of a structure and must be taken into consideration when designing for an explosive event.

5.4.1. Blast Overpressure

The blast overpressure is pressure wave that results from the detonation of an explosive. The chemical reaction produced by an explosion releases a large amount of gas in a short period of time resulting in a blast wave. The surrounding air is forced out by the violent expansion of gases. A layer of compressed air forms in front of the gases. This layer is known as the blast wave and contains most of the explosion’s energy. The blast pressure falls a little below ambient pressure levels as cooling and expansion continue because gas particle velocities cause a slight over expansion before their loss of momentum. [6]

These blast waves are amplified in pressure due to reflections with the nearby ground surface producing the blast overpressure. It poses a great threat to structural integrity. When this overpressure reaches a structure, the

distributed load is applied impulsively. This load is applied over an extremely short time period and is considered an instantaneous impulse [7]. See Figure 2 for a typical blast-loading environment.

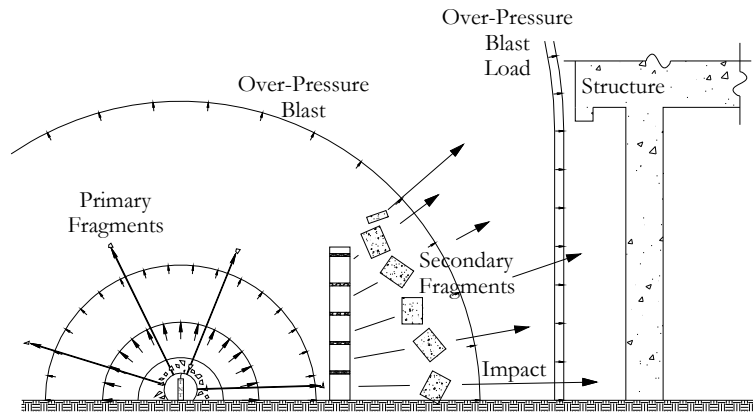


Figure 2: Typical Blast Loading Environment

When a blast wave strikes an object, it generates a pressure greater than the peak static overpressure on the face of the object. This occurs because air molecules are brought to rest and compressed further by the collision. Peak static overpressure is essentially the pressure felt by a particle moving with the blast wave. Another pressure, dynamic pressure must also be considered. Dynamic pressure q is defined as:

$$q = 1/2\rho u^2$$

where ρ is the density of air immediately behind the wave front and u is the particle velocity. Therefore, the total pressure experienced on the face of the object is the sum of peak static pressure and dynamic pressure [2]. This pressure is known as peak reflected pressure.

5.4.2. Shock Loads

When explosions occur inside an enclosed structure, extremely high peak pressures and impulses are associated with the shock front [1]. These pressures and impulse are further amplified within the structure. The configuration and size of the structure, explosive charge weight, and charge location are all necessary parameters for the determination of average shock loads.

A protective structure experiencing high intensity shock pressures may be designed for impulse rather than peak pressure only if the applied pressure duration is short compared to the structure's response time. A rule of thumb to follow is if the time to reach maximum displacement is less than or equal to 3 times the load duration, then design against peak pressure controls rather than impulse [1].

5.4.3. Fragments (Primary and Secondary)

The explosion of the cased donor charge produces fragments. Primary fragments are the pieces of the charge casing itself. Because of their light mass (~ 1lb), they are characterized by extremely high velocities on the order of thousands of feet per second. In terms of structural performance, they are usually neglected due to their small size [1].

Secondary fragments are produced when the blast overpressure reaches other surrounding objects. At close distances the shock load magnitude is very high and may result in objects being broken up or forcibly removed their supports. Secondary fragments can weigh up to a few hundred pounds and travel at speeds of over 100 ft/s. Damping affects the blast overpressure more than the fragments causing secondary fragments to reach the structure first. Piercing of the structure is possible before arrival of the blast wave resulting in further degradation of structural integrity [1].

5.4.4. Mach Front

During an airburst, the phenomenon known as the “Mach” front is formed by the interaction of initial shock waves with reflected waves. For design considerations, variations in pressure over height are neglected. The pressure vs. time plot for the Mach front is similar to that of initial shock waves but larger in magnitude. The path of the triple point is defined as the intersection of the initial shock waves, reflected waves, and Mach front waves. If the height of the triple point is not above the height of the protective structure, then the magnitude of loads will vary with the height of the point being considered [1].

5.5. Dangers From Blast

When an explosion occurs, it creates dangers for both human and structural safety. Fragments such as pieces of concrete, glass, and any surrounding objects threaten the safety of people inside the building as well as other building components such as walls. Smoke inhalation also creates a hazard for building occupants. Structural integrity can be endangered by a phenomenon known as brisance, which will be discussed in more detail. Also, reverse loading of slabs and progressive collapse compromise a structure’s reliability.

5.5.1. Personnel Safety/Hazard Issues

5.5.1.1. Fragments:

A detonation creates fragments as discussed earlier. These fragments may be part of the explosive casing (primary) or pieces of surrounding material (secondary). In the case of large explosions such as the Oklahoma City bombing, primary fragments are usually not of concern to human safety. The larger secondary fragments pose a much greater threat. Pieces of concrete, office equipment, and especially glass cause the majority of injuries in an explosive event.

5.5.1.2. Glass Shards:

Besides injuries from the blast pressure wave itself, pieces of flying glass are responsible for the majority of injuries. Direct glass-related injuries occur from glass shards flying from fractured windows causing lacerations and abrasions. Secondary glass-related injuries occur when the shock wave passes into the building causing hearing injuries [8]. Normally, blast pressures propel glass shards at speeds in excess of 30 m/s (100 ft/s) [9].

A study conducted on glass-related injuries revealed that over half of all glass-related injuries besides those in the Murrah Building occurred between 60-120 meters away from the detonation. The 4000 lb. ammonium nitrate fuel oil mixture generated a blast wave powerful enough to demolish the curtain wall of the Murrah Building and shatter nearly every window in buildings within a one and one-half block radius [8]. The danger associated with glass shards has encouraged the development of many standard tests for glazing systems under airblast loadings. These include Glazing and Glazing Systems Subject to Airblast Loadings [10], Determining Load Resistance of Glass in Buildings [11], and Structural Performance of Glass in Exterior Windows, Curtain Walls, and Doors Under the Influence of Uniform Static Loads by Destructive Methods [12].

5.5.1.3. Smoke and the “Stack” Effect:

Smoke inhalation during an explosion causes a major threat to the health and safety of building occupants. During the World Trade Center bombing of 1993, most injuries were respiratory injuries because of smoke travel through ruptured vertical shafts driven by the stack effect [13].

The stack effect in buildings works much like a chimney does in a home. It is the pressure difference between the inside and outside of a building [14]. If the building has openings at high and low elevations, a natural flow occurs. If air inside the building is warmer than air outside, warm air will float out the top and be replaced by cooler air through the bottom opening. If air inside is cooler, air will flow out the bottom being replaced by warmer air through the top [15]. The stack effect depends on the ambient pressure, building height, and absolute temperatures inside and outside the building.

5.5.2. Structural Issues

5.5.2.1. Brisance:

Brisance is the measure of an explosive’s shattering power. It occurs when there is a rise to maximum pressure so rapid that it shatters any nearby material. This phenomenon is proportional to the speed at which the explosive releases its energy [16]. Brisance is a major concern for reinforced concrete structures.

An example of brisance is seen in the bombing of the Alfred P. Murrah Federal Building in Oklahoma City on April 19, 1995. Figure 3 portrays the aftermath of this explosion. For column G20 of the Murrah Building, $R/W^{1/3} = (15.6 \text{ ft})/(4000 \text{ lb})^{1/3} = 1.0 \text{ ft/lb}^{1/3}$ where 15.6 ft was the range to the center of the column. Studies done by McVay [17] in 1988 have shown that reinforced concrete walls can be removed by a phenomenon known as brisance at a value as high as $1.5 \text{ ft/lb}^{1/3}$. According to McVay, brisance would have occurred at a range of $R = (1.5 \text{ ft/lb}^{1/3}) * (4000 \text{ lb})^{1/3} = 23.8 \text{ ft}$ or less. It is likely that column G20 was destroyed by brisance since no signs of the column were found in the debris [18].



Figure 3: Alfred P. Murrah Building

5.5.2.2. Progressive Collapse:

Nearby column G24 was outside the likely range for brisance but was still highly loaded. The strength of this column was limited by its shear resistance at its ends, namely at the first and third floor slab connections. The deflection at column midspan was so great that the shear capacity was exceeded at the ends causing this column to fail in shear [18].

Column G16 was located at a slant range of 50 feet from the blast. The slant range is defined as the distance from the explosion to the column midheight. By performing an analysis similar for G24, column G16 was predicted to reach shear capacity and fail accordingly. On the other hand, column G12 also endured direct blast effects but remained intact. It was located at a slant distance of 89 feet from the blast and only 10% of its shear capacity was reached [18].

These columns G12, G16, G20, and G24 all supported a transfer girder, which distributed loads from the third floor columns and above. The failures of 3 out of these 4 columns lead to the failure of the transfer girder and building's subsequent progressive collapse. Specific techniques have been developed to design against progressive collapse. The General Service Administration has created the Progressive Collapse Design Guidelines. Analyses of two columns of the Alfred P. Murrah Federal Building were performed using the procedures of TM5-1300 [1] and the results are summarized below in Table 1. Data sheets and the procedure for calculating these pressures are summarized in Appendix A.

Column	Peak Pressure [psi]	Distance from Blast [ft]
G12	126	88.1
G20	714	49.0

The idealized pressure vs. time curves for columns G12 and G20 along with a plan view of the Murrah building are shown in Figure 4 below:

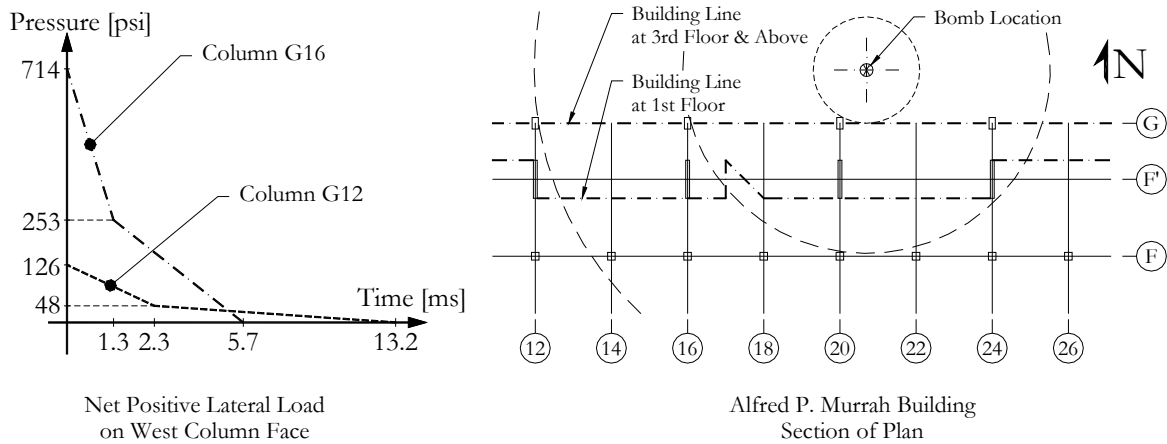


Figure 4: Idealized Pressure Curves for Columns G12 and G26

Furthermore, seismic building code provisions have been investigated to design against progressive collapse. A study conducted compared special moment resisting frames in areas of high seismic activity to ordinary moment resisting frames in low seismic areas using the 1997 Uniform Building Code. The study modeled building systems by removing certain columns and analyzing the structure for progressive collapse. Investigators came to the conclusion that using seismic codes does not necessarily prevent progressive collapse, but provides better protection than ordinary moment resisting frames. The benefits from using seismic provisions are that the ductile details force the beam to form plastic hinges before column failure and prevents collapse from spreading to adjacent bays in the structure [19].

5.5.2.3. Upward Loading of Slabs:

As blast loads enter a structure through shattered windows or failed curtain walls, floor slabs are loaded in an unusual fashion. The net pressure underneath the floor slabs is greater than the pressure loading on top. This creates a brief upward loading on the floor slab. Floor slabs are not designed for upward loading and can only handle a relatively small upward pressure. Furthermore, the uplift of slabs causes a brief tensile force in the supporting columns. Reinforced concrete columns are not designed to withstand the effects of bending and tension [20]. These members may be damaged from the tensile forces and lead to a progressive collapse of the structural system.

5.6. Current Test Facilities

There are a few facilities in the United States capable of testing structures under blast loads. Most of the full-scale tests are performed at government-operated facilities such as the NASA White Sands Test Facility in Las Cruces, NM. Most information regarding blast testing at these facilities is confidential, making it difficult for university researchers to profit from valuable information. However, there are a few privately owned facilities such as SRI International in Menlo Park, CA and Southwest Research Institute in San Antonio, TX. These facilities usually do not have the blast testing capabilities of government plants, but valuable information may still be gained.

5.6.1. Government Facilities

5.6.1.1. White Sands, Las Cruces, NM:

The NASA White Sands Test Facility in New Mexico is capable of full-scale open-air detonations but very costly to use [21]. Specific information regarding the equipment and test site is either classified or very difficult to retrieve.

5.6.1.2. AED, Tooele, UT:

The AED (Ammunition Equipment Directorate) Test Site (www.tead.army.mil) is located at the Tooele Army Depot in Tooele, Utah. The facility is designed to conduct tests and studies for improving methods for the handling and demilitarization of munitions and explosives. It consists of a central control building for protection of personnel and equipment. All other sites are controlled from this building. Four test pads are used for tests involving large amounts of explosives. A storage pad is utilized for storing munitions and explosives to be used in future tests. A deactivation furnace is part of the demilitarization process where the final burning of a munitions item occurs after exposing the explosive.

- Barricade Testing: These tests are monitored with instruments such as sound level microphones, blast pressure transducers, high-speed cameras, and temperature sensors. Tests are performed in a cubicle simulating an ammunition maintenance facility bay.
- Propagation Tests: This test is used to determine minimum safe separation distances for munitions. Donor rounds are detonated while observing propagation to nearby acceptor rounds at varying distances.

Variety of equipment and data analysis accuracy is as follows:

- Explosive air blast pressures – up to 10,000 psi
- High speed photography – 100 to 40,000 frames per second
- Data recording – one 16 channel FM and direct tape recorder with 80 kHz response, several oscilloscopes with cameras, and one 16 channel tape recorder with 20 kHz response
- Data analysis – analysis using Tektronics transient recorder
- Force measurements – up to 10,000 lbs. via load cell

5.6.1.3. Royal Military College of Science, Cranfield, UK:

The Royal Military College of Science (www.rmcs.cranfield.ac.uk) at Cranfield University in the United Kingdom has the ability to quantify loads acting on structures in a blast environment. They have the necessary equipment to measure, record, and analyze blast loads. The RMCS understands the principles of structural response to blast loading while using this knowledge to assess the response of real structures to terrorist events. Figure 5 displays an impact test on a wall.

The explosive range on campus has an open-air capacity limited to about 250 grams of HE. This capacity is a bit larger in their reinforced concrete containment building on the order of 1 kg of HE. These smaller explosive capacities generally confine the work to scale models of structures for which they measure blast pressure-time histories. Most of the structural response work is conducted on a university range about 40 miles from campus, on the edge of the Army training range of Salisbury Plain. Bigger charges may be detonated while assessing real structural response to blast [22].

For measurement, piezoelectric pressure transducers (from Kistler Instruments) are used. The data is then captured using a digital storage oscilloscope. Structural response is likely conducted at the larger range, however, it is likely that this type of experiment would be conducted on a UK Ministry of Defense Range. They would perform an arena test where several specimens may be tested with one large detonation [22].

The RMCS also offers courses on blast once a year. The courses offered include blast loading, blast and ballistic loading: structural response and design, and structural response to blast, ballistic and impact loading. They cover a variety of topics necessary for blast protection including blast waves in air, internal explosions, principles of scaling and modeling, protective design techniques, structural dynamics, stress wave propagation, and human response to blast loading (ref www.rmcs.cranfield.ac.uk).



Figure 5: Wall Impact Test at RMCS

5.6.2. Non-Government Facilities

5.6.2.1. SRI Menlo Park, CA:

SRI International (www.sri.com/psd/poulter) is one of the largest privately owned blast-testing facilities in the United States. The 480-acre site consists of three separate testing facilities run all year round. Figure 6 show these three facilities.

5.6.2.2. Area 1:

This facility is used primarily for large explosive tests. A natural earth bowl surrounds the 30-m-diameter firing area. A protective bunker is situated at the open end of the bowl housing the necessary data acquisition systems. Dozens of channels of instrumentation with buried cables connected to a hardened junction box are situated in this bunker.

5.6.2.3. Area 2:

Area 2: Smaller explosive tests are performed in this facility. It includes an 8-m by 23-m concrete test pad with a retractable A-frame shelter. Setup on the concrete pad is usually performed under the shelter for protection from weather and retracted during firing. A 9-m by 9-m by 4.5-m deep pool is used for underwater tests. A 4-kbar explosive loader uses controlled venting of explosive gases to produce pressure pulses up to 400 MPa (60 ksi) with rise times ranging from 0.5 ms to 100 ms. Also, a 150-mm-bore (6 in.) pneumatic gun is used for propelling projectiles up to 500 m/s.

5.6.2.4. Sample Experiment: Turbine Fragment Impacts on Containment Structures

The hubs of electrical generator turbines were launched into scale-models of steel and reinforced concrete barriers. The hub fragments ranged from 1 to 12 kg and velocities varied from 125 to 200 m/s. Piercing and blunt impact orientations were also considered. The varying target (barrier wall) parameters included wall thickness, amount of reinforcement in the concrete and steel plate construction. The data analysis helped improve design formulas for barrier design. Figure 7 exhibits this experiment.

5.6.2.5. Area 3:

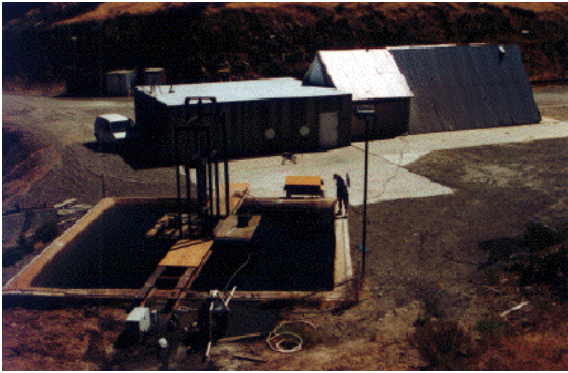
A 2.4-m-diameter (8 ft), 78-m-long (257 ft) shock tube is used to test structures up to 1-m wide at pressures up to 760 kPa (110 psi). A smaller shock tube measuring 0.6-m in diameter (2 ft) and 15-m long (50 ft) is used to develop unique airblast environments for use in the larger shock tube. A gas-propelled rail-sled apparatus is used for launching aircraft or other models weighing up to 100 kg at velocities up to 175 m/s or 50 kg up to 250 m/s. A natural gas pipeline test facility is utilized for assessing the effects of detonation of gas from accidental releases.

5.6.2.6. Sample Experiment: Air Blast Loading of Reinforced Concrete Walls

A series of 1/8-scale reinforced concrete walls varying in design were performed using a detonation of a methane/oxygen gas mixture. The mixture was detonated inside a rectangular shock tube applying a pulse of uniform pressure. This type of testing applies an essentially uniform flood pressure load. This type of distribution experiences an exponential decay over the entire wall, and the shock sweep time is extremely short. Movies were taken to depict the two-way bending, rupture at the floor and roof, formation of a vertical hinge, and the breaking loose of the wall at its ends. A picture of this experiment is shown in Figure 7.



Area 1

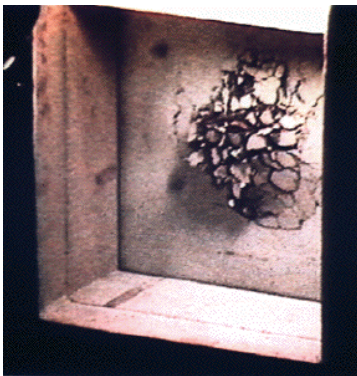


Area 2

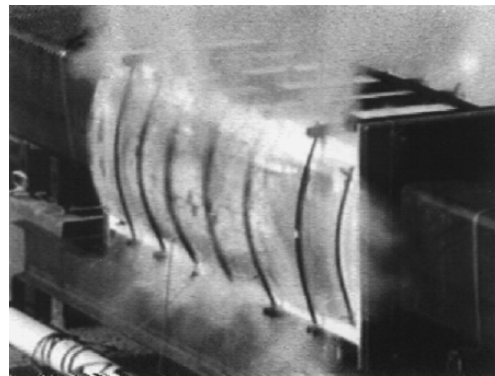


Area 3

Figure 6: SRI Facilities



Area 2



Area 3

Figure 7: SRI Sample Experiments

5.6.2.7. Southwest Research Institute, San Antonio, TX:

The Southwest Research Institute (www.swri.org) is located in San Antonio, TX covering 1,200 acres and employing more than 2,700 people. The SWRI facility and a sample experiment are shown in Figure 8. The Institute conducts work for both industry and government clients. SWRI is extensively involved in blast research. Some of areas of concern include blast containment design, explosion hazards evaluation, and fragmentation and debris dispersion measurement and prediction. They are also involved in impact shield design and testing along with measurement of ballistic and explosive events.

The blast facilities at Southwest Research Institute include a ballistic and explosives test range, remote test sites, and testing capabilities up to 1,000 lbs of high explosive (HE). Their experience in blast containment design includes

design, fabrication, and testing of portable demilitarization containers; design, fabrication, and testing of 22-lb. HE chambers; and studies on chamber life extension.

The explosion hazards evaluation research area deals with the fundamentals of explosions, development of software, fragment impacts, prediction of human injury, and safety/hazard analyses. Experience in this field includes predicting source of car bombs, hazards evaluation of HE facilities, and shaped charge development.

The SWRI Engineering Dynamics Department is capable of measuring and predicting debris throw and dispersion. They perform scale model tests and validate results with developed software. They have experience in developing a software program called DISPRE for quantity-distance evaluation. They perform analyses of aircraft shelters and debris throw for accidental explosions, and predict fragment loads on structures.

The Engineering Dynamics Department also tests wide varieties of impact conditions including low and hypervelocity impacts. Their experience varies from space debris studies, to land mine protection. They are involved in fragment shields for containment structures, concepts of munitions storage, and donor/acceptor propagation testing.

Finally, the Ballistic and Explosion Test Facility has widespread instrumentation for measuring ballistic and explosive events. Their piezoelectric transducers measure blast and quasi-static pressures. Dynamic measurements include temperature, strain, acceleration, rotation, and displacement. They are equipped with high-speed imaging up to 10^8 frames per second, Hewlett Packard pulsed x-ray systems for radiography.



Figure 8: SWRI Tests

5.6.2.8. Texas Tech University Lubbock, TX:

Texas Tech currently has a blast testing facility located outside the campus of Lubbock, TX. It is operated under the guidance of Dr. H. Scott Norville, a professor in the department of Civil and Environmental Engineering University at Texas Tech University. This facility has been developed for the evaluation of glazing systems.

The facility is an open-air arena located on a 2-acre plot in a remote area outside of Lubbock. The test site is capable of detonating charges up to 140 kg (300 lb) of TNT. Currently, this site has not been utilized significantly for evaluating blast effects on structures [23].

5.7. Current Blast Experts

5.7.1. Dr. Theodor Krauthammer

Dr. Krauthammer is a Professor of Civil Engineering at the Pennsylvania State University. He is also Director of its Protective Technology Center. His research focuses on structural behavior under severe dynamic loads with consideration to survivability and fragility of structures exposed to blast, shock, and impact. Dr. Krauthammer has done extensive work on the modeling of blast loading of structures [24, 25]. Furthermore, he has contributed to the assessment of safety and physical security of buildings before or after violent crimes [3].

5.7.2. Maj. Jim MacKenzie

Major MacKenzie is a Royal Engineer based at the U.S. Army Waterways Experimental Station in Vicksburg, MS. He is routinely concerned with large-scale blast experiments and testing. The Big Black test facility located approximately 30 miles outside of Vicksburg is capable of large open-air detonations for structural testing [21].

5.7.3. Dr. Peter Smith

Dr. Smith works in the Engineering Systems Department at the Royal Military College of Science. He is involved in the testing of scaled structures at the explosive range facilities located at the Cranfield campus [22].

5.7.4. Dr. H. Scott Norville

Dr. Norville is a leading authority on the engineering properties of window glass. He has developed an expertise concerning behavior of window glass and other glazing materials subjected to blast loads (http://www.wind.ttu.edu/Faculty_Info/norville/norville2.htm).

Dr. Norville has conducted many experiments evaluating performance of glazing materials under blast loading [8, 26]. He has also made significant contributions to the development of an ASTM F1642 Standard Test Method for Glazing Systems Subject to Airblast Loadings [10]. Dr. Norville has co-authored two manuals on window glass design and one software package.

5.8. Current Testing Technologies

There have been a couple of unique advancements in the field of blast testing. Shock tubes have been developed and used in government and university facilities for years. These devices can apply an impulsive airblast pressure to a structure such as walls and slabs. This provides important data for the behavior of these structures in an explosive environment. Also, advancements in high strain rate material testing have been accomplished through use of the Split Hopkinson Bar. High strain rate testing is extremely important for understanding structural response to blasts since material properties differ under this type of loading.

5.8.1. Shock Tube

A shock tube is a device that can be used to study shock waves or investigate the effects of high pressure impulses on structures. Shock tubes are commonly used to test walls for quick, impulsive pressures.

The shock tube is a fairly simple mechanism. Figure 9 below shows a basic schematic of a shock tube. The tube itself is split into two parts, the driver section and driven section. The driven section is filled with a desired gas to a desired pressure. The driver side is slowly filled with an inert gas (helium, argon, or an argon/helium mixture) until the diaphragm ruptures due to the pressure difference. A shock wave propagates into the driven side while an expansion wave travels into the driver section. Both the expansion and shock waves reflect off the end of the tube and interact with each other until the pressure is equalized. This whole process takes approximately 1 millisecond [27].

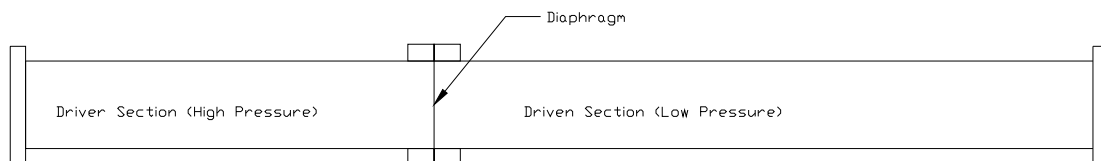


Figure 9: Basic Schematic of Shock Tube

A number of universities currently have shock tube testing facilities. They include California Institute of Technology, the University of Illinois at Urbana-Champaign, Stanford University, and the University of Wisconsin-Madison.

5.8.2. Split-Hopkinson Pressure Bar

The material properties of structures behave differently under blast loads. The Split Hopkinson bar is a device for performing high strain-rate experiments. It consists of three long pressure bars, namely the striker bar, incident bar, and transmission (output) bar. The test specimen is placed between the transmission and incident bar. Strain gages are mounted on the incident bar, transmission bar, and test specimen itself. A gas gun supplies the necessary energy

to propel the striker bar. This sends a compressive wave into the incident bar. Force and displacement can be derived from the measured strains assuming wave propagation in the bars is not dispersive (<http://matrix.ecn.purdue.edu/~cmlweb/resources/devices/hopkinson.htm>). See Figure 10 for a typical Split Hopkinson bar.

Bertram Hopkinson was the original inventor of the Hopkinson bar. He used the Hopkinson bar to study the shapes of pressure waves from the detonation of explosives or impact of bullets at one end of a long rod [28]. Kolsky modified the original Hopkinson Bar in 1949 by adding another bar with the specimen placed between the two ends [29, 30]. The bar then became known as the Kolsky Bar or Split Hopkinson Pressure Bar (SHPB). Kolsky incorporated work done by Davis [31] to obtain stress-strain behaviors in both bars. The stress-strain history of the specimen could then be obtained from the theory of one dimensional wave propagation theory.

To a good approximation, waves traveling in the bar are governed by the one dimensional wave equation [32]:

$$\partial^2 u^2 / \partial x^2 - 1/c^2 \partial^2 u^2 / \partial t^2 = 0$$

having the solution

$$u = f(x - ct) + g(x + ct) = u_i + u_r$$

where u_i is the incident wave and u_r is the reflected wave.

By definition the strain in the incident bar is

$$\varepsilon = \partial u / \partial x$$

The strain in the incident bar is therefore

$$\varepsilon = f' + g' = \varepsilon_i + \varepsilon_r$$

The velocity at any point in the incident bar is

$$\dot{u}_1 = c(-f' + g') = c(-\varepsilon_i + \varepsilon_r)$$

The velocity in the output (transmission) bar is

$$\dot{u}_2 = -c\varepsilon_t$$

The corresponding strain rate in the specimen is

$$\dot{\varepsilon} = (\dot{u}_1 - \dot{u}_2) / l_s = c/l_s (-\varepsilon_i + \varepsilon_r + \varepsilon_t)$$

where l_s is the instantaneous length of the specimen.

The forces in the incident and output bars are

$$F_1 = AE(\varepsilon_i + \varepsilon_r)$$

$$F_2 = AE\varepsilon_t$$

Setting the forces equal yields

$$\varepsilon_i = \varepsilon_i + \varepsilon_r$$

Therefore

$$\dot{\varepsilon} = 2c \varepsilon_r / l_s$$

The stress is calculated by dividing the force by the cross-sectional area of the specimen

$$\sigma(t) = AE\varepsilon_t / A_s$$



Figure 10: Split Hopkinson Bar

5.9. Concerns

5.9.1. Noise

The sound wave generated by a large explosion can be very hazardous to the surrounding environment. Even at a range of a few hundred meters, the decibel level can be on the order of 120-140 dB for a high explosive (HE) detonation [21]. This level of noise corresponds to a jet takeoff (at 200 feet standoff distance) and an air raid siren having corresponding levels of 120 dB and 140 dB (<http://www.deq.state.or.us>). Fifty percent of exposed eardrums rupture at a pressure of 15 psi for fast rising pressures [1].

5.9.2. Safety

Generating a blast environment puts the lives of those involved at stake. A significant amount of planning and care must be taken to ensure the safety of anyone in the vicinity of the blast testing facility and environment. The blast wave must be properly contained or an appropriate standoff distance must be enforced to negate hazardous effects from the potentially dangerous blast overpressure. Reflections of the blast and amplifications in blast overpressure need consideration. The fragments produced by the detonation, whether they are primary or secondary, must be contained so that no person suffers bodily harm.

5.9.3. Cost

The funds necessary for simulating a blast environment for structural testing are enormous. Careful planning and budgeting must be performed to ensure that all necessary equipment, labor costs, and safety measures are taken into account.

5.10. Discussion

There has been an increased threat to the security of buildings due to terrorist actions. These bombings have revealed the weaknesses of structures to resist various phenomenon. Effects such as brisance, progressive collapse, fragments, and reverse loading of slabs can deteriorate the integrity of structures to the point of global failure.

The results of brisance must be further studied to design against this occurrence. Furthermore, a progressive collapse study must be performed to evaluate a structure based on the loss of a structural element. An example of this is to remove a column from a structure, possibly lost by brisance, to predict the behavior of the remaining structural members.

A study of the high velocity fragments produced in a blast needs investigation. This can be accomplished by designing a catapult system to launch fragments at structural elements. The reaction of walls, columns, beams, and girders to this highly impulsive impact loading can be tested in this manner.

Slabs may experience a loading from underneath when a blast overpressure enters a structure through an opening such as a window bay. This causes the slab to bend in the opposite direction for which it was designed. It also may induce tensile forces in the adjacent columns. The failure of these slabs should be contained locally in their respective bays to prevent global failure.

The material behavior of structures under explosive loads differs from its expected live and dead loads. This is due to the extremely high strain rates involved in a blast environment. A Split Hopkinson Bar has been developed to determine the strain in a specimen under a high strain rate. Strain rates on the order of 1000 s^{-1} have been measured with this device.

The performance of structures under blast loads requires extensive investigation. Human lives depend on thorough studies of current techniques and improvements to blast resistant designs. The design of structures to resist terrorist threats and accidental explosions will continue to increase in demand and most certainly remain as one of the most important areas of structural engineering.

5.11. Acknowledgments

- Dr. Clay Naito
- PITA
- ATLSS

5.12. References

- [1] U.S. Department of the Army, "Structures to Resist the Effects of Accidental Explosions," Technical Manual 5-1300, Navy NAVFAC P-357, AFR 88-22. Washington, D.C.: Departments of the Army, Navy, and Air Force, 1969.
- [2] Michael Neff, "A Visual Model for Blast Waves and Fracture." Thesis submitted for degree M.S. of Computer Science, University of Toronto, 1998.
- [3] Conrath, E. J., Krauthammer, T., Marchand, K. A., Mlakar, P. F., "Structural Design for Physical Security – State of the Practice." Structural Engineering Institute of ASCE, Reston, VA, 1999.
- [4] U.S. Department of Energy, 1992. A Manual for the Prediction of Blast and Fragment Loadings on Structures. DOE/TIC-11268. Washington, D.C.: U.S. Department of Energy.
- [5] Frederick J. Bueche, "Introduction to Physics for Scientists and Engineers." McGraw-Hill Book Company, New York, fourth edition, 1986.
- [6] P.D. Smith and J. G. Hetherington. "Blast and Ballistic Loading of Structures." Butterworth and Heinemann Ltd., Oxford, 1994.
- [7] Henrych, J., "The Dynamics of Explosion and Its Use," Technical Research Institute of Prague, Building Research Institute, Elsevier Scientific Publishing Co., 1979.
- [8] Norville, H. S., Harvill, N., Conrath, E.J., Shariat, S., Mallonee, S., "Glass Related Injuries in Oklahoma City Bombing," *Journal of Performance of Constructed Facilities*, 13(2): 50-56, May, 1999.
- [9] *Misty picture data: window glass experiment, final data report.* (1987). Glass Research and Testing Lab., Texas Tech University, Lubbock, TX.
- [10] ASTM F1642-96, *Standard Test Method for Glazing and Glazing Systems Subject to Airblast Loading*, ASTM Standards, American Society for Testing Materials, Philadelphia, PA, 1996.
- [11] ASTM E1300-00, *Standard Practice for Determining Load Resistance of Glass in Buildings*, ASTM Standards, American Society for Testing Materials, Philadelphia, PA, 2000.
- [12] ASTM E997-01, *Standard Test Method for Structural Performance of Glass in Exterior Windows, Curtain Walls, and Doors Under the Influence of Uniform Static Loads by Destructive Methods*, ASTM Standards, American Society for Testing Materials, Philadelphia, PA, 2001.
- [13] Longinow, A., Mniszewski, K. R., "Protecting Buildings Against Vehicle Bomb Attacks," *Practice Periodical on Structural Design and Construction*, 1(1): 51-54, February, 1996.
- [14] Wilson, A.G., Tamura, G.T., "Stack Effect in Buildings." <http://www.nrc.ca/irc/cbd/cbd104e.html> (August 1968).
- [15] Wright, C., "Convective Flow due to Stack Effect." http://www.chuck-wright.com/calculators/stack_effect.html.

- [16] Gilbert, F. K., *Explosive Shocks in Air*. The MacMillan Company, New York, 1962.
- [17] McVay, M. K. (1988). "Spall Damage of Concrete Structures." *U.S. Army Engr. Waterway Experiment Station Technical Rep. SL-88-22*. U.S. Army Engineer Waterways Experiment Station, Vicksburg, MS.
- [18] Mlakar, P. F., Corley, W. G., Sozen, M. A., Thornton, C. H., "The Oklahoma City Bombing: Analysis of Blast Damage to the Murrah Building," *Journal of Performance of Constructed Facilities*, 12(3): 113-119, August, 1998.
- [19] Hinman, E., Dal Pino, J., Pekelnicky, R., "How Much Blast Protection Do Seismic Provisions Provide?" *Proceedings of the Seventh U.S. National Conference on Earthquake Engineering*, Boston, MA, July 21-25, 2002.
- [20] Ettouney, M., Smilowitz, R., Rittenhouse, T., "Blast Resistant Design of Commercial Buildings," *Practice Periodical on Structural Design and Construction*, 1(1): 31-39, February, 1996.
- [21] MacKenzie, Maj. J., U.S. Waterways Experimental Station, Vicksburg, MS, *Personal Communication*, June, 2002.
- [22] Smith, P., Royal Military College of Science, Cranfield, UK, *Personal Communication*, June, 2002.
- [23] Norville, H. S., Professor of Civil Engineering and Director of Glass Research and Testing Laboratory, Texas Tech University, Lubbock, TX, *Personal Communication*, June, 2002.
- [24] Krauthammer, T., Ku, C.K., "A Hybrid Computational Approach for the Analysis of Blast Resistant Connections", *Computers and Structures*, Vol. 61, No. 5, 1996, pp. 831-843.
- [25] Krauthammer, T., Otani, R.K., "Mesh, Gravity and Load Effects on Finite Element Simulations of Blast Loaded Reinforced Concrete Structures", *Computers and Structures*, Vol. 63, No. 6, 1997, pp. 1113-1120.
- [26] Norville, H.S., King, K. W., Swofford, J. L., "Behavior and Strength of Laminated Glass," *Journal of Engineering Mechanics*, 124(1): 46-53, January, 1998.
- [27] Rasheed, A., "How a Shock Tube Works." <http://www.galcit.caltech.edu/~arasheed/st17/st.html> (July 26, 1998).
- [28] Hopkinson, B. (1914), "A Method of Measuring the Pressure Produced in the Detonation of High Explosives or by the Impact of Bullets." *Philosophical Transactions of the Royal Society of London A*, Vol. 213, pp. 437-556.
- [29] Kolsky, H. (1949), "An Investigation of the Mechanical Properties of Materials at Very High Rates of Loading." *Proceedings of the Physics Society of London B*, Vol. 62, pp. 676-700.
- [30] Kolsky, H. (1963), *Stress Waves in Solids*, Dover Publications Inc., New York.
- [31] Davis, R. M. (1948), "A Critical Study of the Hopkinson Pressure Bar." *Philosophical Transactions of the Royal Society of London A*, Vol. 240, pp. 375-457.
- [32] Gray, G. T., "High Strain-Rate Testing of Materials: The Split Hopkinson Bar." *Methods in Materials Research*, John Wiley Press, October, 1997.
- [33] Task Committee on Blast Resistant Design, "Design of Blast Resistant Buildings in Petrochemical Facilities," Petrochemical Committee of the Energy Division of ASCE, New York, NY, 1997.

5.13. Appendix A: Column Calculations

The following examples give a detailed procedure [1] for calculating the blast loads on a column given the explosive weight W in lbs, distance from detonation to structure R in feet, and the height and width of the structure in feet

Alfred P. Murrah Building
Column G12 East Face

Given Parameters:

$W = 4000$ lbs
 North distance = 14 ft
 Lateral distance = 87 ft
 $R = 88.1$ ft
 Height = 21 ft
 Width = 36 in

Note: All referenced figures are from the Army Technical Manual TM5-1300 [1].

Find free field blast wave parameters:

Calculate scaled ground distance:

$$Z_g = 5.551 (W/lb)^{1/3}$$

Use Figure 2-15 to obtain the following values:

$P_{so} = 36$ psi
 $t_b/W^{1/3} = 1.650$ ms/lb^{1/3}
 $L_w/W^{1/3} = 1.500$ ft/lb^{1/3}
 $t_r/W^{1/3} = 1.650$ ms/lb^{1/3}
 $i_r/W^{1/3} = 15.000$ psi*ms/lb^{1/3}

$t_a = 26.19$ ms
 $L_w = 23.81$ ft
 $t_b = 26.19$ ms
 $i_b = 238.11$ psi*ms

Determine front wall reflected pressure and impulse:

Input the angle of incidence:

$a = 9.1$ degrees

Read C_{ra} for P_{so} and a from Figure 2-193:

$C_{ra} = 3.50$

Calculate P_{ra} from $C_{ra} = P_{ra}/P_{so}$:

$P_{ra} = 126$ psi

Read $i_{ra}/W^{1/3}$ for P_{ra} , and a from Figure 2-194:

$i_{ra}/W^{1/3} = 28$ psi*ms/lb^{1/3} $i_{ra} = 444$ psi*ms

Determine front wall loading, positive phase:

Read sound velocity in reflected overpressure region C_r from Figure 2-192:

$C_r = 1.62$ ft/ms

TM5-1300 Method for calculating t_c

Calculate clearing time t_c from Equation 2-8, $t_c = 4^*S/[(1+R)*C_r]$:

$S = 1.500$ ft

$H = 21$ ft

$G = 21.000$ ft

$R = 0.071$

$t_c = 3.457$ ms

OUT OF RANGE!!

Equation 3-8 below [33] was used if C_r was off the graph of Figure 2-192

Used!!!!

Petrochemical/ Newmark Method for calculating t_c

Calculate clearing time t_c from Equation 3-8, $t_c = 3^*S/U < t_c$, where $S = \min(\text{Height}, \text{Width}/2)$,

$U = 1130 \times (1 + 0.058P_{so})^{0.5}$:

$S = 1.500$ ft

$P_{so} = 36$ psi

$U = 1985.716$ ft/sec

$t_c = 2.266$ ms

Calculate the fictitious positive duration t_{df} from Equation 2-11, $t_{df} = 2^*t_r/P_{so}$:

$t_{df} = 13.23$ ms

Determine the peak dynamic pressure q_0 from Figure 2-3:

$q_0 = 22$ psi

Input C_D from Section 2-15.3.2:

$C_D = 1.0$ For Front

Calculate $P_{so} + C_D q_0$:

$P_{so} + C_D q_0 = 58$ psi

Calculate fictitious reflected pressure duration t_{rf} :

$t_{rf} = 7.06$ ms

Construct the positive pressure-time curve:

Determine front wall loading, negative phase:

Read values of Z corresponding to P_{ra} and $i_{ra}/W^{1/3}$ from Figure 2-15:

$Z(P_{ra}) = 5.50$ ft/lb^{1/3}

$Z(i_{ra}/W^{1/3}) = 6.00$ ft/lb^{1/3}

Using Z values from above and Figure 2-16, determine values of P_{ra}^- and i_{ra}^- :

$P_{ra}^- = 4.3$ psi

$i_{ra}^-/W^{1/3} = 21$ psi*ms/lb^{1/3}

Calculate fictitious duration t_{rf}^- :

$t_{rf}^- = 155.05$ ms

Calculate negative phase rise time:

$0.27^* t_{rf}^- = 41.86$ ms

Construct the negative pressure-time curve:

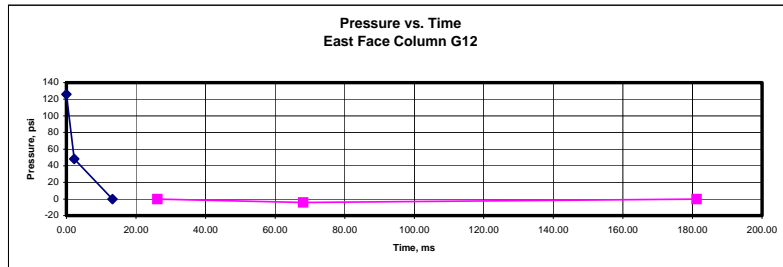
$t_0 = 26.19$ ms

$t_1 + 0.27^* t_{rf}^- = 68.06$ ms

$t_1 + t_{rf}^- = 181.24$ ms

Curve Parameters	Time [ms]	Pressure [PSI]
Positive phase:	0.00	126
	2.27	48
	13.23	0
Negative phase:	26.19	0
	68.06	-4
	181.24	0

P_r Peak reflected Pressure
 Intercept of t_c with Pressure load ($P_{so} + C_D q_0 - t_{of}$ line)
 $-P_{ra}$ Negative Peak reflected pressure



The following examples give a detailed procedure [1] for calculating the blast loads on a column given the explosive weight W in lbs, distance from detonation to structure R in feet, and the height and width of the structure in feet

Alfred P. Murrah Building
Column G16 East Face

Given Parameters:

W = 4000 lbs
North distance = 14 ft
Lateral distance = 47 ft
R = 49.0 ft
Height = 21 ft
Width = 36 in

Note: All referenced figures are from the Army Technical Manual TM5-1300 [1].

Find free field blast wave parameters:

Calculate scaled ground distance:

$Z_0 = 3.089 \text{ ft/lb}^{1/3}$

Use Figure 2-15 to obtain the following values:

$P_{so} = 140 \text{ psi}$
 $t_{so}/W^{1/3} = 0.500 \text{ ms/lb}^{1/3}$
 $L_w/W^{1/3} = 0.790 \text{ ft/lb}^{1/3}$
 $t_r/W^{1/3} = 1.800 \text{ ms/lb}^{1/3}$
 $i_r/W^{1/3} = 25.000 \text{ psi}^* \text{ms/lb}^{1/3}$

$t_A = 7.94 \text{ ms}$
 $L_w = 12.54 \text{ ft}$
 $t_0 = 28.57 \text{ ms}$
 $i_s = 396.85 \text{ psi}^* \text{ms}$

Determine front wall reflected pressure and impulse:

Input the angle of incidence:

$a = 16.6 \text{ degrees}$

Read C_{ra} for P_{so} and a from Figure 2-193:

$C_{ra} = 5.10$

Calculate P_{ra} from $C_{ra} = P_{ra}/P_{so}$:

$P_{ra} = 714 \text{ psi}$

Read $i_{ra}/W^{1/3}$ for P_{ra} , and a from Figure 2-194:

$i_{ra}/W^{1/3} = 58 \text{ psi}^* \text{ms/lb}^{1/3}$
 $i_{ra} = 921 \text{ psi}^* \text{ms}$

Determine front wall loading, positive phase:

Read sound velocity in reflected overpressure region C, from Figure 2-192:

$C_r = 1.65 \text{ ft/ms}$

TM5-1300 Method for calculating t_c

Calculate clearing time t_c from Equation 2-8, $t_c = 4^*S/[(1+R)^*C_r]$:

$S = 1.500 \text{ ft}$

$H = 21 \text{ ft}$

$G = 21.000 \text{ ft}$

$R = 0.071$

$t_c = 3.394 \text{ ms}$

OUT OF RANGE!!!

Equation 3-8 below [33] was used if C_r was off the graph of Figure 2-192

USED!!!

Petrochemical/ Newmark Method for calculating t_c

Calculate clearing time t_c from Equation 3-8, $t_c = 3^*S/U$ & $t_c < t_0$, where $S = \min(\text{Height}, \text{Width}/2)$,

$U = 1130 \times (1 + 0.058 P_{so})^{0.5}$

$S = 1.500 \text{ ft}$

$P_{so} = 140 \text{ psi}$

$U = 3412.525 \text{ ft/sec}$

$t_c = 1.319 \text{ ms}$

Calculate the fictitious positive duration t_{pf} from Equation 2-11, $t_{pf} = 2^*i_r/P_{so}$:

$t_{pf} = 5.67 \text{ ms}$

Determine the peak dynamic pressure q_0 from Figure 2-3:

$q_0 = 190 \text{ psi}$

Input C_D from Section 2-15.3.2:

$C_D = 1.0$ For Front

Calculate $P_{so} + C_D q_0$:

$P_{so} + C_D q_0 = 330 \text{ psi}$

Calculate fictitious reflected pressure duration t_{rf} :

$t_{rf} = 2.58 \text{ ms}$

Construct the positive pressure-time curve:

Determine front wall loading, negative phase:

Read values of Z corresponding to P_{ra} and $i_{ra}/W^{1/3}$ from Figure 2-15:

$Z(P_{ra}) = 3.00 \text{ ft/lb}^{1/3}$

$Z(i_{ra}/W^{1/3}) = 4.00 \text{ ft/lb}^{1/3}$

Using Z values from above and Figure 2-16, determine values of P_{ra}^- and i_{ra}^- :

$P_{ra}^- = 11 \text{ psi}$

$i_{ra}^-/W^{1/3} = 35 \text{ psi}^* \text{ms/lb}^{1/3}$
 $i_{ra}^- = 556 \text{ psi}^* \text{ms}$

Calculate fictitious duration t_{rf}^- :

$t_{rf}^- = 101.02 \text{ ms}$

Calculate negative phase rise time:

$0.27^* t_{rf}^- = 27.27 \text{ ms}$

Construct the negative pressure-time curve:

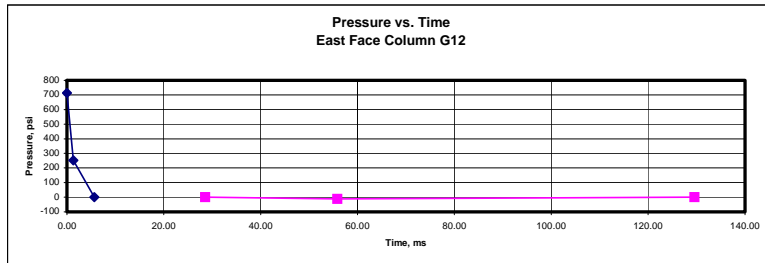
$t_0 = 28.57 \text{ ms}$

$t_n + 0.27 t_{rf}^- = 55.85 \text{ ms}$

$t_n + t_{rf}^- = 129.59 \text{ ms}$

Curve Parameters	Time [ms]	Pressure [psi]
Positive phase:	0.00	714 Pr
	1.32	253
	5.67	0
Negative phase:	28.57	0
	55.85	-11 -Pra
	129.59	0

Peak reflected Pressure
Intercept of t_c with Pressure load ($P_{so} + C_D q_0$ - t_{pf} line)
Negative Peak reflected pressure



Section 6: Mortar Reinforced With Superelastic Nickel-Titanium Fibers By Michael J. Minicozzi

Advisors: Yunfeng Zhang, Ph.D., David Brown, MSCE

6.1. PROJECT SUMMARY

Concrete is extremely desirable for construction applications because it is cheap, durable, and has acceptable compressive strength. However, it has unacceptable properties. Over the past 40 years, it has been proven that fiber reinforcement improves the poor characteristics of concrete [1]. This project's main focus is the material characterization of mortar reinforced with short discontinuous nickel-titanium (NiTi) superelastic fibers that provide better ductility, toughness, and strain recoverability to the composite than other fibers.

The primary objectives of this research project are to do an experimental study of the mechanical properties of mortar reinforced with short NiTi superelastic fibers and to examine the damage monitoring capability of NiTi fiber reinforced mortar with an electrical resistance technique.

Some of the main arrangements made for this research project include mold preparation, the mortar mixing and curing procedures, and the specimen test procedures. The two main tests in this experimental study are the compression test of cylindrical specimens and the flexural test (4-point bending) of beam specimens. The electrical resistance technique will monitor the damage to the flexural beam during loading.

No information in this area has been reported and research must be done on the behavior of this new type of fiber reinforcement. Potential applications for this research project include nuclear waste containment and blast-resistant military structures.

6.2. BACKGROUND

6.2.1. Fiber Reinforced Concrete

Concrete without reinforcement has many deficiencies that make it insufficient for many applications. These deficiencies include brittleness, poor tensile strength, and poor impact resistance. Brittleness leads to abrupt failures. Figure 1 shows a brittle fracture of plain mortar. Concrete tensile strength is generally only one tenth of its compressive strength. Low energy absorption capacity and low toughness cause the concrete to behave poorly under impact loading [1,2,3].

Improvements to counteract these faults were introduced in the mid 1800's. At this time steel reinforcement was first used, and it is still extremely popular for many applications. In the 1940's fiber reinforcing was introduced. The main idea behind fiber reinforced concrete (FRC) is the use of embedded fibers to enhance the energy absorption capacity and toughness of the concrete. Increases in tensile and flexural strength are also significant. Generally, the "first crack strength" of FRC is as much as three times higher than plain concrete and the ultimate strength can be raised five times by adding fiber reinforcement. In addition, FRC has significantly improved the ductility of plain concrete [3].



Figure 1: Brittle Fracture of Plain Mortar

Fiber reinforced concrete is a two-phase composite system. This composite system will act like an un-reinforced system until the “first crack strength” is reached. After this stress is reached the reinforcing fibers bridge across the cracks and allow for increasing stresses and deformations. The maximum load carrying capacity for fiber reinforcing is generally controlled by fiber pull-out. The fibers pull-out of the matrix before the yielding of the fibers occurs. This limits the amount of stress the fibers can transfer over a crack. With sufficient bond between fiber and matrix the strength and toughness behavior of FRC can be greatly improved [1,3].

There are four main topics that influence the properties of FRC. They are volume percent of fibers within the concrete matrix, aspect ratio, orientation of the fibers within the matrix, and type of fibers.

The fiber percentage within the concrete mix is based on volume and is conveyed as a percent of the mix. Common percentages are between 1.7 percent and 2.7 percent for testing purposes. Generally, the volume percentage of fibers within the hardened mix is directly proportional to the tensile strength of the composite.

The aspect ratio is the length of the fibers divided by the diameter of the fibers. This ratio signifies the amount of surface area of fiber against the concrete mix. The higher the ratio, the tougher the concrete mix will be. However, the length of the fibers cannot be too long because this will present problems in the workability of the mix and even fiber distribution.

The orientation of the fibers can either be continuous or discontinuous. Continuous fibers are aligned within the concrete matrix. This orientation of fibers within the concrete is strongest in the direction of the fibers and the weakest in the direction perpendicular to the fibers. Discontinuous fibers are randomly dispersed throughout the concrete matrix resulting in isotropic properties of the composite.

The most common types of fibers are steel, glass, and plastic fibers. The type of fibers used for any particular application is based on the desired effect the fibers have on the concrete properties, the type of structural member in the application, the atmospheric conditions, and the cost of the fibers [2,3].

6.2.2. Shape Memory Alloys/Superelasticity

Shape memory alloys are materials that when stressed and deformed can restore their original shape with a heating procedure that induces a phase transformation. In order to understand superelastic and shape memory NiTi alloys one must understand the two different crystal structures that are associated with them. The first is called the martensite phase. This crystal structure exists within the alloy at low temperatures. It is extremely weak and can be deformed by a relatively small-applied force. The second crystal structure is called the austenite phase. Generally, this phase exists at high temperatures within the alloy and has higher resistance to deformation. These two crystal structures allow for the shape memory and superelastic phenomena [4,5]. Stress-strain curves for each of these crystal structures can be seen in Figure 2.

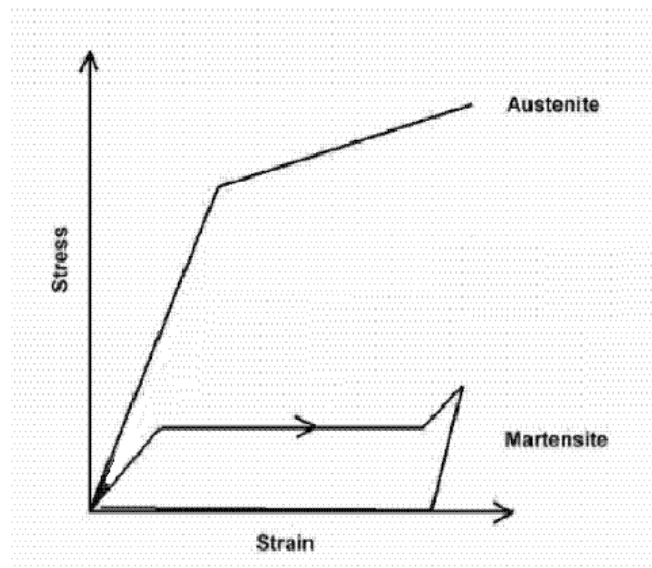


Figure 2: Typical stress-strain curves for martensite and austenite crystal structure of NiTi alloys [6].

Superelasticity is a property of shape memory alloys. It is a mechanical type of shape memory. This means that the material reverts back to its original shape after a cycle of loading. The superelastic effect is explained in Figure 3. This figure shows three stress-temperature graphs that trace a stress path of a typical superelastic material. The NiTi material starts in the austenite crystal structure (a) at a temperature that is slightly above the final temperature at which the material will transform from martensite to austenite (A_f – Austenite finish line). As the stressing proceeds (b), the crystal structure will eventually convert to martensite as it crosses the martensite start line (M_s) and goes past the martensite finish line (M_f). The material will then experience a substantial amount of deformation for small applied loads. As the material is released from stressing (c), the crystal structure of the material will pass the austenite start line and begin to revert back to the austenite phase. Upon crossing A_f the material will go back to its original shape [4,5]. Figure 4 shows a typical stress-strain curve for superelastic materials. One can see the loading and unloading scheme that occurs and how much strain results from the corresponding stresses at certain areas of the curve [6].

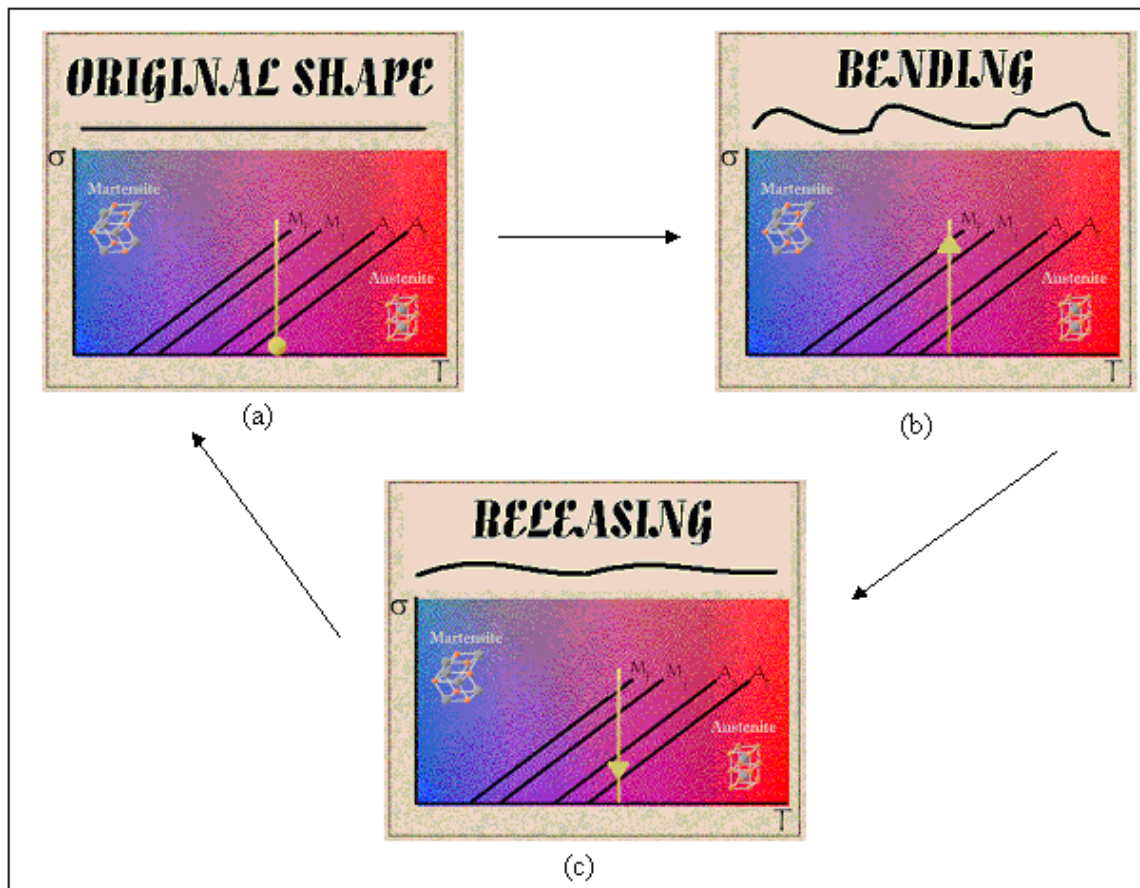


Figure 3: Three stress-temperature graphs that trace a stress path of a typical superelastic material [4].

Figure 5 shows a stress and temperature path of a typical shape memory alloy. These six graphs are the same graphs that are in Figure 3. In Figure 5, shape memory materials begin the cycle by cooling from the austenite phase to the martensite phase. When in the martensite phase, the material can be loaded and unloaded resulting in deformation. After this deformation, the material is heated and the crystal structure reverts back to the austenite phase. This results in the return of the material's original shape. This occurs because the austenite phase has only one possible orientation that accommodates its crystal structure [4,5].

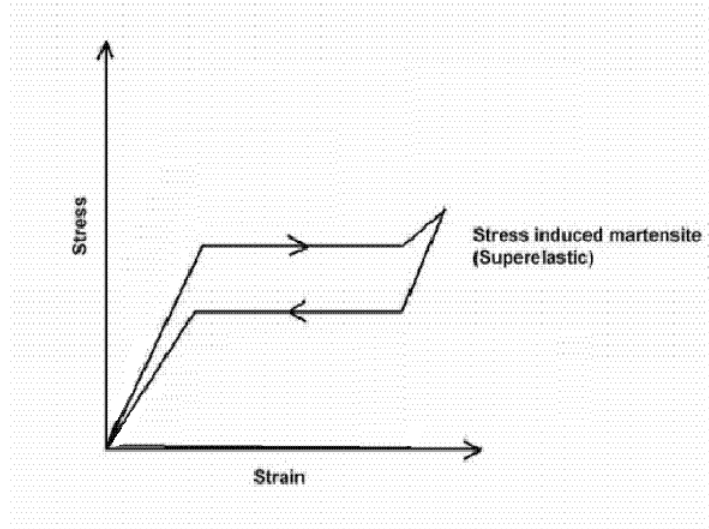


Figure 4: A typical stress-strain curve for superelastic materials [6]

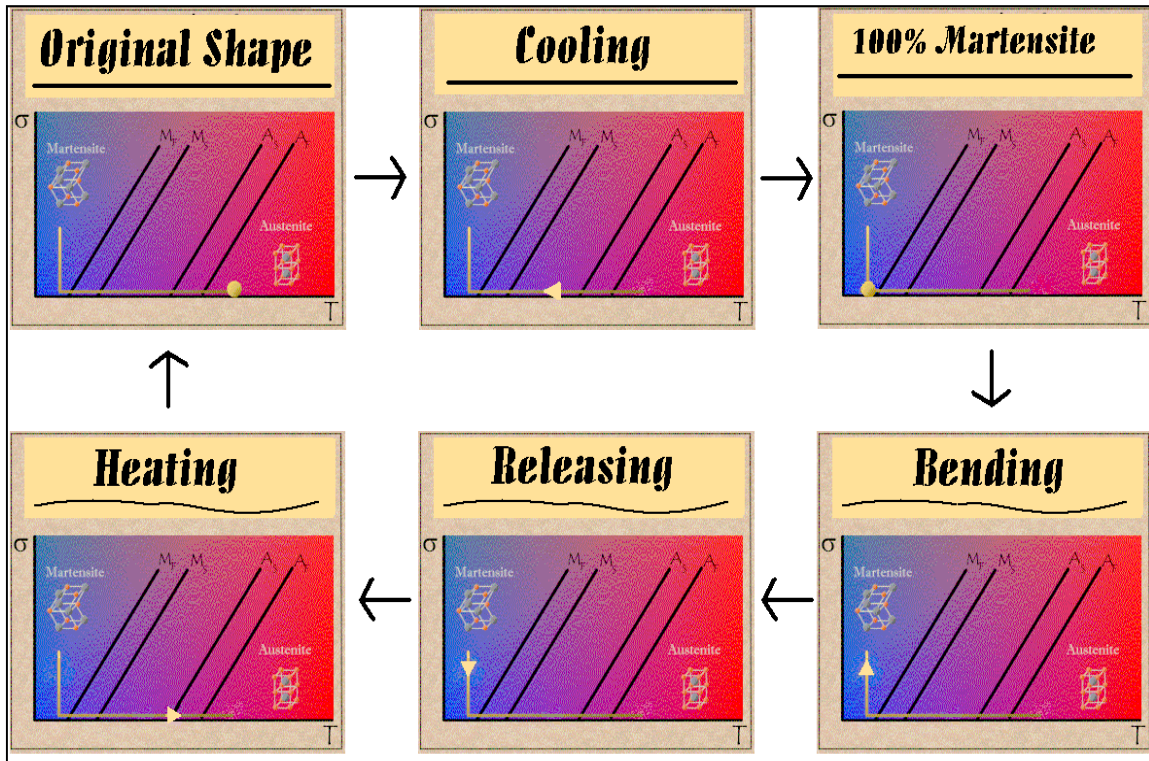


Figure 5: Stress and temperature path of a typical shape memory alloy [4].

6.2.3. Shape memory and superelastic alloy applications

Shape memory and superelastic NiTi alloys have many applications. They can range from medical devices, to industrial goods, to consumer goods.

NiTi alloys are extremely compatible with the human body, which make them popular materials for medical application. Another important point is shown in Figure 6. This is a stress-strain curve for a NiTi alloy and a typical stainless steel. Nickel-titanium alloys are so common to medical applications because of the unloading plateau that results. This plateau is the basis for certain medical devices. In dentistry, the constant force that occurs over a large strain range with a nickel-titanium device will increase tooth movement with less pain to the patient. In addition, the elasticity of stainless steel (most common medical device material used at the present time) is about 0.5 percent

while the elasticity of NiTi is 11 percent making the elasticity of NiTi alloys twenty times greater than stainless steel.

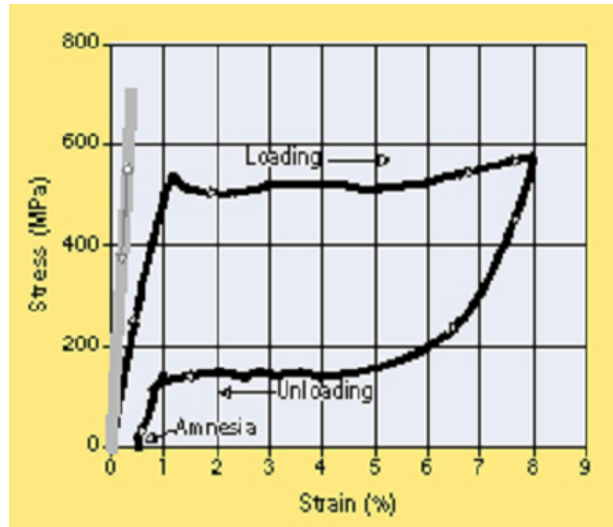


Figure 6: Stress-strain curve for a NiTi alloy and a typical stainless steel [7].

Shape memory and superelastic alloys go beyond just medical applications. For instance, these alloys can be used for hydraulic pipe couplings. This pipe fitting application uses its shape memory capability. The pipe coupling is first brought down to cryogenic temperatures where the martensite crystal structure will be present. The coupling is then expanded and slid on the pipes. Then it is heated up and tries to revert back to the original shape (austenite crystal structure present) before the cooling and deformation occurred. The pipe coupling is then constrained by the pipes creating a connection more efficient than a weld.

Consumer goods can also take advantage of shape memory alloy characteristics. For instance, superelastic frames of glasses that endure large amounts of deformation. If bent, the frames to these sunglasses will return to their original position [5].

6.3. PROJECT OVERVIEW

This research project has four distinct parts: mold preparation, mortar mixing, mortar curing, and compression and flexural testing. Mold preparation consists of cutting and grinding steel angles and bases to construct beam molds. From these beam molds and cylindrical plastic molds there will be a total of four batches of castings (cylindrical and beam specimens) made and cured. These specimens will then be tested after a 28-day period.

6.3.1. RESEARCH AND EXPERIMENTAL STUDIES

6.3.1.1. Mortar-NiTi Fiber System

Nickel-titanium fibers within a Portland cement based matrix have many advantages. The first and most important is that these types of fibers have greater ductility and strain recovery than other fibers. NiTi fibers have a recoverable strain up to ten percent [5]. Additionally, the use of NiTi fibers will stop the initiation and arrest the propagation of cracks that will arise as the mortar is stressed. The discontinuity of the fibers within the mortar matrix give the mortar isotropic properties to “bridge” cracks in any direction. Moreover, some other key virtues that NiTi fibers contribute to the reinforcement of the mortar are their high fatigue life, high corrosion resistance, and their high energy-absorption capacity [8].

On the other hand, there are some unfavorable issues associated with NiTi alloys. The manufacturing cost of NiTi alloys is high. One reason for this is the extremely reactive nature of titanium. The melting of titanium must be done in an inert atmosphere. In addition, the machining of the alloys can be difficult. When the superelastic material is cold worked it will work harden quickly. Fortunately, NiTi alloys do have a fine grain structure that can be successfully drawn into fine wire. The complexity of the fabrication creates another problem in that the possible shapes that can be formed from this material are limited. For many uses the needed shapes must be custom-manufactured [5].

The two main potential applications for mortar reinforced with superelastic fibers are nuclear waste containment and blast-resistant military structures. All the merits of superelastic fiber reinforced mortar will contribute to these applications, but the expensive fabrication process hinders a large structural function. For critical structures, the relatively high cost may not be a problem because of the importance of their function. Also, as the material is used more exclusively the material's cost may come down [8].

6.3.1.2. Specimens

In this research study there will be two types of specimen: cylindrical, and beam. The cylindrical samples will be 4 inches in length by 2 inches in diameter and the beam samples will be 8 inches in length, 2 inches in width, and 2 inches in height.

Four castings of mortar will be made. The first casting is a test batch of plain mortar to test the mortar mix proportions. In addition, the test batch samples will be used to perfect the test procedures used on the future specimens. This test batch will contain 24 beam specimens and 12 cylindrical specimens.

The last three castings will be used for the experimental study. The second casting will be a batch of plain mortar. The third will be a batch of mortar reinforced with carbon fibers. Finally, the fourth will be a batch of mortar reinforced with NiTi fibers. These castings will consist of 24 beam specimens and 6 cylindrical specimens. Each batch will be cured for a 28-day period and then tested.

6.3.1.3. Specimen Preparations

The cylindrical molds are plastic and are the same dimensions as the cylindrical specimens that will be tested. The beam molds are made of steel. They consist of four steel angles that sit on a steel base plate. The steel angles and base plate were cut as follows. Two of the steel angles 2 X 2 X 2 inches and the other two are 28 inches in length by 2 inches in width and 2 inches in height. The steel base plates are 28 inches in length by 6 inches in width. The two longer steel angles sit on the ends of the length side of the base plate with their angles toward the middle. The two smaller steel angles sit on the center of the ends of the width side of the base plate with their angles toward middle. This gives a mold that produces a mortar beam that is 24 inches in length by 2 inches in width by 2 inches in height. After the casting and curing process, these beams are cut into three specimens that are 8 inches in length.

The mortar mixing and curing procedure are ASTM C192 Standard. This standard sets the guidelines for an appropriate casting and curing process procedure of the mortar test specimens. The proper molds, tools (concrete mixer, external vibrator, etc), mixing procedure, mixing environment, and curing environment are presented accordingly. Additionally, a slump test and temperature measurement within this procedure follows the ASTM C143 Standard and ASTM C1064 Standard respectively.

The compression test of the cylindrical samples follows the ASTM C39 Standard. This standard sets the guidelines for the appropriate testing procedure for testing the maximum compressive strength of the mortar specimen. The standard has requirements for the bearing blocks and specimen that may be used. It also gives the calculation technique for the maximum compressive strength of the mortar specimens.

For the flexural test and toughness measurement procedure of the beam specimens the ASTM C78 standard is used in conjunction with ASTM C1018. ASTM C78 Standard is the test method for the flexural strength of the mortar. This standard sets the guidelines for the proper apparatus that must be used. It shows the appropriate procedure and calculation technique to determine the modulus of rupture. ASTM C1018 Standard is the test method to ascertain the flexural toughness and first-crack strength of the mortar with and without fiber reinforcement. It provides the correct technique and formulas for each calculation. Appendix A includes summaries of all of these procedures.

6.3.1.4. Test Results

The results of the compression test of each cylinder will give a load history. This load history will show a maximum peak load that will be converted into a maximum compressive strength by dividing by the cross sectional area of the cylinder sample.

The results of the flexural test on the beam specimens will be used to calculate the modulus of rupture and toughness of the material. The modulus of rupture (R) can be determined from the maximum load (P) of the flexural test, the span length (L), the average width (b) of the specimen at fracture, and the average depth (d) of the specimen at fracture. The formula for R is:

$$R = PL/bd^2$$

The toughness (energy absorption capacity) of the material is represented as the area under the load-deflection curve. First, one must determine the first crack strength and corresponding first crack deflection (δ). Secondly, one must calculate toughness indexes I_5 , I_{10} , and I_{20} at deflections 3, 5.5, 10.5 times the first crack deflection respectively. The toughness indexes equations are:

$$I_5 = \text{area under the load deflection curve up to } 3\delta / \text{area under the load-deflection up to } \delta$$

$$I_{10} = \text{area under the load deflection curve up to } 5.5\delta / \text{area under the load-deflection up to } \delta$$

$$I_{20} = \text{area under the load deflection curve up to } 10.5\delta / \text{area under the load-deflection up to } \delta$$

All techniques and formulas are according to ASTM standards.

While the flexural test on the beam specimens is in progress, the electrical resistance technique will be used to detect the damage that is occurring in the mortar. This technique is based on the hypothesis that the volume electrical resistivity depends on the propagation of cracks in concrete that is being stressed [8]. A four-ring electrode configuration will be used as shown in Figure 7. The silver paint will be put on the beam first, followed by the copper wire directly over it. The paint will be placed a half an inch from the contact point of each lower support to the mortar. A function generator will create a current across the outer rings of the specimen while a voltage will be measured through the inner rings. All measurements and data storage will be done on multimeters. Ohm's law will be used to calculate the resistance ($R = V/I$) and the electrical resistivity (ρ) can be calculated using $\rho = R \cdot A/L$. A is the cross-sectional area of the beam and L is the height of the specimen [9].

Additionally, the applied load and the deflection in the direction of the applied load will be measured. The contact points between the lower and upper supports and the mortar beam are 3 inches and 1 inch from the midpoint respectively. LVDT's will measure this deflection on both sides of the specimen. They will be on a yoke setup on the beam specimen and data from both will be averaged [9].

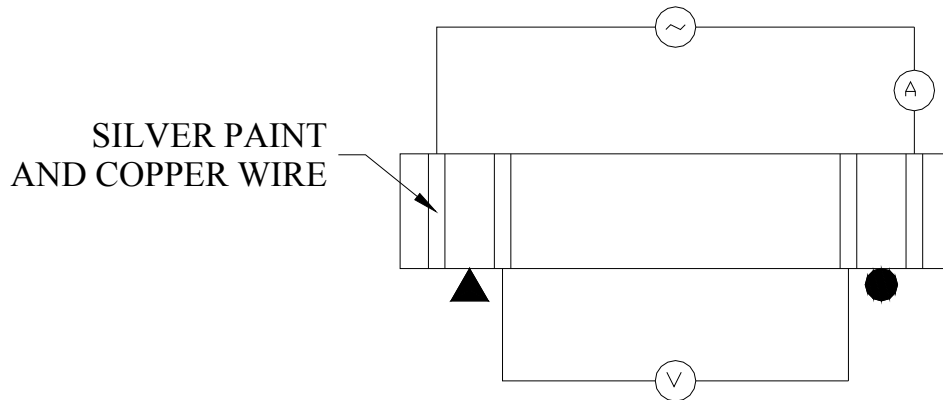


Figure 7: Four-ring electrode configuration on beam specimen [9]

6.4. CONCLUSION

Considerable research has been done on the material characterization of many types of fibers within FRC, but none has been performed on concrete reinforced with short discontinuous superelastic fibers. These fibers are expected to increase the composite's ductility, toughness, and strain recoverability more than other fibers. In order to investigate these properties compression and flexural tests will be performed. This research also examines a damage monitoring technique that can be performed using electrical equipment. This study will hopefully present a new material that can be used for nuclear waste containment and blast-resistant military structures.

6.5. ACKNOWLEDGEMENTS

I would like to thank the following people for their assistance:

Dr. Yunfeng Zhang

Mr. David Brown

Dr. Clay Naito

Dr. Eric Kaufman

John Hoffner

Gene Matlock

Joe Timar

My fellow REU friends

6.6. APPENDIX A

6.6.1. Summary: ASTM C192 - Standard Practice for Making and Curing

Concrete Test Specimens in the Laboratory

Materials: Mortar, Admixtures, and Burlap

Equipments: Revolving Pan, External Vibrator, Cylindrical and Beam Molds, Scale, Trowel, Slump mold, Tamping Rod, Temperature measuring device, Reference Temperature measuring device

1. Mixing operations will be performed in Fritz Concrete Laboratory.
2. Make sure the water tightness of the mold is acceptable. Use of heavy grease, or thin rubber pieces in the joints.
3. Check molds for smooth walls and no indentations. The beam mold's maximum variation from the nominal cross section should not exceed 1/16". The mold's nominal length variation should not be shorter than 1/16", but it may exceed that.
4. Before mixing the mortar, the mortar materials should be brought to a temperature range of 68 to 86°F. Store mortar according to manufacture's specifications. Mix mortar and admixtures (methylocellulose, superplasticizer) according to manufacturing specifications. The apparatus for mixing should be cleaned after each batch is made to ensure that the subsequent batch is not contaminated by the chemical additions or admixtures used in the mortar. Cover the mortar when it is not being remixed or sampled.
5. Mixing Procedure
 - a) Fill a mixing container with 4/5 gallon of water.
 - b) Add Sika MonoTop while continuing to mix.
 - c) Fill the mixing container with an additional 1/4 gallon of water.
 - d) Mix fibers accordingly
 - e) Use a low-speed drill (400-600 rpm) and paddle or mortar mixer to mix mechanically. Mix uniformly for a maximum of three minutes.
6. After mortar is mixed, a slump test will be performed (Summary: ASTM C143 – Standard Test Method for Slump of Hydraulic Cement Concrete)
 - a) Fill the mold in three layers. Each layer being one-third the mold
 - b) Stroke each layer 25 times with the tamping rod
 - c) Distribute the strokes uniformly over the cross section
 - d) For the top layer, fill mortar above the top of the mold before rodding. Rod the layer as mentioned above. If the mortar is below the top of the mold add more to keep excess on the top surface.
 - e) After rodding this top layer, strike off top surface by screeding and rolling motion of the tamping rod.
 - f) Steadily lift the mold in a vertical direction 12" in 5 +/- 2 seconds
 - g) The entire test should take be in the time span of 2.5 minutes.
 - h) Measure slump. Measure the vertical distance between the top of the mold and displaced original center of the top surface to the nearest 1/4". Use the equation below to compute the slump

$$\text{Slump} = 12 - \text{inches of height after subsidence}$$

*The slump test is unacceptable if the mortar does not slump more than 1/4".

7. 36 castings will be in the first batch and 30 castings in the last three. The beam specimens will be cast first and the cylindrical specimens will be cast thereafter. Place the mortar in the molds using a trowel. Each trowelful should be representative of the whole entire batch. Prevention of segregation during molding is important. Make sure the mortar within the mold is symmetrically distributed by moving the trowel around the top edge of the mold as the mortar is discharged. A tamping rod can also be used to help distribution and prevent segregation. Fill the molds with the least number of lifts possible.
8. To completely fill the molds apply external vibration for 20-30 seconds. Vibration is usually ceased when the surface of the concrete is smooth. Vibrate for only a certain period of time that will help consolidation, but not let segregation occur. Keep the external vibrator as close as possible to the mold while vibration occurs.
9. After vibration, if necessary, add more mortar. Overfill the mold by only an 1/8" and work in as much as possible. Strike the remaining mortar off the top. Finish the surface with wood or magnesium float. Produce a flat even surface that is level with the edges of the mold. No impressions should be present along with no projections more than an 1/8".
10. Determine temperature of each batch (Summary: ASTM C1064 - Standard Test Method for Temperature of Freshly Mixed Portland Cement Concrete)
 - a) Make sure the temperature-measuring device is calibrated.
 - b) Submerge the sensing portion of the device 3" into the freshly mixed mortar making sure the sensor is surrounded on all sides by 3" of mortar. Press the mortar around the device gently so the ambient temperature is not affecting the reading
 - c) Leave the device in the mortar for 2 minutes or until the temperature reading levels off. Record the temperature to the nearest 1°F (0.5 °C).
 - d) Perform the temperature measurement within 5 minutes of obtaining the batch.
11. Use lids to cover cylindrical specimens and cover the top of the beam specimens with wet burlap to keep moist. Place a sheet of plastic over the burlap to keep it wet. The cylindrical specimens will harden with the axis of the cylinder vertical. The flexural beams should be formed with their longest axis horizontal.
12. Leave in casting room for 24 (+-) 8 hours
13. After 24 hours take the casts out of the molds and move them to another storage location (Create a curing room). They are to be moist cured at 73 (+-) 3 °F from the time of the molding to the time of the test. For the first 48 hours the casts should be vibration-free.
14. While the casts are curing cover them with wet burlap. (Temperature under the wet burlap will always be lower than the surrounding atmosphere)
15. For 28 days check on the specimens to make sure they are wet. Re-soak burlap if necessary. Again, use a plastic sheet to keep the burlap wet. Everyday the specimen will be turned 90 degrees.
16. 2 days before the tests the specimen will be uncovered and allowed to dry.

6.6.2. Summary: Standard Practice for Compressive Strength of Cylindrical Specimens

Materials: Cylinders - 4 X 2 (length X diameter)

Equipment: Loading Apparatus – two bearing blocks, one being a spherically seated block

1. Test loading apparatus' accuracy. The percentage error for the loads within range of testing should not be more than +- 1% of the indicated load.
2. Requirements for bearing blocks.

The bearing faces of the blocks should be at least 3% greater than the diameter of the specimen. *They should not depart from a plane by more than 0.001" in any 6" of blocks 6" in diameter or larger, or by more than 0.001" in the diameter of any smaller block; and new blocks shall be manufactured within one half of this tolerance.*

a) Bottom solid block – if new, this block should be at least 1” thick when it is new or at least 0.9” thick after any resurfacing operations. Should have a readily machinable surface. The centering of the specimen must be made relative to the spherically seated block above it. The bottom block may assist the centering as long as the center of the bottom block is directly below the center of the spherical head.

b) Spherically seated block – the maximum diameter of the block with a test specimen that is 2” in diameter is 4”. *The center of the sphere shall coincide with the surface of the bearing face within a tolerance of +/-5% of the radius of the sphere.* The diameter of the sphere should be at least 75% of the diameter of the specimen. The contact area with the specimen should not permanently deform under repeated use. It should withstand 12,000 psi. The curved surfaces of the socket should be well lubricated with petroleum-type oil (ie. motor oil). Further tilting after contact and small initial load is undesirable. *If the radius of the sphere is smaller than the radius of the largest specimen to be tested, the portion of the bearing face extending beyond the sphere shall have a thickness not less than the difference between the radius of the sphere and radius of the specimen. The least dimension of the bearing face shall be at least as great as the diameter of the sphere.* The design should allow at least 4° free rotation of the ball in the socket.

3. Specimen requirements

a) Specimen should be discarded if any cylinder diameter differs from any other diameter of the same cylinder by more than 2%.

b) Each end of the specimen when tested should not lose its perpendicularity to the axis by more than 0.5°. The specimen should be plane within 0.002”. The diameters of the specimens should be measured at mid-height of the cylinder. Two measurements should be taken at right angles to one another. An average of the two should be taken.

c) Diameter measurements should be done for one out of every ten specimens or three per day. This can be done as long as the molds produce consistent diameters within a range of 0.02”. If otherwise, then each individual cylinder diameter should be measured.

4. Procedure:

a) Cylindrical specimens should be tested in the moist condition

b) The permissible tolerance for a specimen that has aged 28 days is 20 hours or 3.0%.

c) Place the bottom solid block (hardened face up) on the table of the testing machine under the spherically seated bearing block. Make sure the surfaces of the bearing blocks are clean. Place the cylinder on the bottom solid block and align the axis of the specimen with the center of thrust of the spherically seated block.

d) Make sure the load indicator is set to zero. As the spherically seated block is brought down to make contact with the specimen rotate it so there is uniform seating.

e) Apply the load continuously at a rate of 20 to 50 psi/s. This should be maintained at least in the latter portion of the loading phase. A higher rate can be permitted in the first half of the loading phase.

f) Load the specimen until it fails and record the maximum load.

g) Note the characteristics of the failure and the appearance of the mortar.

5. Calculations:

a) Calculate the compressive strength.

$$\sigma_{\text{comp}} = P_{\text{max}} / A_{\text{ave}}$$

b) Round to the nearest 10 psi.

c) Also report defects in specimen and age of specimen

6.6.3. Summary: Standard Test Method for Flexural Strength of Concrete (Using Simple Beam with Third-Point Loading)

Materials: FRC or Concrete Beam – 8” X 2” X 2” (Length X Width X Depth)

Equipment: Loading Apparatus, Two Displacement measurement devices, Data Acquisition System, Yoke, Insulating Material, Tape Measure

6.6.3.1. Procedure:

1. Measure all dimensions of beam specimen.
2. Check beam surfaces for scars, indentations, or holes.
3. Center and position bottom supporting blocks contact points 6” away from each other. Center and position the upper load-applying contact points with the beam 2” apart. All four contact points with beam should be 2” apart.
4. In steps 5 and 6 place insulating tape “pad” on all contact points between loading apparatus and beam specimen.
5. Turn the beam on its side with respect to its position as molded and place it on the bottom supporting blocks so that the point of contact with the beam will be offset 1” from either end of the beam’s longest side (Center beam relative to the support blocks). Make sure to center beam along depth dimension relative to the supporting block depth. Measure span length to the nearest 0.1”.
6. Secure yoke to beam directly above the contact points of bottom supporting blocks. Secure displacement measurement devices onto both sides of yoke and position them at the direct center of the longest side of the beam.
7. Bring upper load-applying blocks in contact with beam and apply a load between 3 and 6 % of the estimated ultimate load. Make sure there is solid contact between beam and supporting blocks.
8. Start Data Acquisition System
9. Load beam continuously so that the deflection of the beam at the mid-span increases at a constant rate as near as possible to 0.00015 in/min or load beam continuously and apply at a rate that constantly increases the extreme fiber stress 165 lb/min until rupture occurs.
10. Termination of the test will be when either rupture occurs or when a deflection of 10.5 times the first-crack displacement is reached so the area underneath the curve up to this displacement is clearly defined.
11. Remove broken specimen from loading apparatus.
12. Take three measurements of each final dimension (both edges and center) to the nearest 0.05”. Measure distance to fracture along the neutral axis of the tension face from the fracture line to the closest end of the specimen. Note crack characteristics.
13. If fracture occurs in middle third section of the span length, then the modulus of rupture is calculated using this equation

$$R = PL/bd^2$$

R = Modulus of Rupture, psi

P = maximum applied load indicated by the testing machine, lbf

L = span length, in

b = average width of specimen at the fracture, in

d = average depth of specimen at the fracture, in

*The modulus of rupture is calculated in a different way if fracture occurs outside the middle third region of span length.

14. Record maximum applied load in pound-force, curing history, the apparent moisture condition of the specimen at the time of test, and the age of the specimen.
15. Calculate the flexural toughness and first-crack strength using ASTM C1018.

Summary: Standard Test Method for Flexural Toughness and First-Crack Strength of Fiber-Reinforced Concrete (Using Beam With Third-Point Loading)

- a) Determine the first-crack. This is the point on the load deflection curve where the curve first becomes nonlinear (onset of cracking in the concrete matrix). This point will depend upon the concavity of the initial portion of the curve.
- b) Determine the first-crack strength by using the load that corresponds to the first crack point on the load deflection curve and the equation for the modulus of rupture above. Round to the nearest 5 psi.
- c) Determine the first-crack deflection (δ). Round to the nearest 0.0001”
- d) Calculate area under the load deflection curve up to δ . Calculate the first-crack toughness in inch-pound or SI units.
- e) Calculate area under the load deflection curve up to 3δ point. Calculate toughness index I_5 and round nearest 0.1.

$$I_5 = \text{area under the load deflection curve up to } 3\delta / \text{area under the load-deflection up to } \delta$$

- f) Calculate area under the load deflection curve up to 5.5δ point. Calculate toughness index I_{10} and round nearest 0.1.

$$I_{10} = \text{area under the load deflection curve up to } 5.5\delta / \text{area under the load-deflection up to } \delta$$

- g) If possible, calculate area under the load deflection curve up to 10.5δ point. Calculate toughness index I_{20} and round nearest 0.1.

$$I_{20} = \text{area under the load deflection curve up to } 10.5\delta / \text{area under the load-deflection up to } \delta$$

- h) Calculate the residual strength factor

$$R_{5,10} = 20(I_{10} - I_5)$$

- i) If possible, calculate the residual strength factor

$$R_{10,20} = 10(I_{20} - I_{10})$$

6.7. References

- Balaguru, Perumalsamy N., and Surenda P. Shah. Fiber-Reinforced Cement Composites. New York, NY: McGraw-Hill Inc., 1992.
- Brandt, A.M. Cement-Based Composites: Materials, Mechanical Properties and Performance. New York, NY: E & FN SPON, 1995.
- Berg, Thomas W., “Fiber Reinforced Concrete.” The Technical Advisor June 1993: n. pag.
- Texas A&M SMART labs. July 8, 2002.
<<http://smart.tamu.edu/index.html>>
- Barnes, Clive, “Shape Memory and Superelastic Alloys,” July 8, 2002.
<<http://innovations.copper.org/1999/07/shape.html>>
- Mihalcz, Istvan, “Fundamental Characteristics and Design Method for Nickel-Titanium Shape Memory Alloy.” Periodica Polytechnica Ser. Mech. Eng. 45 (2001): 75-86.
- Duerig, Thomas W., Alan R Pelton, and Dieter Stockel. “Superelastic Nitinol for Medical Devices.” Medical Plastics and Biomaterials Magazine Mar.

1997: 30.

Reza, F., et al., eds. "Volume Electrical Resistivity of Carbon Fiber Cement Composites." ACI Material Journal, V.98, No.1, 2001, pp.25-35.

Zhang, Yunfeng, "The Mechanical Properties and Damage Monitoring of Concrete Reinforced with Short Nickel-Titanium Fibers with Shape Memory Effect." Project Proposal, April 23, 2002.

Section 7: Lateral Load Behavior of Unbonded Post-Tensioned Precast Concrete Walls with Horizontal Joints By Ed Regnier

Advisors: Dr. Richard Sause, Dr. Stephen Pessiki, Felipe Perez

7.1. Summary

The system proposed offers an alternative to cast-in-place walls for a lateral load resisting system. Unbonded post-tensioned precast concrete walls are constructed by post-tensioning precast walls across horizontal joints. The primary objective of this project is to analyze the wall system's lateral load capacity. Since the proposed system is relatively new, experimental as well as analytical analysis are being used to determine behaviors as well as provide a basis for improved design.

As an REU student this summer I spent most of my time assisting Felipe Perez, a Ph. D. candidate at Lehigh University, in both construction as well as analysis of theoretical and experimental data. This report offers a description of the wall system, its lateral load behavior as well as the experimental test set-up. It also explains DRAIN-2DX modeling, a finite element analysis program, used to model the wall system. The process as well as the various steps taken to obtain the most accurate material properties necessary for modeling in DRAIN-2DX will be detailed. In addition, the results of several parameter studies of user input in DRAIN-2DX will be discussed.

7.2. Background

The lateral load behavior of unbonded post-tensioned precast concrete walls is of particular interest for several reasons. Building codes in the United States allow for precast walls to be used for a lateral load resisting system only when they emulate cast-in-place walls. Unfortunately, to emulate cast-in-place walls some of the advantages of precast walls are lost such as lower cost. Emulating cast-in-place walls require detailed connections which can be expensive. In addition, field studies have shown precast walls emulating cast-in-place walls sustained significant damage from large lateral drift during an earthquake similarly to cast-in-place walls. Thus the purpose of this study is to design a precast wall system which, unlike cast-in-place walls, could withstand lateral loading without significant permanent damage.

As mentioned above, precast concrete is more desired than cast-in-place concrete for several reasons. Because the precast pouring environment is controlled, the temperature and moisture content do not vary for the most part during pouring and curing where as they may vary widely on site. In addition to a controllable environment, the strength of the precast concrete can be significantly increased. Most concrete poured on site have a strength of around 4-6 ksi. whereas some mixtures in precast can have strengths up to 12 ksi. Once on site, precast members can also be erected very fast, decreasing construction time as well as labor requirements. The design of a precast system is attractive in that not only would it be more appropriate structurally, it could also be more economical.

The unbonded post-tensioned precast concrete wall system of study was designed for an interior lateral load resisting system for a typical six-story building. The lateral load resisting system is of particular interest to the study of a building's structural integrity since it determines how well the building can withstand an earthquake. Figure 1 shows the prototype structure which the wall system has been designed for. Ten interior walls provide the lateral system in one direction while exterior shear frames provide resistance in the transverse direction.

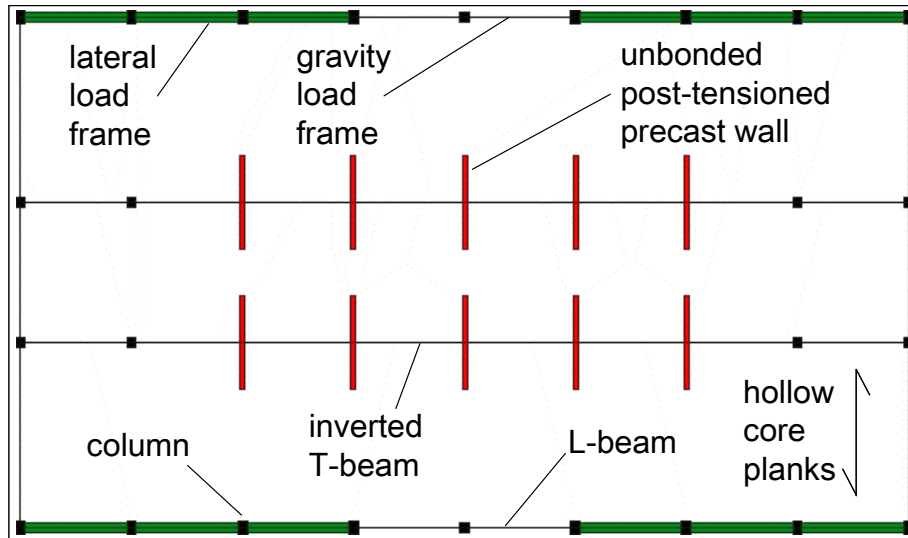


Figure 1: Plan view of a prototype structure. The proposed precast system is located in the interior of the structure.

7.3. Wall System

A general diagram of unbonded post-tensioned precast walls with horizontal joints is shown below in Figure 2. The wall designed for the prototypical structure consists of six one-story panels. The bottom panel, which takes the largest compressive stress, is built with reinforcement cages on both ends, which confine the concrete. The confined concrete is represented by the striped area below. Like all the other panels above it, it also contains vertical conduits, which the steel post-tensioning bars run through.

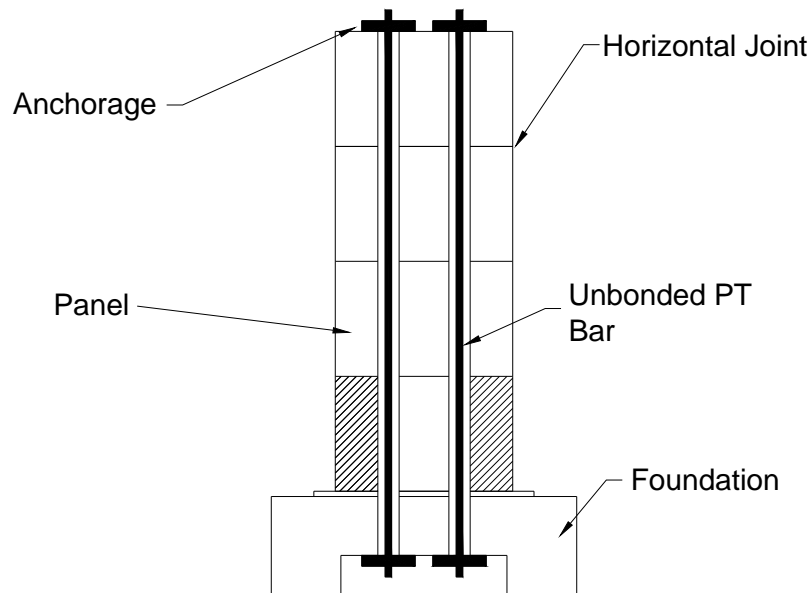


Figure 2: Basic components in wall system.

Since testing a full scale, six-story wall is not practical a modified design was made. Obviously the scaled wall has the same properties as the full-scale wall so behavior characteristics are not compromised. Figure 3 shows the dimensions of both the full-scale and scaled walls.

Full-Scale Wall

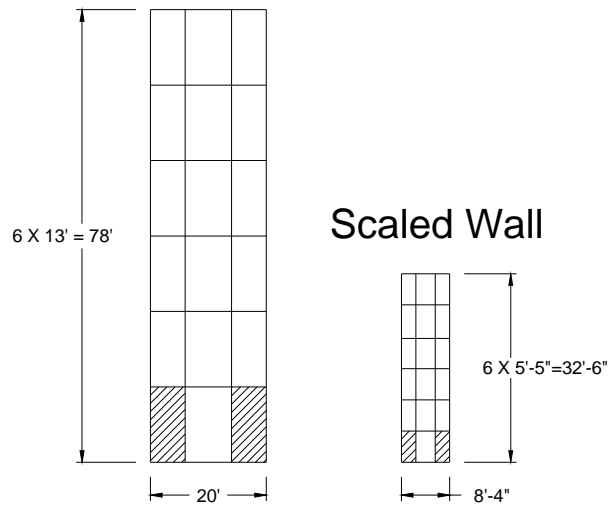


Figure 3: Dimensions of full scale and scaled walls.

Not only are the height and width scaled down, the thickness must be as well. Figure 4 shows the cross section of each wall. In addition to being half as thick as the full-scale wall, the scaled wall's confinement and post-tensioning design needed to be adjusted. The confining steel on this design was spiral reinforcement.

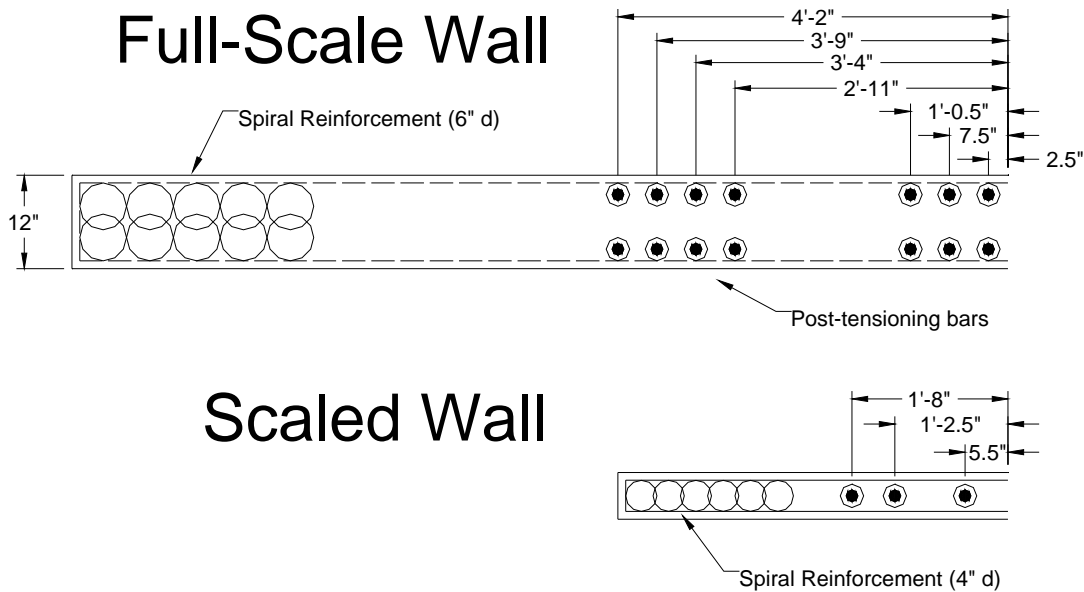


Figure 4: Spiral and post-tensioning bar layout of full-scale and scaled walls.

Once the wall system was scaled a test-set up had to be designed. An earthquake loading on a structure can be modeled as a triangular distributed load. In order to simulate this type of lateral loading, a simplification had to be made since applying a distributed load along the wall is not practical. Elementary mechanics show a distributed triangular load can be simplified using an equivalent load applied at the centroid of the triangle.

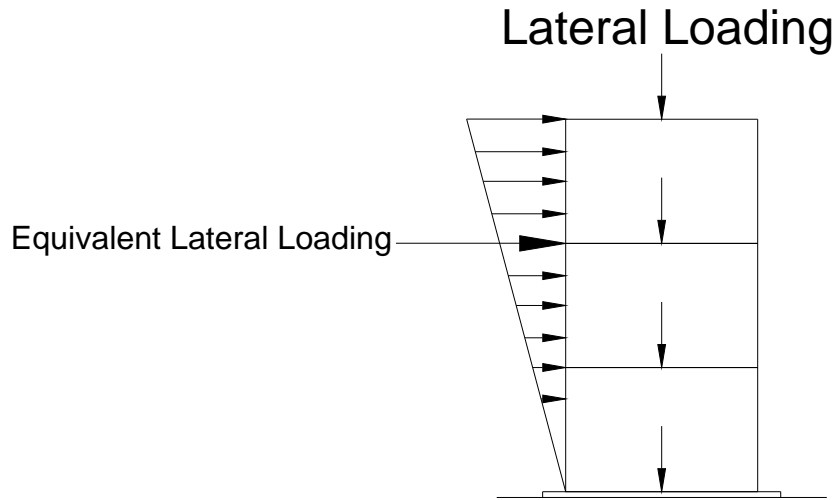


Figure 5: Simplified lateral loading.

Applying this simplified lateral load requires only one actuator. In order to reduce the amount of wall panels in the set-up a gravity actuator is incorporated. Since only one lateral load is being applied 2/3 up the wall, a gravity load can be applied on that same loading block to simulate the load of the top two panels. The gravity actuator has steel bars connected to the foundation, separate from the wall system. To apply a load it pulls the bars in tension and as a result, pushes the loading block down. The load applied is equal to the gravity load of both the top two panels as well as the designed gravity load it would take in the prototypical structure. This additional load would be applied from either the floors or the roof.

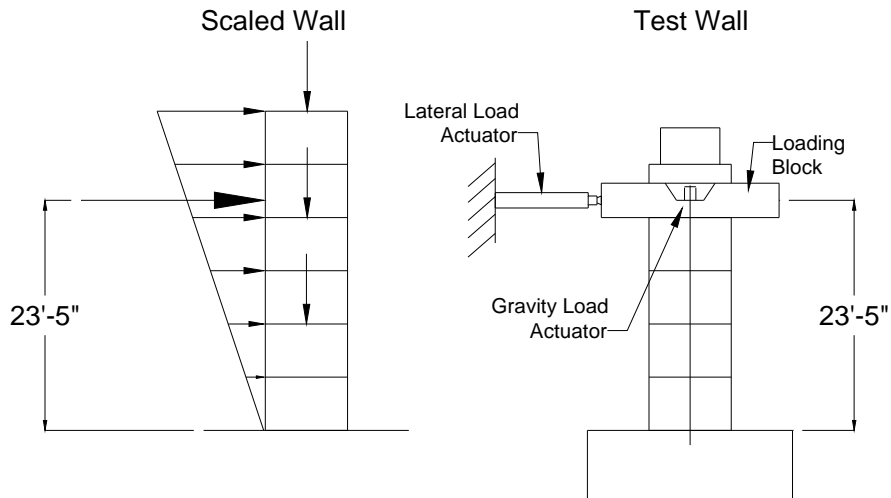


Figure 6: Test wall set up simulating scaled wall.

7.4. Lateral Load Behavior

The wall system which has been described goes through four different, distinct states during loading. Each state provides an opportunity to analyze the walls behavior and design as well as provide a basis to compare theoretical and experimental data. Assuming the wall system has been designed properly, the order of the behavior states is decompression, softening, yielding and eventually failure. (A poorly designed system could have failure before yielding.) Each state is described below. Note the standard modeling of each state during lateral loading is by loading block displacement (in.) and base shear, V (kips).

Figure 7 shows two possible behaviors of precast walls. Shear slip obviously is not a desired behavior since there is no restoring capacity and the wall is permanently damaged. There is also the risk of panels sliding completely off of the panels below them.

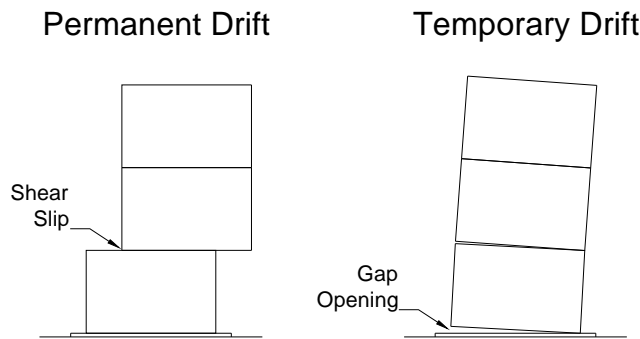


Figure 7: Shear slip vs. gap opening

Gap opening is a much more desired behavior since it allows for large lateral drift in addition to its restoring capacity. Once unloaded the wall will return to its original position due to the post tensioning bars as well as the gravity load.

As the walls are slowly loaded the compression at the base of the wall due to post-tensioning and the gravity load of the system begins to decrease. The decompression state is characterized by gap opening at the far end of the wall. As gap opening begins the concrete begins to behave non-linearly. It is important to realize that the side of the wall which is decompressing is not in tension once it decompresses it is merely under no stress because post tensioning is anchored to the foundation, not the bottom of the wall. One of the reasons for unbonded post-tensioning is that had it been bonded, the wall would behave like a cantilever beam with high tensile stresses on the lateral loading side. If this were the case, the concrete under tension would fail much earlier than any other system component causing permanent damage much earlier than desired.

As gap opening begins to lengthen along the wall the lateral stiffness of the wall begins to decrease significantly. This reduction is known as the softening state. The cause for this is either the nonlinear behavior of confined concrete or significant gap opening along the bottom of the base panel. If large compressive stresses are present at the beginning, softening is caused by nonlinear behavior of the concrete. If the initial stresses are small, softening is governed by significant gap opening.

Once the lateral stiffness has reduced significantly, gap opening increases faster as does drift (lateral displacement/height of wall). The larger the lateral drift, the more strain on the post tensioning bars. The next state begins when the bar closest to the lateral loading begins to yield. Typically no more than three bars in the test wall yield before the final state.

As the lateral drift keeps increasing the side opposite of gap opening takes an increasing compressive stress. The steel reinforcement is designed specifically with this in mind. Eventually the compressive stress on the outside of the wall is too large for the confined concrete and the wall fails. Once the confined concrete fails the wall cannot take any more lateral loading but it should still be able to withstand its designed gravity load.

Figure 8 shows the four behavior states at their approximate position on a typical Base Shear vs. Displacement curve. Notice the significant decrease in stiffness.

Base Shear vs. Loading Block Displ. Behavior States

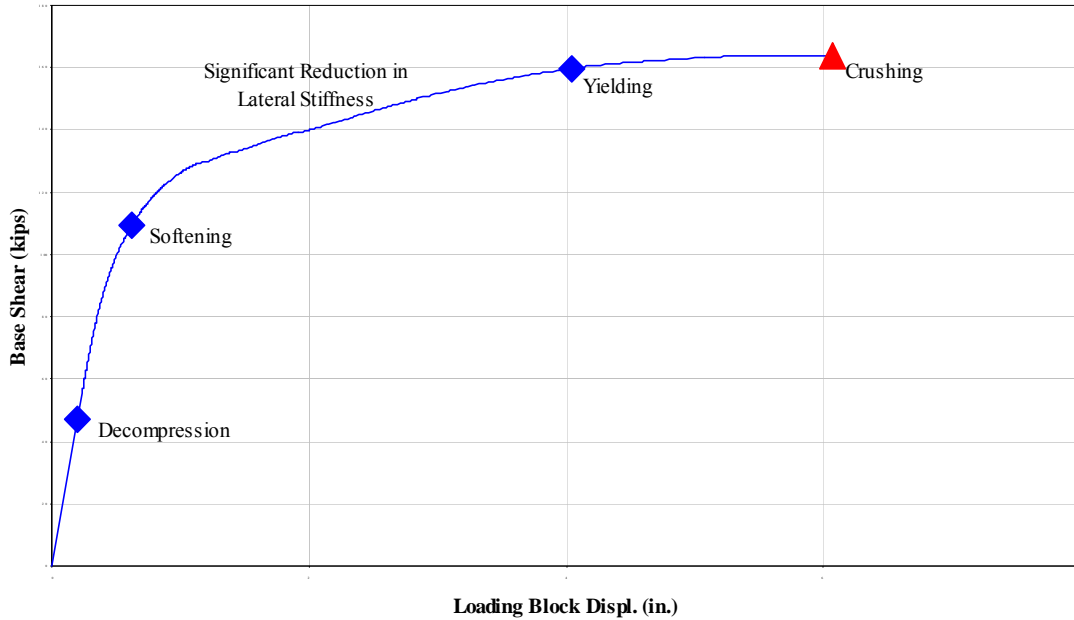


Figure 8: Behavior states of wall system.

7.4.1. DRAIN-2DX Model

7.4.1.1. DRAIN-2DX

In order to better understand the behavior of the wall system, computer analyses were run using DRAIN-2DX. This program uses the finite element method to model structures. What makes this program useful is its ability to model nonlinear elastic behavior as well as materials once they have become inelastic. This was a very important criterion for modeling this wall system since during loading the concrete eventually behaves nonlinearly, the post tensioning steel yields and the concrete eventually crushes.

The wall panels were modeled using fiber elements. Each fiber element consists of a number of segments, which have of a slice at their midpoint. Each slice is divided into individual fibers. The fibers are assigned specific material properties. Truss elements are used to model the post-tensioning bars. This model is simple, yet accurate.

Accuracy of the computer modeling is restrained by the amount of data the computer can process. Modeling this particular wall system requires stress-strain behavior of the steel post tensioning bars, unconfined and confined concrete. For each type of concrete, DRAIN requires 5 stress-strain points. For the steel it requires the stress-strain point where the bar yields as well as a ratio of the post-yielding modulus to the elastic modulus.

7.4.1.2. Material Properties

The cover concrete and concrete surrounding the post-tensioning conduits are all modeled as unconfined concrete (see Figure 4). The unconfined concrete properties were obtained using experimental data and a theoretical model. Three unconfined concrete cylinders were tested by Horan and the average of those results were used to calibrate Oh's unconfined concrete model (Horan). Figure 9 shows Horan's data compared to Oh's model. Oh's model was calibrated by setting the same peak stress (7.5 ksi.), strain corresponding to the peak stress (.0027 in./in.) as well as the modulus of elasticity obtained from the experimental data (3930.9 ksi.). Oh's model was useful in providing an unloading branch. In addition, Oh's model would prove useful for obtaining unconfined concrete stress-strain relationships for a parameter study where the modulus of elasticity was changed.

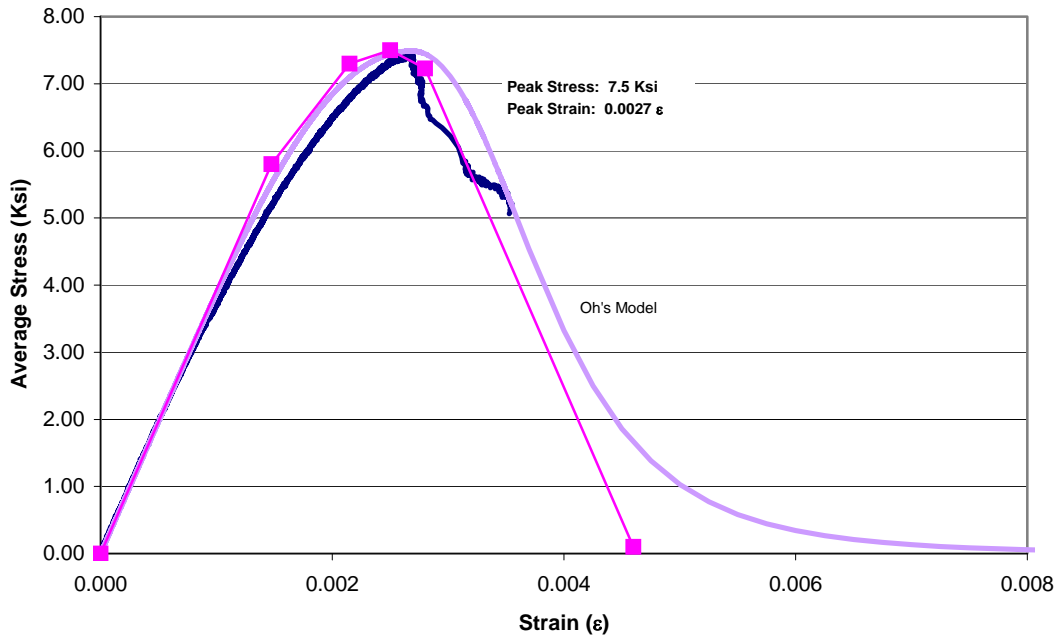


Figure 9: Unconfined Concrete with Discretization used for DRAIN model.

The concrete confined between the spiral reinforcement (Figure 4) was modeled using Mander's Model. Figure 10 shows both Mander's curve and its discretization using $E_c=3930.9$ ksi. The confined concrete always had to have the same modulus of elasticity as the unconfined concrete. Ideally unconfined and confined concrete behave the same until the unconfined begins to deform inelastically.

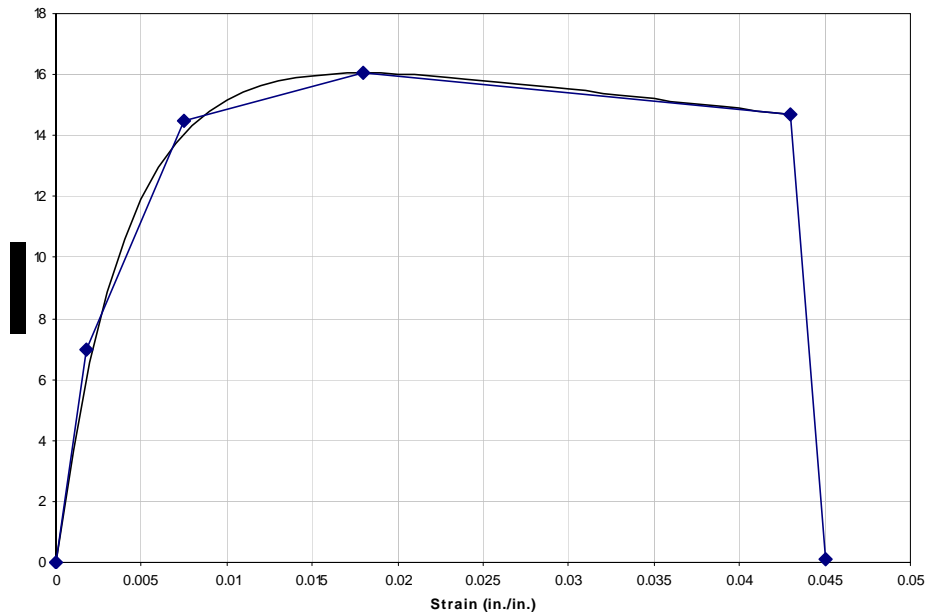


Figure 10: Typical discretization of confined concrete stress-strain relationship obtained using Mander's model.

7.4.1.3. Modulus Parameter Study

Several parameter studies were done to determine the sensitivity of user input in DRAIN on the corresponding output. Figure 11 shows the three different modulus of elasticities used. The lowest modulus, $E_c = 3930.9$ (ksi.), was determined from experimental tests run by Horan. The highest modulus, $E_c = 5196.15$ (ksi.), was found using an approximating equation:

$$E_c = 60\sqrt{f'c}(psi.)$$

Where $f'c = 7500$ (psi). This value was found from unconfined cylinder tests run by Horan and Regnier. The other modulus used was simply the average of the two moduli.

Each modulus produced different stress-strain curves for both confined and unconfined concrete. Figure 12 shows all three curves for unconfined concrete using Oh's model. Notice they all have the same unloading branch. Figure 13 shows the stress-strain curve for confined concrete using Mander's model. Each modulus has the same peak stress and corresponding strain but behavior before and after this peak stress is different. The lowest modulus obviously is the softest of the three at the beginning but it is also the softest after peak loading.

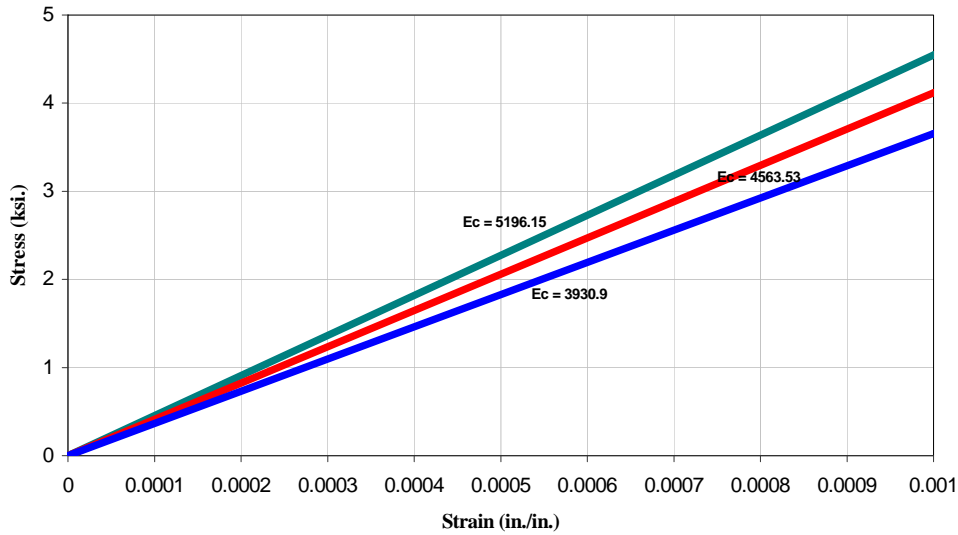


Figure 11: Modulus of elasticity values for parameter study.

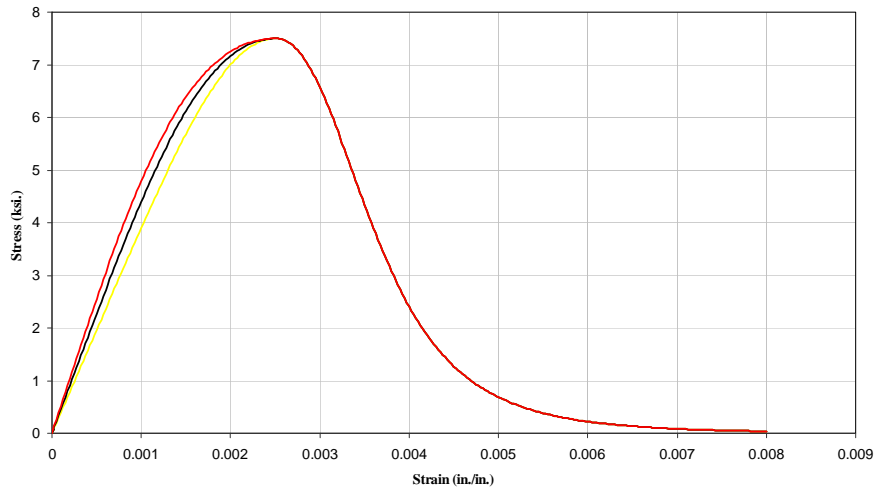


Figure 12: Oh's model for unconfined concrete using three different values of modulus of elasticity.

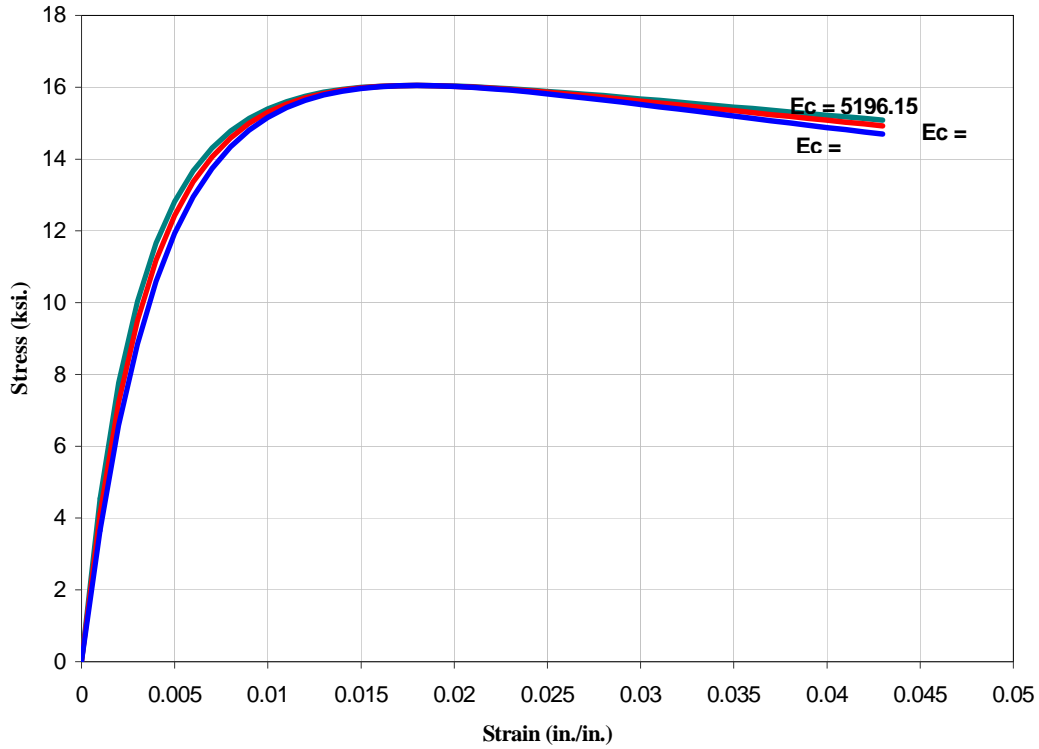


Figure 13: Mander's model for confined concrete using three different modulus of elasticity.

Once all the stress-strain curves for unconfined and confined were discretized, each modulus was run in DRAIN. Figure 14 shows all three moduli relating base shear to loading block displacement. As expected the lowest modulus, $E_c = 3930.9$ ksi., began softening first. Surprisingly though, it began yielding last and showed a superior lateral drift capacity compared to the other larger moduli. A general trend can be concluded that the lower the modulus, the larger the lateral drift before failure assuming the strength is constant. The results of this study are summarized in the table following figure 14 with each result normalized to $E_c = 4563.53$ ksi.

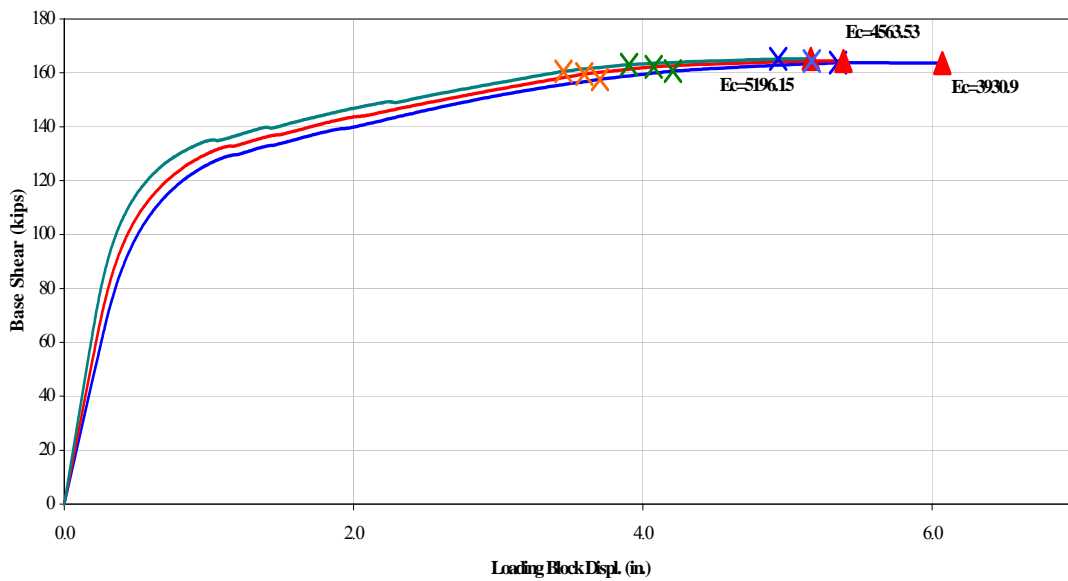


Figure 14: Lateral load behavior obtained for modulus parameter study

Table: Results for the modulus parameter study						
E_c (ksi)	Normalized E_c	Normalized Elastic Stiffness	Normalized V_{lp}	Normalized Δ_{lp}	Normalized V_{max}	Normalized Δ_{csc}
3930.90	0.86	0.86	0.99	1.03	1.00	1.13
4563.53	1.00	1.00	1.00	1.00	1.00	1.00
5196.15	1.14	1.19	1.01	0.96	1.00	0.96

7.4.2. 1st Point Study

The second study dealt specifically with the effect of discretization on output results. Using the same $E_c=3930.9$ ksi, three different tests were run using different 1st points. Figure 15 shows the three different discretizations.

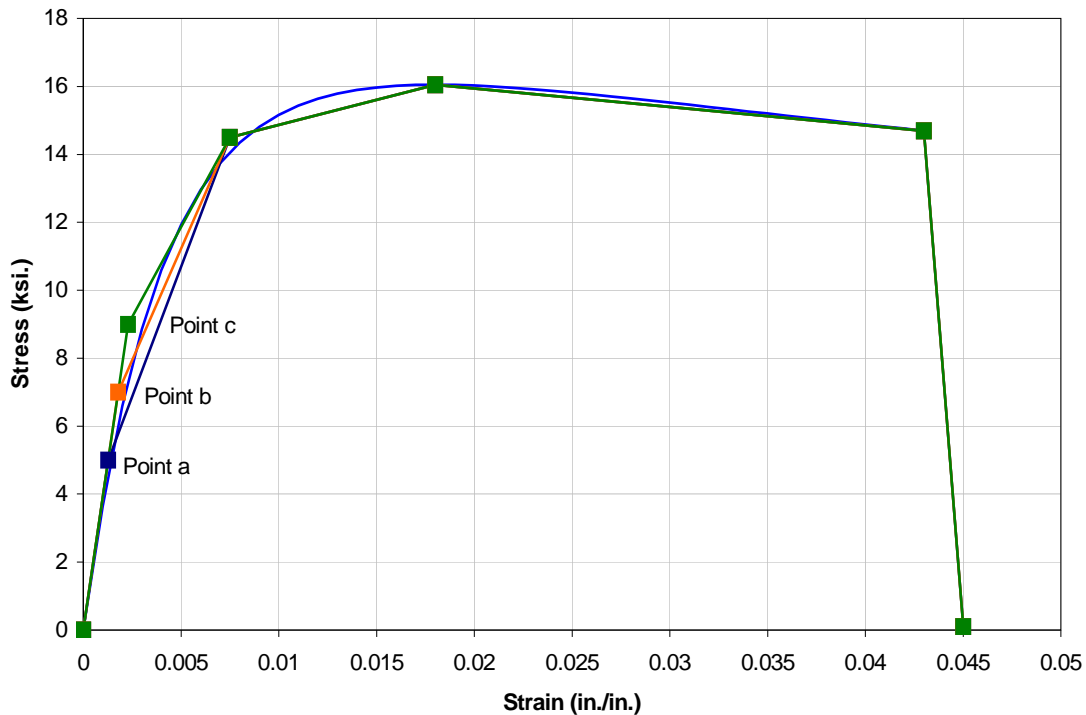


Figure 15: Discretization of Mander model for confined concrete using three different 1st points, but keeping $E_c = 3930.9$ ksi.

The results of these DRAIN runs had some very important results. As it can be seen on Figure 16, point *a* gave the best results even though looking at the discretization it appears to be one of the worst fit overall approximations. This point not only had the best lateral drift but it was extremely close to experimental in the softening region. Although additional DRAIN runs with varying modulus are recommended it appears that discretizing the stress-strain curve the closest at the beginning improves the model behavior of the wall. Since the best point appears to be the lowest one, it looks as though the substantial error in the discretization around the nonlinear concrete behavior plays little role in the overall behavior of the wall. This was concluded since in this study its softening region was still very accurate.

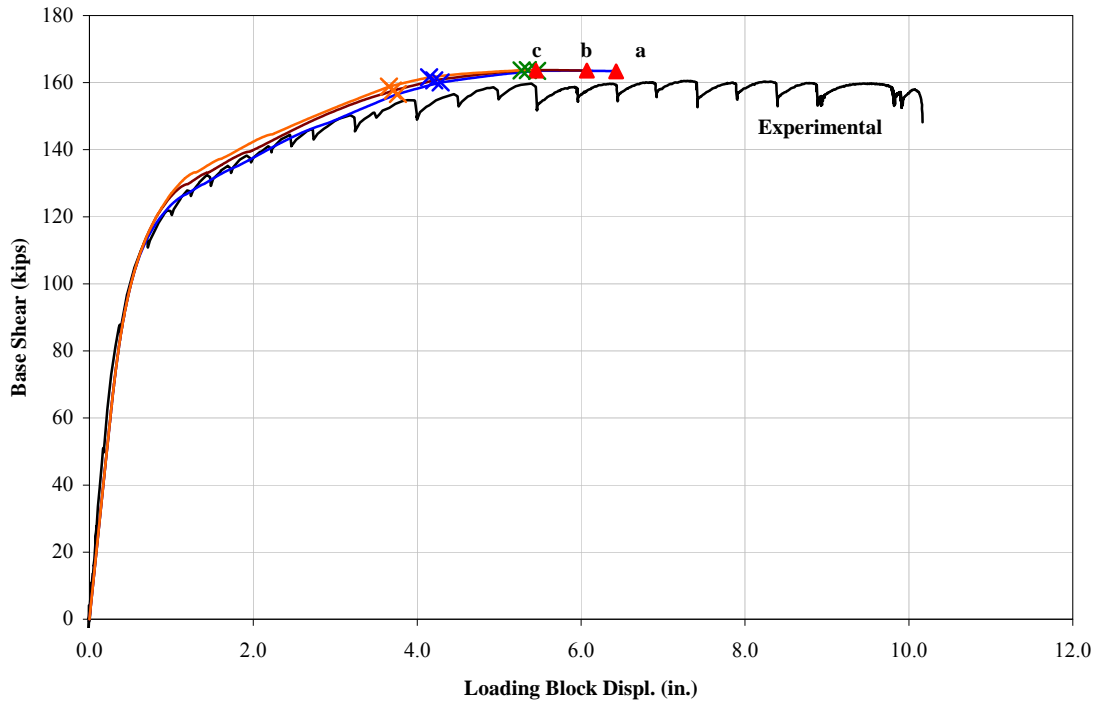


Figure 16: DRAIN results from first point study using $E_c=3930.9$ ksi.

7.5. Stub-Panel Comparison

The final study compared experimental data for the confined concrete with the previous methods mentioned. The experimental data was from a stub panel test. The stub panel was a section of the wall which was cut out. The panel was on the lateral loading side so it was not damaged at all during the experiment. As shown in Figure 17, the stub panel curve is much different than that obtained from Mander's Model.

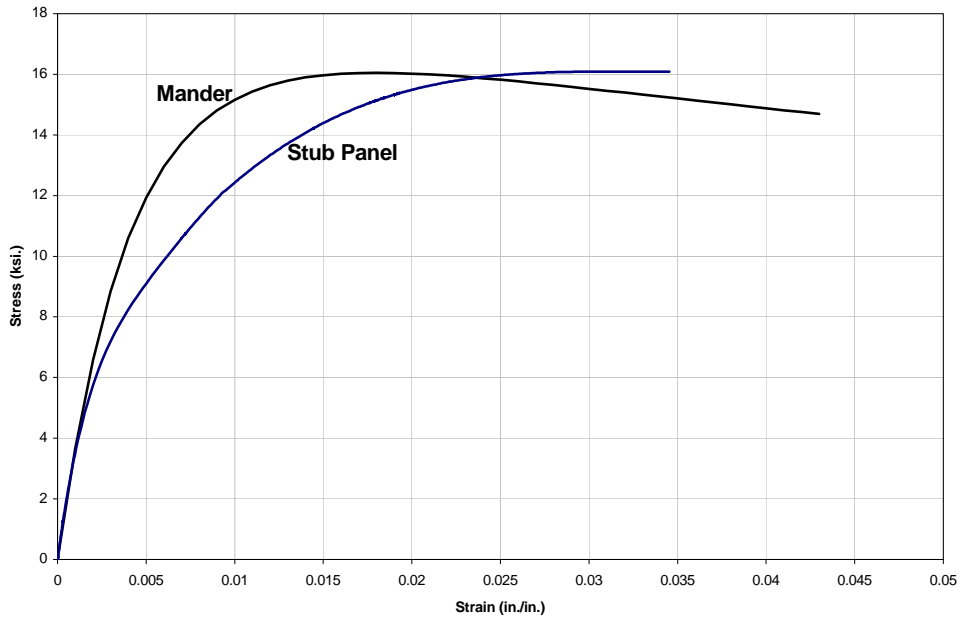


Figure 47: Confined concrete stress-strain relationships for stub panel and Mander model.

The differences between these graphs are very evident aside from the elastic loading at the beginning. The stub panel showed softening earlier than Mander's model but it also reached its peak stress later. This substantial difference in shape suggests Mander's model may need to be adjusted since it does not represent the characteristics of this confined concrete very accurately.

After completing the confined concrete stub panel test, the results had to be discretized. Figure 18 shows Mander's model, the stub panel test and the discretization used for DRAIN runs.

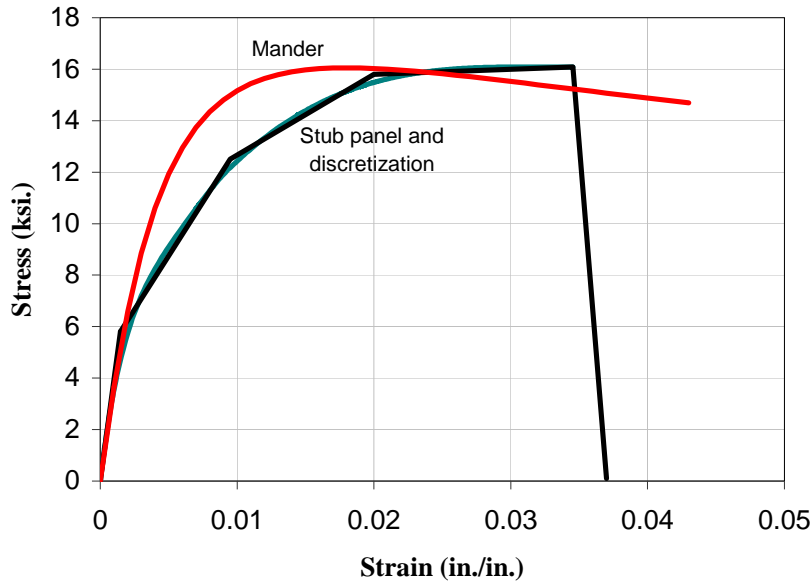


Figure 18: Linearization of stub panel confined concrete stress/strain relationship.

Figure 19 shows the stub panel data compared to the experiment and the best Mander model. The stub panel results are the closest to modeling the actual experiment. Although Mander was more accurate during softening, the lateral displacement of the stub panel is more than an inch closer to the experimental data than any of the Mander models.

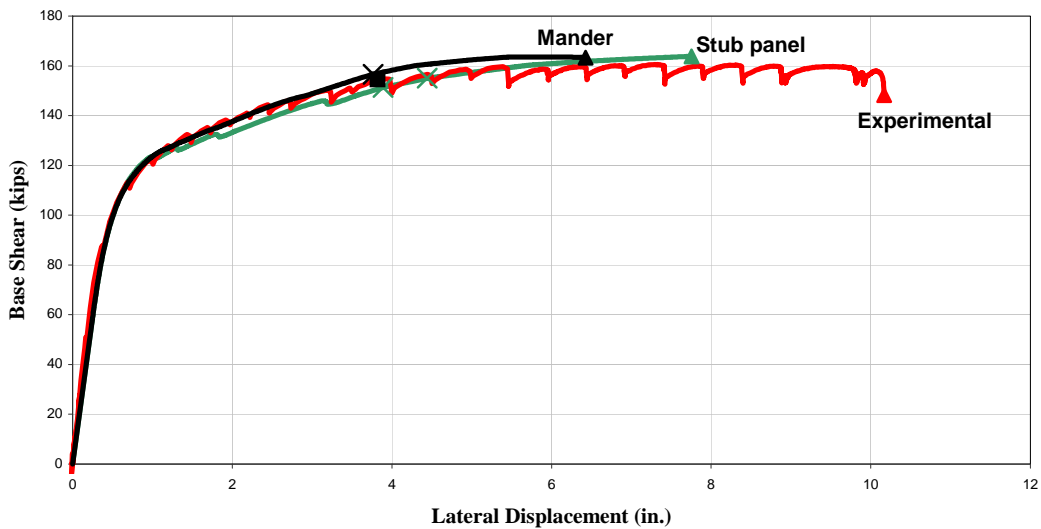


Figure 19: Lateral load comparison of experimental results and DRAIN models based on stub panel and Mander

7.6. Conclusion

The three different studies were done and all of them had useful results. The modulus study showed that the modulus not only affects the stiffness of the wall system it also affects the overall lateral drift. Although the lower modulus softens earlier as expected, it can withstand a larger drift before failure. The relationship between stiffness and the corresponding modulus may be linear but more studies must be run first to pick up a trend relating the two.

The 1st point study maybe showed the most surprising and important results. This data showed that possibly discretizing the concrete the closest at the beginning is more important than the overall discretization. A possibility which was not analyzed due to time constraints but should be before making such a conclusion would be to examine if point *a* had better results because it was closer to the stub panel results used on the final study. Either conclusion would show that the lateral drift capacity is sensitive to the discretization.

7.7. Acknowledgments

Dr. Richard Sause

Dr. Stephen Pessiki

Felipe Perez

Dr. Clay Naito

ATLSS

Lehigh University

Section 8: Field Instrumentation, Testing and Analysis of the Dubois Creek Fiber Reinforced Polymer (FRP) Bridge By Greg Parent

Advisors: Ian Hodgson and Robert Connor

8.1. Project Scope

8.1.1. Reasons for Building a FRP Bridge

For years engineers have been looking for alternatives to steel and concrete materials in order to avoid the high costs of rehabilitation of heavily used structures. Fiber Reinforced Polymers (FRP) could be such a substitute for steel and concrete. In 1999 it was estimated that \$111 billion were spent on rehabilitation and research of United States highways. A more durable material could dramatically lower current rehabilitation costs.

FRP materials offer additional advantages such as low weight, which can ease the installation process, and lengthen service life. Furthermore it is believed that FRP materials have good fatigue resistance, which would be very beneficial in bridge applications. A new FRP bridge has been installed over the Dubois creek in Great Bend Township, Susquehanna County, Pennsylvania, as part of a pilot program instituted by Penn Dot to investigate this new technology.

8.1.2. Description of Dubois Creek Bridge

The Dubois Creek FRP bridge is a relatively small bridge, as seen in Figure 1. The FRP deck rests on concrete abutments 20 ft. apart. It is a two-lane bridge with shoulders on both sides to make the total width = 32 ft. The bridge is skewed so that the concrete abutments create a 70-degree angle with the direction of traffic. The stream is about 5 ft. below the FRP deck. Concrete parapets attached to the FRP deck with rebar, span the upstream and downstream edges of the bridge. These parapets also serve as guiderail. The FRP deck is about 2 ft. thick, and has a wearing surface on the top side, which consists of a fine gravel-like material adhered to the surface.

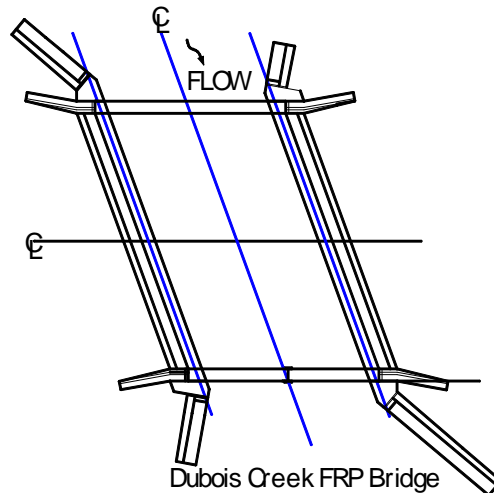


Figure 1: Dubois Creek FRP Bridge Plan view

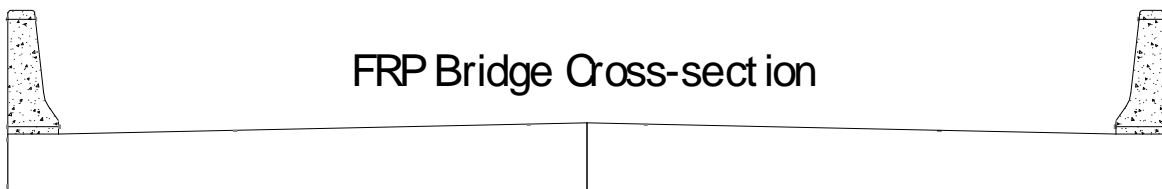


Figure 2. Dubois Creek FRP Bridge Cross-Section

8.2. Overview of the ATLSS Scope of work

ATLSS was subcontracted by Gannett Fleming to apply instrumentation in critical areas of the Dubois Creek FRP Bridge, perform controlled tests on the bridge, perform long-term monitoring of the bridge and report significant findings to Gannett Fleming. The overall goal is to gain an understanding of the behavior of the bridge, by investigating key field parameters such as strains and displacements.

8.2.1. Personal Goals

This REU project is focused on three main topics that are summarized below.

8.2.2. Behavior of the Parapet

On most concrete and steel bridges concrete parapets are not considered to be load-carrying members. However, based on the geometry of the bridge and the lower modulus of elasticity for the FRP material it was thought that the parapet might participate as structural elements and enhance the capabilities to the FRP bridge deck. The main goals of testing and analyzing the FRP bridge were establish the effect of the concrete parapet on the behavior of the FRP bridge deck, investigate the contribution of the parapet to the overall stiffness of the bridge, and to investigate the bending characteristics of the parapet experience.

8.2.3. Location of the Neutral Axis

Due to the influence of the parapet it was unclear where the neutral axis would be located at different transverse positions throughout the bridge. Would the neutral axis position remain the same throughout the entire cross-section, or would the neutral axis be at a different position in the parapet than in the composite deck? The instrumentation plan was developed in order to answer some of these questions. Every strain gage on the bottom of the deck has a corresponding rosette gage directly above it. By comparing the measured strains from the top and bottom of the deck and knowing the distance between the two gages it is possible to calculate where the strain should be zero, assuming a linear strain distribution through the deck.

8.2.4. Finite Element Modeling

The last part of this report deals with the finite element analysis, using the SAP2000 software package. Four models were constructed, each with different modifications implemented with the objective of more accurately modeling the measured response. Each model is described in detail, along with how each model differs from the rest, and how closely each model's results matches the experimental data.

8.3. Description of FRP Material

8.3.1. Fiber Reinforced Polymer Construction

Most FRP materials are organized into a laminate arrangement. Each lamina is made up of woven fibers in numerous directions embedded in a thin layer of light polymer matrix material. The fibers are usually made up of carbon or glass and provide stiffness and strength (see Figure 3). The matrix, commonly made up of epoxy, polyester or nylon protects the fibers from damage and transfers stresses between fibers (see Figure 4).

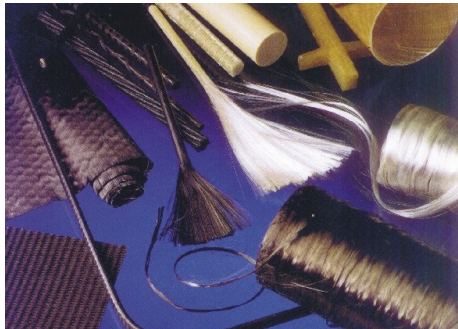


Figure 3: Fiberglass and Fiber carbon

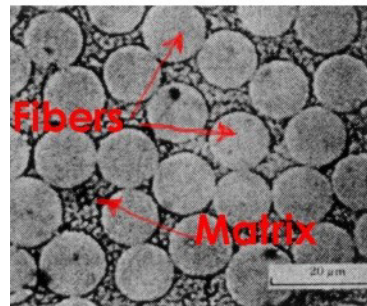


Figure 4: Fibers and Matrix

8.3.2. Pros and Cons

The most attractive properties of FRP material for use in a bridge application include excellent durability and corrosion resistance. Furthermore, their high strength-to-weight ratio is of significant benefit. A member composed

of FRP can support larger live loads since its dead weight does not contribute significantly to the loads that it must bear. Other features include ease of installation, and handling.

However, like most structural materials, FRP material has a few drawbacks that would create some hesitancy for civil engineers to use it in all applications. Some of these include high initial cost, brittle behavior, susceptibility to deformation under long-term loads, photo-degradation (from exposure to light), temperature and moisture effects, lack of design codes, and most importantly, lack of awareness and experience.

8.3.3. Description of Hardcore System

Hardcore Composites Inc. developed the FRP panels used in the Dubois Creek Bridge. The design of the panels is as follows. The flanges located on the top and bottom of the deck are 0.432 inches thick, the webs are 0.144 inches thick. The webs connect each flange are located every eight inches in both the transverse and longitudinal directions. The space between the webs and flanges are filled with 8 inches x 8 inches foam blocks which hold the shape of the webs.

8.4. Field Equipment Used

8.4.1. Displacement Sensors

Three displacement sensors were placed along the transverse centerline as shown in Figure 5. The displacement sensors used are Linear Variable Differential Transformers (LVDT). The three sensors were labeled Ch_51, Ch_52 and Ch_53. The sensors were held in place by steel scaffolding members, which were securely bolted to a temporary wooden deck work platform, under the FRP deck (Figure 6).

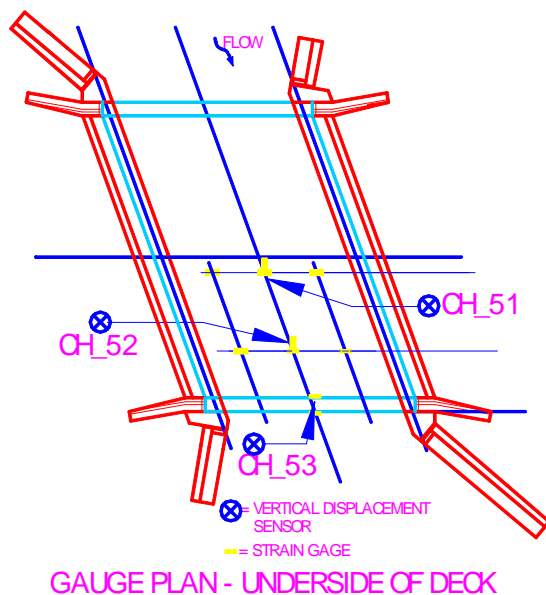


Figure 5: Location of Displacement Sensors



Figure 4: Typical Displacement Sensor Installation

8.4.2. Strain Gages

Two types of strain gages were used. The first are uniaxial strain gages, and the second are strain rosettes. See Appendix A for full instrumentation plans. Each rosette is made up of three uniaxial strain gages. One strain gage is oriented at 0 degrees, the second is oriented at 45 degrees, and the third is oriented at 90 degrees (See Figure 7). In order to measure the strains on the top of the FRP deck the strain gages had to be embedded within the deck. This was accomplished by installing the strain gage rosettes during the manufacturing of the FRP deck. The rosettes were applied to the 8-inch x 8-inch x 24-inch foam bottles that filled the space between the fiber fabric. The epoxy was then applied over the fiber fabric, the foam boxes and the strain gage rosettes.

The uniaxial strain gages were applied to the bridge on site. These gages have a 2 inch gage length. In total 14 strain gages were applied on site, 10 on the bottom of the FRP deck and 4 on the concrete parapet. The strain gages placed

on the bottom FRP deck were placed directly below the rosettes imbedded in the top of the FRP deck in a “T” configuration. (Figure 8) See Appendix A for a complete instrumentation plan.

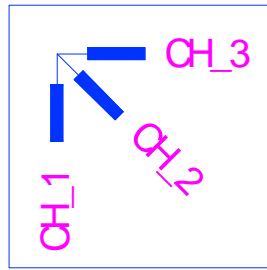


Figure 7: Rosette

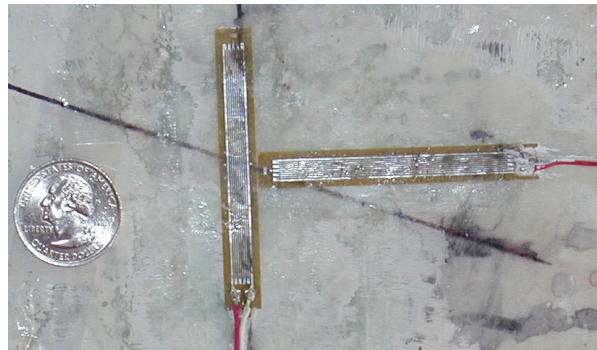


Figure 8: 2" 350 Ω strain gages

8.4.3. Data Acquisition System

The data acquisition system used is a CR9000 data logger manufactured by Campbell Scientific. The CR9000 is a modular, multi-channel digital data acquisition system that provides precision measurement capabilities in a rugged, battery-operated package. The system makes measurements at a rate of up to 100 K samples/second with 16-bit resolution. The CR9000 Base System includes CPU, power supply, and A/D modules inserted to configure a system for specific application. The on-board, Basic-like programming language includes data processing and analysis routines. PC9000 Windows™ Software provides program generation and editing, data retrieval, and realtime monitoring.

8.4.4. Instrumentation Plans

The instrumentation was placed at critical areas. Knowing how the bridge reacted at these areas provides good insight into the global behavior of the bridge. The instrumentation plans for the top deck, bottom deck and parapet are located in Appendix A.

8.5. Controlled Load Test

8.5.1. Test truck

The test truck was a three axle Mack Dump Truck, as shown in Figure 9. The dimensions of the truck can be seen in figure 10. The load on the front axle was measured as 13,700 lbs and the load on the back dual axle was 39,120 lbs. Lehigh personnel did not witness this measurement. The truck was weighed at New Milford Sand & Gravel, Inc., however the accuracy of this measurement should be questioned because the loads have been crossed out and penciled in, and the total load does not equal the back axle load plus the front axle load. This discrepancy in load could account for some of the error that occurred in the finite element models.



Figure 9: Test Truck

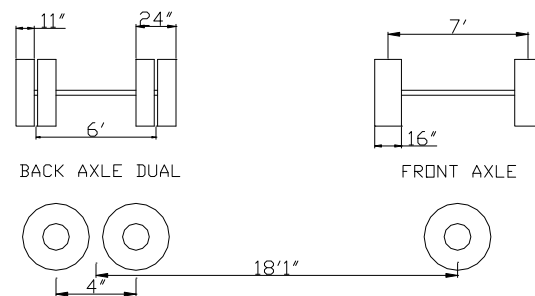


Figure 10: truck Dimensions

8.5.2. Test Types

There were three types of tests performed; each test was performed at different positions along the bridge.

Crawl (CRL): Load moving slowly (1-2mph) across the bridge.

Dynamic (DYN): The load moving quickly (23-25mph) across the bridge.

Park (PRK): The load parked on bridge deck.

8.5.3. Test Matrix

A summary of all the tests performed is contained in Table. I

Table I

Filename	Test Type	Travel Direction	Lane	Truck Orientation	Comment
CRL_US1.DAT	Crawl	South	US	Forward	57" from CL right dual to FF PPT.
CRL_US2.DAT	Crawl	North	US	Reverse	57" from CL right dual to FF PPT.
CRL_US3.DAT	Crawl	South	US	Forward	57" from CL right dual to FF PPT.
CRL_DS1.DAT	Crawl	South	DS	Forward	CL right dual over rosettes A, B, C
CRL_DS2.DAT	Crawl	North	DS	Reverse	CL right dual over rosettes A, B, C
CRL_DS3.DAT	Crawl	South	DS	Forward	CL right dual over rosettes A, B, C
CRL_DS4.DAT	Crawl	South	DS	Forward	CL left dual over rosettes D, E, F
CRL_DS5.DAT	Crawl	North	DS	Reverse	CL left dual over rosettes D, E, F
CRL_DS6.DAT	Crawl	South	DS	Forward	CL left dual over rosettes D, E, F
CRL_PPT1.DAT	Crawl	North	DS	Reverse	Left tires 4"-6" off FF DS PPT.
CRL_PPT2.DAT	Crawl	North	DS	Reverse	Left tires 4"-6" off FF DS PPT.
CRL_PPT3.DAT	Crawl	North	DS	Reverse	Left tires 4"-6" off FF DS PPT.
PRK_RT1.DAT	Park	South	DS	Forward	CL right dual over rosettes A, B, C;
PRK_RT2.DAT	Park	South	DS	Forward	CL right dual over rosettes A, B, C;
PRK_LT1.DAT	Park	South	DS	Forward	CL left dual over rosettes D, E, F;
PRK_LT2.DAT	Park	South	DS	Forward	CL left dual over rosettes D, E, F;
DYN_LT1.DAT	Dynamic	South	DS	Forward	Approx. speed = 23 mph
DYN_LT2.DAT	Dynamic	South	DS	Forward	Approx. speed = 23 mph
DYN_RT1.DAT	Dynamic	South	DS	Forward	Approx. speed = 23 mph
DYN_RT2.DAT	Dynamic	South	DS	Forward	Approx. speed = 23 mph

8.6. Test Results

8.6.1. General Response

The bridge displaced less than a 1/16th of an inch. The bridge experienced bending in both longitudinal and transverse directions. It appeared that the strains were well distributed throughout the bridge. Measured strains and stresses resulting from the test truck are very low.

8.6.2. Displacements

There were 7 different types of tests performed on the bridge. Each test was performed between two and six times (see Table I) to assure that the bridge would react the same way for the same test set-up. It was found that the tests were repeatable, thus the data from Crl_ds1, could represent the data from all six Crl_ds tests.

Table II. Displacements Experimental and Modeled

Crl_ppt3 Load Test Truck as close as possible to downstream parapet.	Ch_51 @ Centerline of Bridge (mils)	Ch_52 @ Centerline of D.S lane (mils)	Ch_53 @ Parapet (mils)
Experimental	-34.03	-56.67	-24.46

If the parapet truly acts as a non-structural (non-load-carrying) element, then all three displacement sensors should have very similar results for the same test. From Table II it is apparent that regardless of the test, the displacement under the parapet, ch_53, is much lower than the displacements near the center of the bridge, ch_51, or at the center of the downstream driving lane, ch_52. For the loading case in Table II, if the parapet acted as a non-load-carrying element, then ch_53 should have the greatest displacement. This confirms that the parapet stiffens the bridge, acts as a structural member and is carrying a significant part of the load. The displacement data for the Crl_ppt, Crl_ds, and Crl_us tests are available in Appendix B.

8.6.3. Strains

All of the microstrain vs. time plots are available in Appendix C, D, E. The complete instrumentation plan can be seen in appendix A for tests ppt1, ds1 and us1 respectively. Usually the strains show a nice smooth curve, however occasionally large spikes appear. For many cases the truck tires are running directly over the rosettes imbedded in the top of the composite deck. These rosettes are experiencing local strain, where the load, displacement, and strains are much higher around the immediate vicinity of the strain gages. This report will only be dealing with the global strains, how the bridge reacts as a whole to an applied load. Not all of the spikes can be explained by local strains. Ch_47, for example, seems to always be “noisy”, the strains seem to jump up and down as if there was a lot of interference with the signal. The cause for this is probably due to a damaged strain gage. Ch_47 was placed on the outside face of the parapet 2.5 inches above the top of the composite deck. Ch_48 was placed 2.5 inches above the composite deck on the inside face of the parapet. The strain data for Ch_47 and Ch_48 followed the same trends except that Ch_48 had no spikes. For this reason, the data from Ch_48 was used in the calculations of the location of the neutral axis. The data from Ch_48 replaced the data from Ch_47.

Ch_45 was located three inches from the top, on the outside face of the concrete parapet, Ch_46 was located three inches from the top, on the inside edge of the concrete parapet. Both of these strain gages were in compression however Ch_46 was always in less compression than Ch_45, even though these strain gages were at the same height. One explanation for this is the parapet is experiencing weak axis bending. Not only is the parapet bending downward about the strong axis, but it is also bending slightly inward towards the center of the bridge about the weak axis. When the parapet bends about the weak axis it puts Ch_45 in compression and Ch_46 in tension. This small tension strain is overshadowed by the large compression strains due to the strong axis bending, however it is apparent that Ch_46 is in less compression than Ch_45.

8.6.4. Neutral Axis

It was assumed that the parapet was perfectly bonded to the composite deck, (i.e. no slippage between the parapet and the composite deck). If there is no slippage then the strain diagram should be linear such as in Figure 11. If, however, there was zero bond between the parapet and the composite deck then the strain diagram would look like Figure 12. Figure 13 shows the experimental results of micro-Strain at a given time. It can be seen that the four values of micro-Strain do not fall on the same line. A linear regression line was plotted to give a best-fit line for the four data points. According to the diagram, the outside face of the parapet represents zero strain. Any values to the left are in compression; any values to the right are in tension. The neutral axis occurs where the linear regression line crosses 0 strain, any part of the parapet above that point is in compression; any point below is in tension.

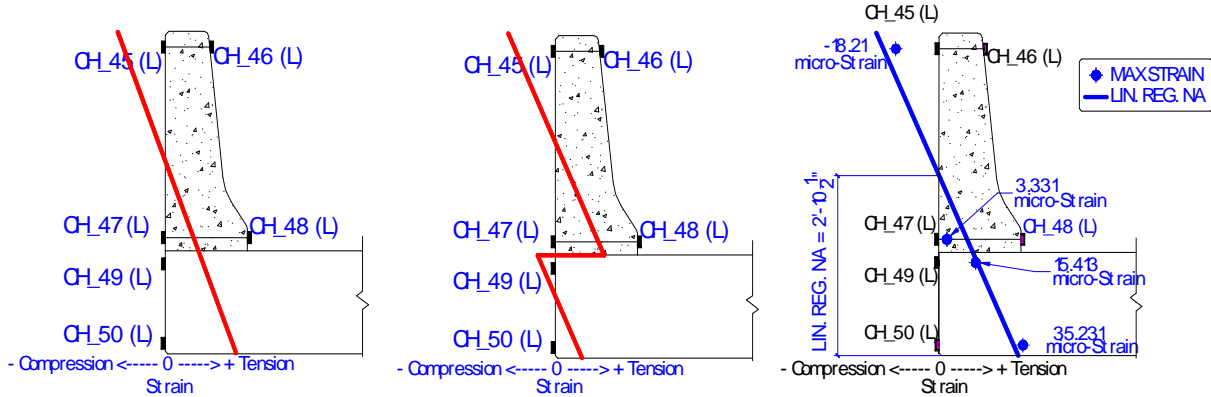


Figure 11: Fully Composite

Figure 12: Non-Composite

Figure 13: Experimental Results

It is apparent from Figure 13 that the neutral axis occurs in the parapet, however, the strain gages further from the parapet on the deck indicate that the neutral axis is located within the composite deck. This means that the neutral axis location varies with position on the bridge cross-section. In the original gage plan there was supposed to be a strain gages on the top and bottom of the composite deck three inches from the inside face of the parapet. The data from that strain gage would have indicated how the position of the neutral axis changes from its location in the parapet to its location inside the composite deck. Unfortunately it was not possible to apply a strain gage on the top of the deck because the wearing surface of the deck had already been applied. It would have required removal of some of the wearing surface to create a suitable bond between the deck and the strain gage. One of the major problems with FRP bridges has been delamination of the wearing surface. Removal of the driving surface to apply the strain gage could have exacerbated the delamination process. As a result it was decided that the strain gage three inches from the inside face of the parapet would not be applied. What it shown in Figure 12 is an estimate of how the neutral axis changes location.

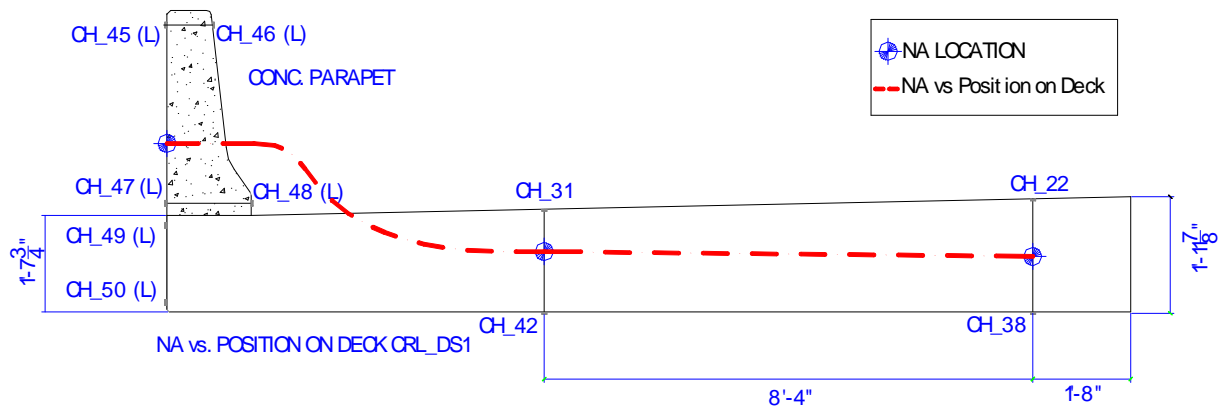


Figure 12: Neutral Axis vs. Position on deck

Refer to Appendix F for all of the neutral axis data.

8.6.5. Finite Element Analysis

8.6.5.1. SAP 2000

SAP2000 is a finite element analysis and design system that provides the structural engineer with a tool to analyze models of complex structures. It is easy to create models, modify the models, display and group results, and it has many different modeling tools. SAP2000 provides a single user interface to create, modify, analyze, check and optimize the design of a structure. Graphical displays of results, including real-time animation of time history displacements, are easily produced. To check the validity of the SAP results and the modeling methodology, the author constructed a number of simple models in SAP, including simply supported beams, and shells, and compared the analytical results from SAP with the results of hand calculations. All of the SAP results were extremely close to the hand calculations, within 0.4%.

8.6.5.2. Single Layer Shell Element Model

The very first model in SAP2000 was a simplified model. The moment of inertia of the cross-section of the FRP model was calculated and a shell model was constructed with an equivalent moment of inertia. The intent was that an equivalent moment of inertia would yield similar results as the honeycomb model, however this was not the case. The model values for the displacements were about 17 times greater than the experimental values.

8.6.5.3. Modeled Load Cases

The load cases were developed to simulate the load cases that were applied to the bridge in the field in order to determine if the results from the model matched the data in the field. In order to calculate the correct uniform load, the load of the rear axles dual must be divided by the total area of the deck in contact with the back dual tires. Each tire has an assumed footprint of (8 inches)(24 inches) = 192 in². For this case the load on the rear axle dual was 39,120 lbs, the total area of the deck in contact with the four rear wheels was = (4 tires)(192 in²) = 768 in². So the uniform load = 39,120 lbs/768 in² = 50.937 lbs/in² = 0.05094 ksi. In the following diagrams, Figures 11 through 13, the shaded rectangles represent the uniform loads.

There were three load cases modeled. The first represented the parapet crawl test. The second load case represented the downstream crawl test. The third load case represented the upstream crawl test. For each test the rear dual tire layout (represented by the four patch loads) was moved across the bridge deck to six discrete locations.

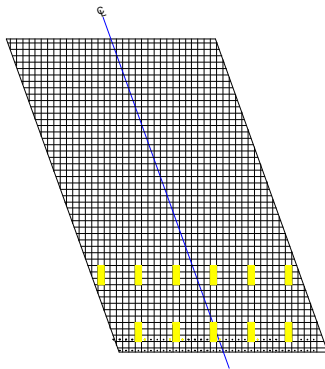


Figure 9: Parapet Crawl

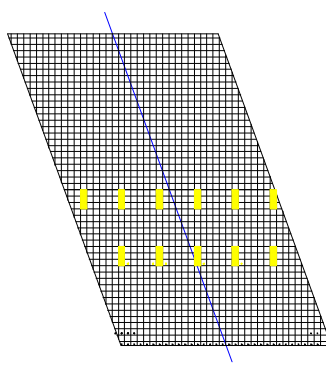


Figure 10: Downstream Crawl

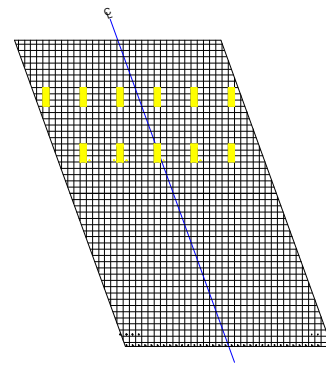


Figure 11: Upstream Crawl

8.6.5.4. Honeycomb Shell Element Model 1

The next model was a three dimensional model constructed with the elements of the same dimensions and material properties as the actual bridge. The top and bottom flanges have a thickness of 0.432 inches and the webs occur every 8 inches in both the transverse and longitudinal directions. Every web has a thickness of 0.144 inches. The 8-inch x 8-inch “boxes” are filled with non-structural foam in order to hold the shape of the box. For this model the entire bridge was made up of one continuous honeycomb panel with the same material properties for each shell element. This model will be referred to as Honeycomb 1.

8.6.5.5. Results of Honeycomb Model 1

The strains that are recovered from the analysis are representative of all the gages on the parapet (ch_45, ch_46, ch_47, ch_48, ch_49, & ch_50). For the parapet crawl load cases, the results of this model showed very similar trends in data as the field measured data, however the magnitudes for all the gages in tension were about twice as high as the experimental data. It should be noted that the strains measured on the bridge were extremely low. For the downstream and upstream loading cases, the modeled data varied largely from the experimental data in both trend and in magnitude. An explanation for this would be due to the entire model being modeled as one large panel. The actual bridge was made up of upstream and downstream panels, which were glued together along the longitudinal centerline. A glued joint resists shear very well but it does not resist bending, since the top and bottom deck plates are not continuous or spliced across the longitudinal joint. The second model was modified into two panels.

In order to maintain shear and bending resistance in the longitudinal direction but have no bending resistance in the transverse direction, the material properties along the joint must be modified. The FRP material is orthotropic,

meaning it has different material properties in different directions. For the second model, all of the flange and web elements along the longitudinal centerline were modified to have a modulus of elasticity of 0 ksi in the transverse direction. This model will be referred to as Honeycomb 2.

8.6.5.6. Results of Honeycomb Model 2

The analysis of this model yielded much better results for all load cases, especially for the Cr1_ds1 and the Cr1_us1 tests. All of the modeled data followed the same trends as the experimental data, however the magnitudes of the strains were slightly higher for the models. The graphs comparing the parapet strains for model data and experimental data can be found in Appendix G .

This model has no resistance to transverse tension or to compression across the longitudinal centerline. This is supposed to represent the glued joint, which has poor resistance to tension perpendicular to the glued surface. Therefore it cannot resist bending, however the upstream and downstream panels are flush against each other and can resist a compression force. This is not represented in this model. A third honeycomb model had to be constructed with resistance to compression in the transverse direction along the longitudinal centerline. This model will be referred to as Honeycomb 3.

8.6.5.7. Results of Honeycomb Model 3

By checking previous models the flange elements on the top of the composite deck were all found to be in compression in the transverse direction. These elements were given material properties with E = 3650 ksi in the transverse direction the bottom flanges at the joint were unchanged with E = 0ksi transverse to the joint. Honeycomb 3 could also be described as one continuous panel representing the top flange of the composite deck and two separate upstream and downstream panels representing the bottom flanges of the composite deck.

The analysis of Honeycomb 3 gave results that were very similar to Honeycomb 2 results, however the magnitudes of the parapet strains of Honeycomb 3 were slightly larger (by about 9%) than Honeycomb 2. The model data that most closely fit the experimental data, was Honeycomb 2. Out of the three models, Honeycomb 2 had the smallest error, on average around 20%. As was mentioned earlier, the load of the actual test vehicle may have differed from the load that was reported to us by New Milford Sand & Gravel, Inc. If the load reported to us was an overestimate it could account for some of the error of our model data.

Table III: SAP Model and Experimental displacements

Cr1_ppt3 Load Test Truck as close as possible to Downstream Parapet	Ch_51 at Centerline of bridge (mils)		Ch_52 at Centerline of D.S. Lane (mils)		Ch_53 at Parapet (mils)	
	Experimental	% Error	Experimental	% Error	Experimental	% Error
E = 3650 ksi TOP AND BOTTOM MODEL	-27.7	22.8	-52.4	8.2	-39.0	37.3
E = 0 ksi TOP AND BOTTOM MODEL	-29.0	17.4	-52.8	7.4	-39.3	37.7
E = 3650 ksi TOP and E = 0 ksi BOTTOM	-28.6	18.8	-52.6	7.7	-39.2	37.5

It also appears that for channel 53 (located under the parapet), all of the models seem to have displaced more. This would imply that the parapet had less of a stiffening effect in the models than it did experimentally. The parapet also seems to have less of a stiffening effect in the strain models of the parapet.

Table III. EXPERIMENTAL AND MODELED RESULTS OF LOAD TEST CRL_DS

Experimental	Ch_45		Ch_46		Ch_47		Ch_48		Ch_49		Ch_50	
	Experimental	% Error	Experimental	% Error	Experimental	% Error	Experimental	% Error	Experimental	% Error	Experimental	% Error
	-16.6	% Error	-14.2	% Error	2.9	% Error	3.1	% Error	13.5	% Error	33.4	% Error

Honeycomb 1	-18.2	8.5	-19.8	28.3	5.3	44.9	10.9	71.2	36.4	62.8	74.4	55.1
Honeycomb 2	-14.2	17.5	-11.0	29.6	2.7	10.7	9.3	66.4	20.0	32.2	52.5	36.4
Honeycomb 3	-14.3	16.1	-11.6	22.8	3.0	3.2	10.1	69.2	21.7	37.5	57.6	42.0

Table IV. EXPERIMENTAL AND MODELED RESULTS OF LOAD TEST CRL_US

Experimental	Ch_45		Ch_46		Ch_47		Ch_48		Ch_49		Ch_50	
		% Error		% Error		% Error		% Error		% Error		% Error
Honeycomb 1	11.2	547.3	12.8	2028.5	-7.6	1081.4	-3.2	1482.1	24.8	2194.4	-48.9	936.9
Honeycomb 2	-0.9	46.6	-0.3	51.1	-0.6	7.1	0.7	239.8	1.0	5.6	5.2	10.8
Honeycomb 3	-1.3	22.5	-0.6	6.5	-0.4	36.6	1.3	536.8	1.7	54.6	7.2	51.5

On the whole the parapet reaction of Honeycomb 2 was similar to that of the experimental results. The model was very accurate in trends, however the magnitudes of strain were consistently higher in the SAP models than in the experimental data. Further refinement of the model would likely improve results.

8.7. Conclusions

In conclusion the parapet was found to be a substantial load-carrying member that significantly stiffens the bridge. From the experimental results it was apparent that even with the truckload as close as possible to the parapet the displacement sensor under the parapet displaced less than any of the other displacement sensors.

Overall, the bridge experienced small strains when subjected to the test truck loading. Displacements were also very small. The neutral axis was found to change location at different positions on the deck. As was originally suspected along the upstream and downstream edges the neutral axis was located in the concrete parapet but neutral axis moves down within the composite deck with increasing distance from the parapet. The modifications to the SAP models did improve the results. The trends were almost identical, but the magnitudes of the models were not identical. The model data that most closely resembled the experimental data was model Honeycomb 2.

8.8. Acknowledgements

Ian Hodgson

Robert J. Connor

Prof. Clay Naito

PITA

PennDOT

FHWA

ATLSS

8.9. References

CR9000 Measurement Control System, Training Manual by Campbell Scientific p. OV-1

SAP2000...Finite Element Analysis and Design System Computers and Structures Inc., web page: <http://engineering.ceanet.com.au/products/sap2000.asp>

Materials in Action Series, Structural Materials, Peter Lewis and Nick Reid, Butterworths 1990, pp. 314, 315.

Analysis of Dubois Creek Bridge, Susquehanna County Analysis Report. Rev.B Hardcore Composites, July 10, 2001 Hayati Catbas.

Section 9: Acknowledgements

The principal investigators would like to thank the Pennsylvania Infrastructure Alliance and the ATLSS center for financial support of this project. The organizers would also like to commend the work that the research advisors and graduate students put in to make this program a success. Additional thanks to Frank Stokes and John Hoffner for making the laboratory available to students, and to Jack Bower and Peter Bryan for helping the students get situated. Special thanks to Elia Schoomer and Sharon Seigler for their assistance with the presentation and library seminars, and to Schuylkill Products, Weidlinger Associates and High Steel for the tours. Thank you to all the ATLSS staff and students for making this a friendly environment for the students to work in.